1-28-2015

X-RAY CHARACTERIZATION OF PLATINUM GROUP METAL CATALYSTS

Eric Peterson

Eric J. Peterson

Candidate

Nanoscience and Microsystems Engineering

Department

This dissertation is approved, and it is acceptable in quality and form for publication:

Approved by the Dissertation Committee:

Abhaya K. Datye , Chairperson

Adrian Brearley

Deborah Evans

Hua Guo

X-RAY CHARACTERIZATION OF PLATINUM GROUP METAL CATALYSTS

by

ERIC J. PETERSON

B.S. Geology, 1978

DISSERTATION

Submitted in Partial Fulfillment of the
Requirements for the Degree of

Doctor of Philosophy
Nanoscience and Microsystems Engineering

The University of New Mexico
Albuquerque, New Mexico

December, 2014

Acknowledgements

I would like to thank my advisor, Dr. Abhaya K. Datye for his patience, kindness and guidance in this work. I also thank Dr. Andrew DeLaRiva for his electron microscopy skills, catalyst reactivity measurements and companionship at the beamline, Dr. Barr Halevi for his wisdom regarding reactivity measurements, as well as the rest of the members of Dr. Datye's Catalysis Group, all of whom have provided help, insight and encouragement. Bruce Ravel, Anatoly Frenkel, and Jeff Miller were of great assistance in guiding me through the nuances of X-ray absorption spectroscopy. I would also like to thank Dr. Deborah Evans, Dr. Adrian Brearley and Dr. Hua Guo for agreeing to sit on my committee. Finally, I thank my mother, Harriett and my son Jeff for their encouragement.

X-RAY CHARACTERIZATION OF PLATINUM GROUP METAL CATALYSTS

By

Eric J. Peterson

B.S. Geology

Doctor of Philosophy, Nanoscience and Microsystems Engineering

Abstract

Platinum group metals (PGMs) are used extensively as catalysts, employed in several sectors of the world energy economy. Fuel cells employing PGM catalysts show promise as power sources in the proposed hydrogen economy, using alcohols as hydrogen storage media. Currently, the most economically important application for PGMs is for the mitigation of emissions from internal combustion engines via catalytic converters. In all applications, efficient use of these expensive metals to fabricate robust catalysts is of the utmost importance.

Understanding the catalyst structure/property relationship is the key to the improvement of existing catalysts and the discovery of new catalysts. For example, catalyst particle size can have profound effects on catalyst activity, as in the case of gold nanoparticles. Catalyst particle size control and stability is also important for the efficient use of PGM metals and catalyst deactivation prevention. The challenge is to identify and characterize structural features and determine if and how these features may relate to catalytic properties. The ultimate goal is to simultaneously measure catalyst structural

characteristics and catalytic properties under *operando* conditions, unambiguously establishing the structure/property link.

X-ray diffraction (XRD) and X-ray absorption spectroscopy (XAS) are important techniques used for the characterization of PGM catalysts. Microstructural information such as crystallite size, as small as ~ 1 nm, and microstrain can be obtained from Bragg diffraction peak shapes in X-ray diffraction patterns, and long range crystal structure information is found in the intensities and positions of these peaks. In contrast, X-ray absorption spectroscopy provides information about the chemical state and local structure of selected atoms. From the average nearest neighbor coordination numbers, crystallite sizes can also be inferred, with particularly high sensitivity in the sub-nm size range. Electron microscopy complements information obtained from both XRD and XAS. With aberration-corrected HAADF, particles ranging from sub-nm-size down to clusters of a few atoms and isolated single-atoms can be routinely imaged. A challenge to the interpretation of these images is the characterization of mixed atomic species, in this case, palladium and lanthanum. In this work we show for the first time that quantitative chemical identification of atomically-dispersed mixtures of palladium and lanthanum in an industrially relevant catalyst (palladium on lanthanum-stabilized gamma-alumina) can be obtained through image intensity analysis.

Using these techniques we have characterized the state of bimetallic fuel cell catalysts, *ex situ*, and have examined the state of Pd catalysts under *operando* CO oxidation conditions.

Table of Contents

List of Figures

List of Tables

Chapter 1 Introduction and scope of research

1.1. Introduction

The field of heterogeneous catalysis encompasses many applications, and plays an important role in the world economy. Heterogeneous catalysts are employed in the automobile, energy and petroleum industries, the production of fine and bulk chemicals, and food processing. In 2010, heterogeneous catalysis was estimated to be a 29.5 billion

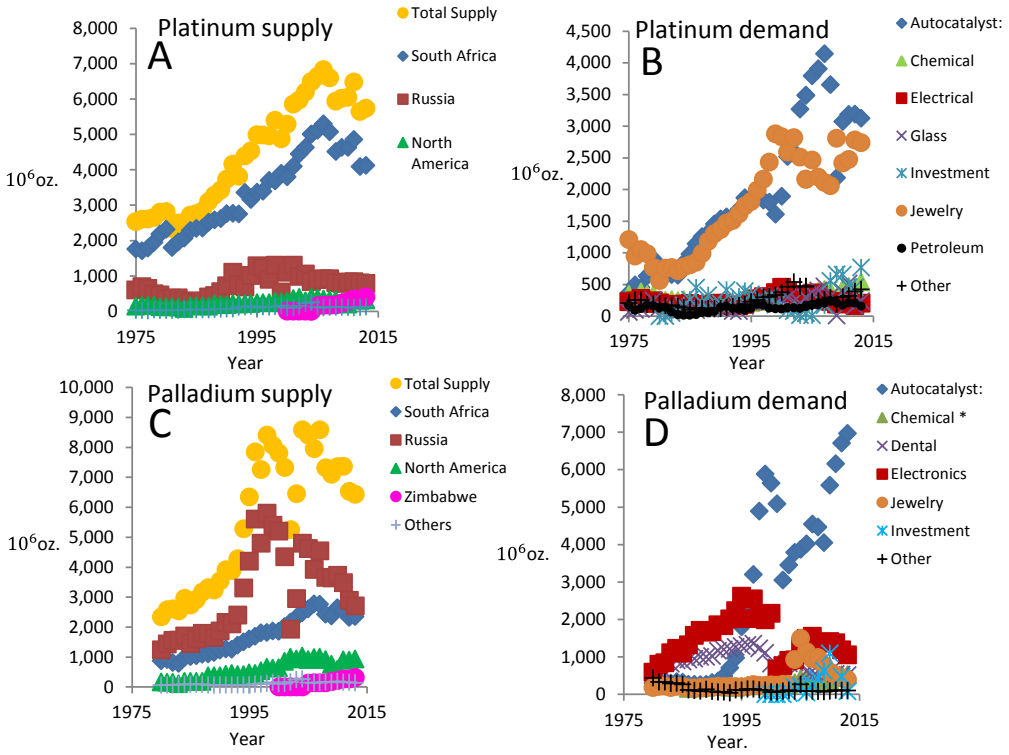

Figure 1.1 World-wide platinum and palladium supply (A and C) and demand (B and D) [1].

USD business [2]. Platinum group metals (PGM) play a major role as industrial catalysts, usually in conjunction with a high surface area support such as γ-alumina.

The production of these strategic metals occurs primarily outside of the United States with South Africa being the primary source for platinum and Russia for palladium (Fig. 1.1). The primary demand for platinum is the automobile industry, with slightly less demand for use in jewelry. Automobile applications are also the main use for palladium, followed by electronics, dental and jewelry applications. The variation of platinum and palladium prices over the past two decades or so is shown in Figure 1.2. Platinum is seen to be quite expensive, and is generally comparable to gold in price. Palladium, while less expensive than platinum, is still costly, and tracks the market price of platinum.

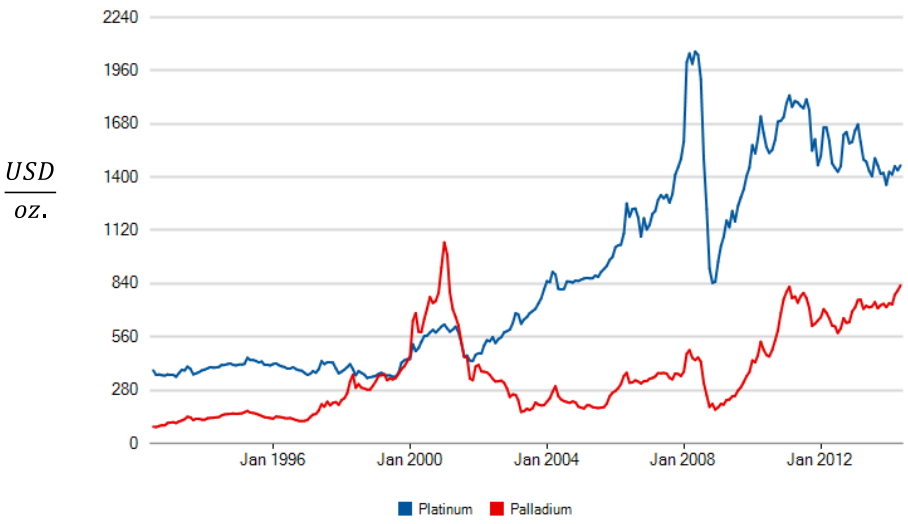

Figure 1.2 Platinum and palladium prices [1].

The catalytic properties of platinum had been described in the early 1800's [25]; however, agreement on the definition of the term "catalyst" was not achieved until c.a. 1900: "*A catalyst is a substance which affects the rate of a chemical reaction without being part of its end products"* [26]. Reports on the redox behavior of CO appeared thereafter (eg. [27, 28]), but were sparse until the 1920's, after the use of poison gas on the battlefield in WWI sparked interest in room temperature catalytic oxidation of CO. Oxide catalysts such as Cr, Hg, Ag, Cu, and Mn-oxide (eg. [29-34]) were explored for use in gas masks.

Because of the expense and potentially precarious availability of PGMs. there is strong motivation for efficient use. For catalysts, this means maintaining as small of a particle size (typically a few nanometers in diameter) as possible.

1.2. Energy Storage Applications

An important and growing application for PGM catalysts is in the energy storage arena. One aspect of this is the storage of excess energy generated by intermittent renewable energy sources such as wind and solar. In particular, in Europe there has been significant increase in the fraction of total power produced by renewables. For example recently (June 9, 2014) Germany experienced a day in which 50% of its power was provided by solar-generated electricity [3]. Figure 1.3 shows the hourly variation in

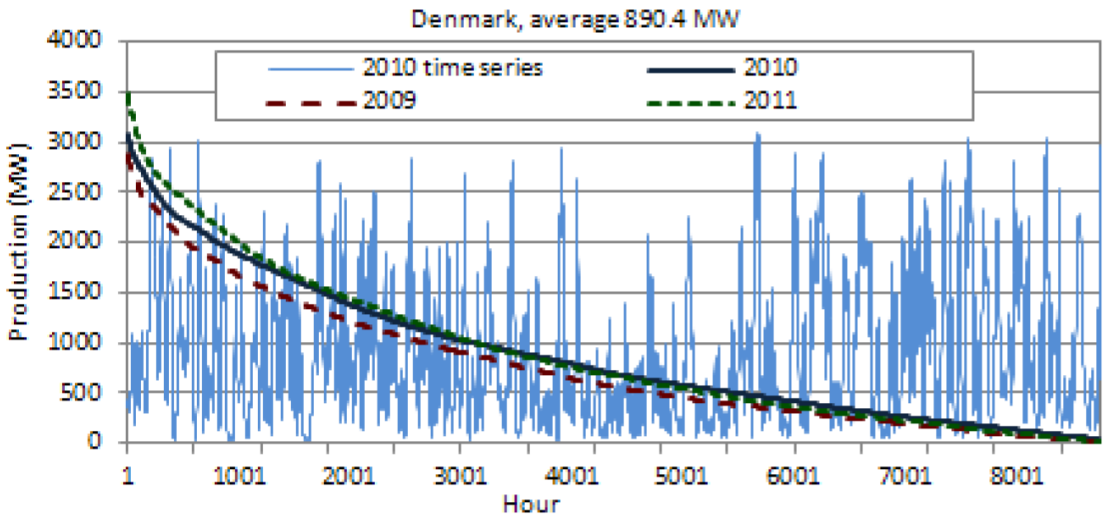

Figure 1.3 Wind power production in Denmark, 2010 [4].

power produced by wind in Denmark. Unfortunately, with renewable energy sources, power demand does not generally mirror power production. It is therefore desirable to be able to store excess energy in a stable form that would be available for later use. Figure 1.4 shows energy density (volumetric and gravimetric) for various forms of energy

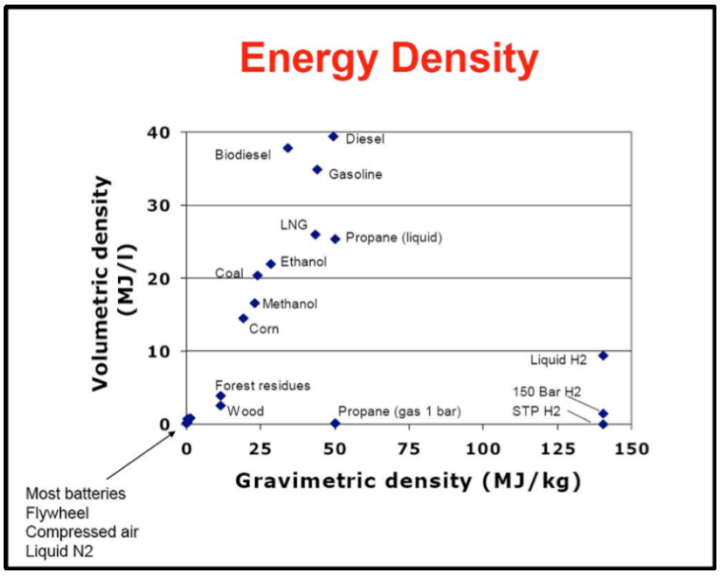

Figure 1.4 Volumetric and gravimetric energy densities of various fuels [5].

storage. Not surprisingly, gasoline and diesel fuels rank favorably in term of both volumetric and gravimetric energy density. Less favorable but still viable are methanol and ethanol. Methanol has the advantage of being a simple molecule, easy to synthesize, and has been proposed as a H_2/energy storage medium for excess power generated by renewables.

One way of efficiently tapping the energy stored in alcohols is through hydrogen fuel cells. (A possible application of such a system is shown in Figure 1.5.) The research in our group has involved the extensive study of the catalytic behavior of the Pd/Zn system [6-21], primarily for the steam reforming of methanol to form H_2 for fuel cell use.

There are 2 possible reactions that lead to H_2 formation from methanol:

$$\boldsymbol{CH_3OH + H_2O \rightarrow CO_2 + 3H_2}$$ methanol steam reforming (MSR) **Equation 1.1**

$$\boldsymbol{CH_3OH \rightarrow CO + 2H_2}$$ methanol decomposition **Equation 1.2**

The MSR reaction (no CO formation) is desirable for H_2 fuel cell applications because CO is a fuel cell poison. When catalyzed by Pd metal, CO is the primary carbon product. However, earlier work by Iwasa [22, 23], determined that tetragonal PdZn was the active phase for the MSR reaction, producing CO_2 as the primary product, and therefore the desirable phase in a MSR/fuel cell system.

1.3. Automobile Catalysts

By far, the primary use of platinum and palladium is in catalytic converters for automobiles, where they are typically used as "3-way" catalysts. The reactions catalyzed by these metals are 1) oxidation of CO to CO_2 2) oxidation of hydrocarbons 3) and

reduction of NO_x. For our work, we chose to focus on reaction 1) (CO oxidation) as a reportedly structure-insensitive [24] reactivity probe to characterize our alumina-supported palladium samples.

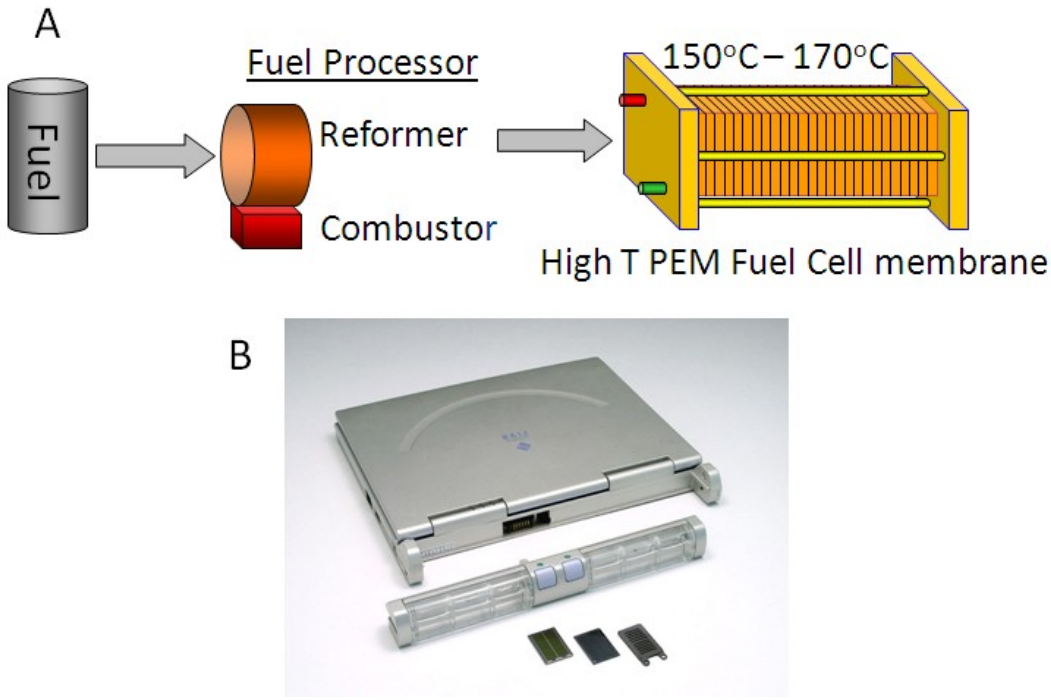

Figure 1.5 Schematic illustration of a proton exchange membrane (PEM) fuel cell (A) and a laptop computer (B) that could be powered by such a device.

As early as 1925, inventors were experimenting with "catalytic mufflers", using platinum as a catalyst and intended specifically for the mitigation of internal combustion engine emissions [35]. Research and development continued over the decades, and in 1954 Eugene J. Houdry filed for a U.S. patent for a precursor to the modern catalytic

converter, which was awarded in 1958 [36]. An early catalytic converter is shown in Figure 1.6

Despite the early interest in internal combustion engine exhaust mitigation, little was done in the way of the commercial implementation of this technology. The major hurdle to overcome was the elimination of the tetra ethyl lead anti-knock additive to gasoline. Lead serves as irreversible poison to the PGM catalysts, coating the catalyst surface. In 1973 [37], it was mandated that Pb-additives be phased out of gasoline sold in the U.S. In the mid 1970's catalytic converters began to be required for new cars. This

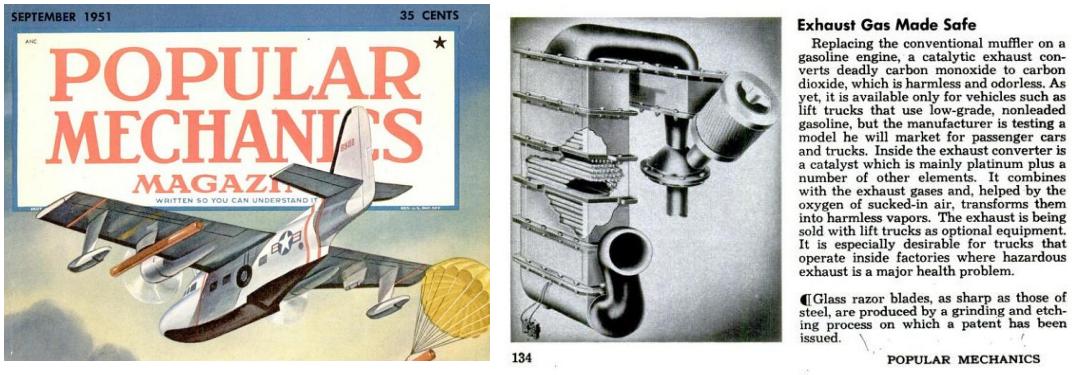

Figure 1.6 An early catalytic converter.

mandate, coupled with mandatory fuel economy measures, led to significant improvements in air quality in the U.S. over the next 3 decades, in spite of a doubling in the number of miles driven by Americans over that same period (Figures 1.7 and 1.8). Similar reductions in other automobile-related pollutants were also achieved with the implementation of these policies, coupled with technological advances. The current technological challenge is the problem of "cold start" emissions (Figure 1.9). Because

todays catalytic converters are not functional below 200 ˚C, the development of robust catalysts that are active in the ambient to 200 ˚C temperature range would help to address this issue.

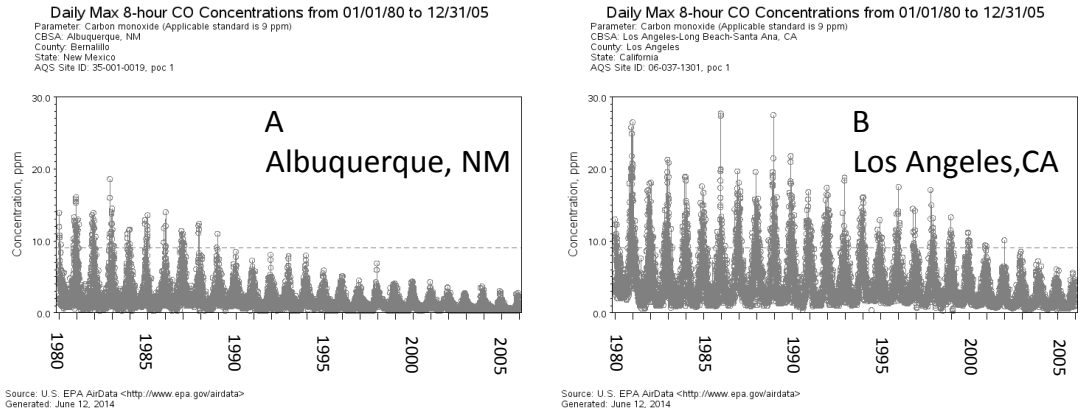

Figure 1.7 Local carbon monoxide concentrations measured at monitoring stations in Albuquerque, NM (A) and Los Angeles, CA (B) [38].

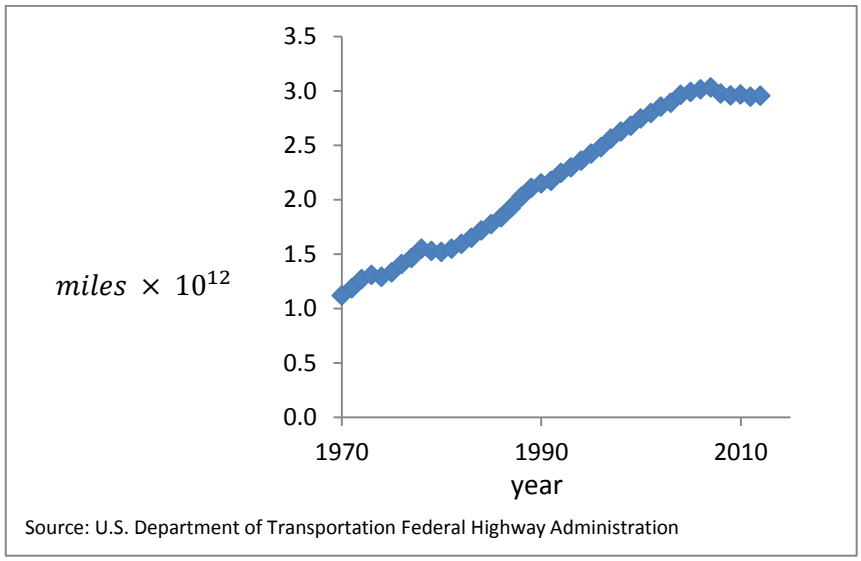

Figure 1.8 Trillions of miles driven by Americans by year [1].

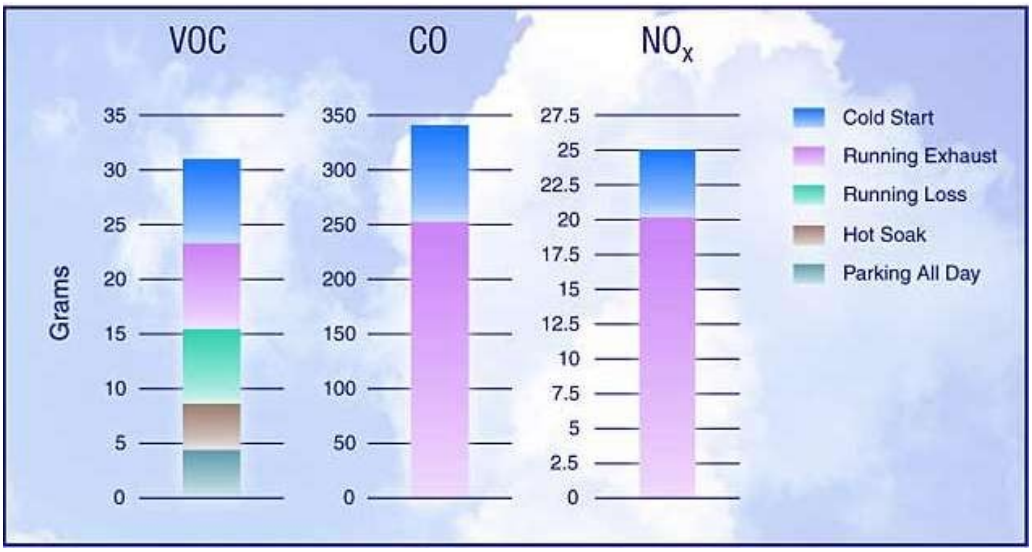

Figure 1.9 Volatile organic compounds (VOC), CO and NO_x emissions during cold start and optimum conditions, assuming 7 trips/day and 4 miles/trip. Estimated for a typical car on the road in 2002 [39].

1.4. CO oxidation mechanisms

The mechanism for CO oxidation on PGM's has been studied extensively [40] and is classified as a Langmuir-Hinshelwood mechanism, characterized by the following elementary steps: 1) Adsorption of reactant molecules onto the surface. 2) Dissociation and migration of adsorbates on the surface. 3) Reaction between adsorbed species. 4) Desorption of reactants from the surface. A problem with Pd and Pt is that at room temperature, CO covers the catalyst surface and is so strongly bound (Fig. 1.10) so as to block the adsorption of oxygen, thereby preventing the Langmuir-Hinshelwood mechanism from operating. To be active at low temperatures a catalyst requirement would be that CO not be so strongly bound and/or that a different mechanism be dominant.

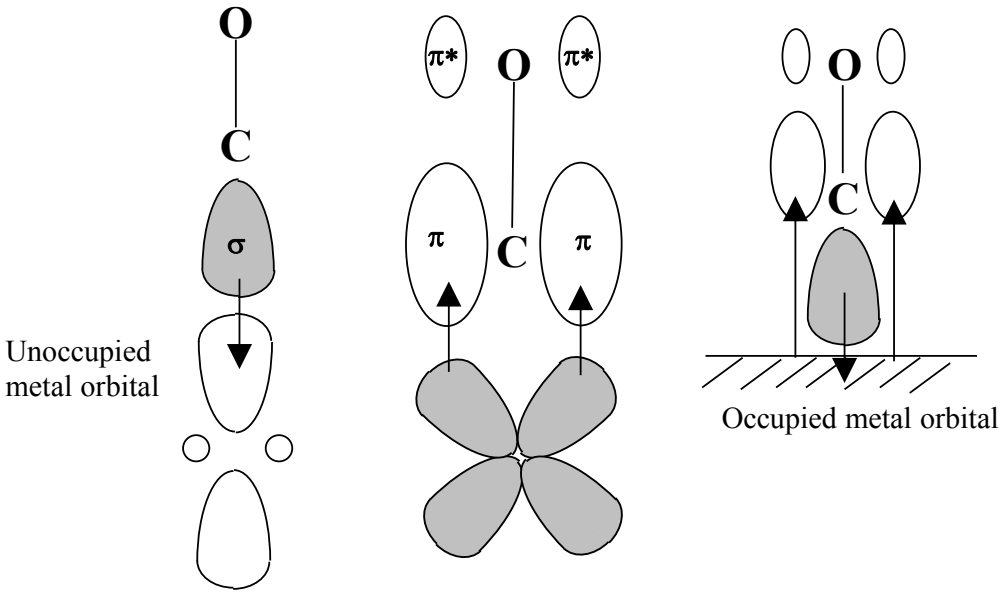

Figure 1.10 Adsorption of CO on a metal surface [41]. The strong adsorption of CO to Pd and Pt metal surfaces involves σ-bond electron donation from CO to the metal and back-bonding from the metal d-orbitals to the empty CO π molecular orbitals.

1.5. Scope of research

The work presented in this dissertation is divided into two parts: 1) Synthesis and structural characterization of bimetallic catalysts that are of interest for fuel cell applications (Chapters 3 and 4), and 2) Characterization of atomically-dispersed Pd on La-stabilized γ-alumina, which is of interest for automobile catalytic converters.

Chapter 3 is focused on the aerosol synthesis and structural characterization of tetragonal PdZn, which is of interest for methanol steam reforming for hydrogen production. Chapter 4 focuses on the measurement of constrained particle sizes and constitutional defects of bimodal-sized, templated Pt-Sn and Pt-Ru catalysts for ethanol oxidation. Finally, Chapter 5 focuses on the symbiotic relationship between atomically-

dispersed La and Pd, present on γ-alumina, a widely used, industrially relevant support. This chapter presents a novel image analysis technique for the chemical quantification of La/Pd atomically-dispersed mixtures, *operando* XAS/CO oxidation experiment results demonstrating the effect of the presence of La in a low-loading (0.5 wt%) Pd/γ-alumina catalyst. The low temperature activity observed for this catalyst, coupled with the measured reaction orders, indicates that the standard Langmuir-Hinshelwood mechanism for CO oxidation on Pd-metal is not appropriate. A surface structure model for the interaction of La and Pd on the γ-alumina (100) surface and a Mars-van Krevlen CO oxidation mechanism are proposed.

References

1. *Market Data Tables*. Platinum Today 2014 [cited 2014 June 13, 2014]; Available from: http://www.platinum.matthey.com/publications/market-data-tables.
2. *Market Report: Global Catalyst Market*, 2008 revised 2011, Acmite market intelligence.
3. Massalski, T.B., *Binary Alloy Phase Diagrams*. Second ed, ed. T.B. Massalski. Vol. 3. 1990, Materials Park, Ohio: Materials Information Soc.
4. Holttinen, H., et al., *Wind and load variability in the Nordic countries*. VTT TECHNOLOGY 96 2013, Finland: VTT Technical Research Centre of Finland 98.
5. Rapier, R. *The Key to Running the World on Solar and Wind Power*. 2013 [cited 2014 July 7, 2014]; Available from: http://www.energytrendsinsider.com/2013/04/30/the-key-to-running-the-world-on-solar-and-wind-power/.
6. Karim, A., T. Conant, and A. Datye, *The role of PdZn alloy formation and particle size on the selectivity for steam reforming of methanol.* Journal of Catalysis, 2006. **243**(2): p. 420-427.
7. Zhang, H., et al., *The Influence of ZnO Facets on Pd/ZnO Catalysts for Methanol Steam Reforming.* ACS Catalysis, 2014.
8. Johnson, R.S., et al., *The CO oxidation mechanism and reactivity on PdZn alloys.* Physical Chemistry Chemical Physics, 2013. **15**(20): p. 7768-7776.
9. Halevi, B., et al., *Catalytic reactivity of face centered cubic PdZn< sub> α</sub> for the steam reforming of methanol.* Journal of Catalysis, 2012. **291**: p. 44-54.
10. Halevi, B., et al., *Bimetallic Zn Alloys for the Electrooxidation of Hydrazine in Alkaline Media.* Meeting Abstracts, 2011(16): p. 1019-1019.
11. Smith, G.K., et al., *Initial steps in methanol steam reforming on PdZn and ZnO surfaces: Density functional theory studies.* Surface Science, 2011. **605**(7): p. 750-759.
12. Peterson, E.J., et al., *Aerosol synthesis and Rietveld analysis of tetragonal (β< sub> 1</sub>) PdZn.* Journal of Alloys and Compounds, 2011. **509**(5): p. 1463-1470.
13. Smith, G.K., et al. *Initial steps in methanol steam reforming on PdZn surfaces*. in *ABSTRACTS OF PAPERS OF THE AMERICAN CHEMICAL SOCIETY*. 2010. AMER CHEMICAL SOC 1155 16TH ST, NW, WASHINGTON, DC 20036 USA.
14. Lebarbier, V., et al., *The effect of PdZn particle size on reverse-water–gas-shift reaction.* Applied Catalysis A: General, 2010. **379**(1): p. 3-6.
15. Datye, A.K., et al. *Bimetallic PdZn catalysts for the steam reforming of methanol*. in *ABSTRACTS OF PAPERS OF THE AMERICAN CHEMICAL SOCIETY*. 2009. AMER CHEMICAL SOC 1155 16TH ST, NW, WASHINGTON, DC 20036 USA.
16. Burton, P.D., et al., *Morphological Dependence of ZnO on Methanol Steam Reforming Activity in Pd/Zno Catalysts.* The 2008 Annual Meeting, 2008.

17. Burton, P.D., et al., *Synthesis and activity of heterogeneous Pd/Al2O3 and Pd/ZnO catalysts prepared from colloidal palladium nanoparticles.* Topics in Catalysis, 2008. **49**(3-4): p. 227-232.
18. Conant, T., et al., *Stability of bimetallic Pd–Zn catalysts for the steam reforming of methanol.* Journal of Catalysis, 2008. **257**(1): p. 64-70.
19. Dagle, R.A., et al., *PdZnAl catalysts for the reactions of water-gas-shift, methanol steam reforming, and reverse-water-gas-shift.* Applied Catalysis A: General, 2008. **342**(1): p. 63-68.
20. Lebarbier, V., et al., *CO/FTIR spectroscopic characterization of Pd/ZnO/Al2O3 catalysts for methanol steam reforming.* Catalysis Letters, 2008. **122**(3-4): p. 223-227.
21. Karim, A., T.R. Conant, and A. Datye, *Monometallic Pd Supported on Zno: Highly Selective Towards Co2 in Steam Reforming of Methanol.* The 2006 Annual Meeting, 2006.
22. Iwasa, N., et al., *Dehydrogenation of Methanol to Methyl Formate over Supported Ni, Pd and Pt Catalysts - Anomalous Catalytic Functions of Pdzn and Ptzn Alloys.* Reaction Kinetics and Catalysis Letters, 1995. **55**(2): p. 245-250.
23. Iwasa, N., et al., *Steam Reforming of Methanol over Pd/Zno - Effect of the Formation of Pdzn Alloys Upon the Reaction.* Applied Catalysis a-General, 1995. **125**(1): p. 145-157.
24. Boudart, M.D.-M., G., *Kinetics of Heterogeneous Catalytic Reactions*. 1984, Princeton, NJ: Princeton University Press.
25. Schiff, J., ed. *Briefwechsel zwischen Goethe und Johann Wolfgang Döbereiner (1810-1830)* 1914, Bohlaus: Weimar. 144.
26. Ostwald, W., *Catalysis.* Physikalische Zeitschrift, 1901. **3**: p. 313-322.
27. Hofman, H.O. and W. Mostowitsch, *The reduction of calcium sulphate by carbon monoxide and carbon, and the oxidation of calcium sulphide.* Transactions of the American Institute of Mining and Metallurgical Engineers, 1911. **41**: p. 763-785.
28. Orlow, G., *The pyrogenetic oxidation of hydrogen and carbon monoxide through contact action.* Berichte Der Deutschen Chemischen Gesellschaft, 1909. **42**: p. 895-897.
29. Merrill, D.R. and C.C. Scalione, *The catalytic oxidation of carbon monoxide at ordinary temperatures.* Journal of the American Chemical Society, 1921. **43**: p. 1982-2002.
30. Ray, A.B. and F.O. Anderegg, *The oxidation of carbon monoxide by passage with oxygen or air through the silent discharge and over ozone decomposing catalysts.* Journal of the American Chemical Society, 1921. **43**: p. 967-978.
31. Rogers, T.H., et al., *The catalytic oxidation of carbon monoxide.* Journal of the American Chemical Society, 1921. **43**: p. 1973-1982.

32. Bray, W.C. and G.J. Doss, *The catalytic oxidation of carbon monoxide III. Catalytic efficiency of mixtures of dry manganese dioxide and cupric oxide.* Journal of the American Chemical Society, 1926. **48**: p. 2060-2064.
33. Hoskins, W.M. and W.C. Bray, *The catalytic oxidation of carbon monoxide. II. The adsorption of carbon dioxide, carbon monoxide, and oxygen by the catalysts, manganese dioxide, cupric oxide, and mixtures of these oxides.* Journal of the American Chemical Society, 1926. **48**: p. 1454-1474.
34. Draper, H.D., *The catalytic oxidation of carbon monoxide IV The pore volume of the catalysts manganese dioxide, copper oxide and mixtures of these oxides.* Journal of the American Chemical Society, 1928. **50**: p. 2637-2653.
35. Thompson, C.E. and R.E. Bissell, *Method of and apparatus for treating exhaust gases*, 1926, Google Patents.
36. Houdry, E.J., *Catalytic muffler*, 1958, Google Patents.
37. *EPA Requires Phase-Out of Lead in All Grades of Gasoline [EPA press release - November 28, 1973]*. 1973 [cited 2014 June 17, 2014]; Available from: http://www2.epa.gov/aboutepa/epa-requires-phase-out-lead-all-grades-gasoline.
38. *Air Data*. 2014 [cited 2014 June 12, 2014]; Available from: http://www.epa.gov/airdata/ad_viz.html.
39. Chary, K.V.R., et al., *Characterization and reactivity of Al2O3-ZrO2 supported vanadium oxide catalysts.* Journal of Molecular Catalysis a-Chemical, 2006. **243**(2): p. 149-157.
40. Ertl, G., *Reactions at surfaces: From atoms to complexity (Nobel lecture).* Angewandte Chemie-International Edition, 2008. **47**(19): p. 3524-3535.
41. McCash, E.M., *Surface Chemistry*. 1 ed. 2001, Great Clarendon Street, Oxford: Oxford University Press. 177.

Chapter 2 Materials and methods

2.1. Synthesis

In order to maximize catalyst efficiency, practical heterogeneous catalysts are generally composed of nanoparticles of catalyst supported on a high surface area support. The use of unsupported catalysts in real world applications would be inefficient because most catalysts do not lend themselves to the formation of stable high surface area monoliths. As a result, much of the catalyst would be buried in the monolith, unavailable for catalytic reactions. In many cases there is a symbiotic relationship between catalyst and support, with the support playing an active role in the catalyzed reaction. Supported catalysts may also contain additional phases that may also be catalytically active but selective to other, possibly undesirable products. In the case of the Pd-Zn-Al_2O_3 system for methanol steam reforming, the desired active catalyst, selective toward CO_2 as a product, is tetragonal PdZn. However, the actual supported catalyst may contain Pd metal (selective toward undesirable CO product formation), ZnO and Al_2O_3 in close proximity to each other (Figure 2.1). The presence of ZnO, and even the morphology of ZnO present [1] may influence this catalysts' behavior. To isolate the catalytic behavior of a catalyst, it is sometimes useful to examine the unsupported catalyst in as high of a specific surface area form as possible [2]. To do this for tetragonal PdZn, we employed aerosol powder synthesis [4] as a technique for the production of reasonably high surface

area phase-pure tetragonal PdZn for methanol steam reforming and CO oxidation reaction studies [5].

In contrast, the study of support effects on catalyst particle behavior requires the synthesis of extremely well-dispersed metals on a high surface area support. For these samples we relied on the dry impregnation or incipient-wetness technique (eg. [6]).

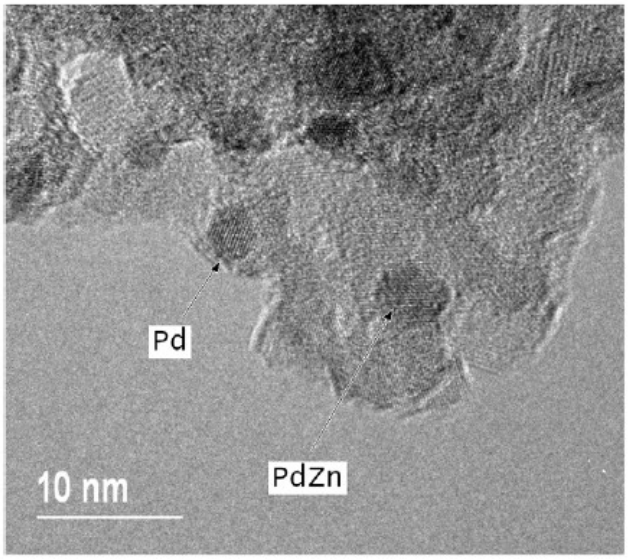

Figure 2.1 HRTEM image of Pd/ZnO/Al2O3 catalysts reduced at 250 ◦C. This image illustrates that both bulk PdZn and Pd nanoparticles can be identified within close proximity via cross-fringe analyses. It is also evident that the nanoparticles are not seen to be core-and-shell, although the EDX data shows a large variation between the near-edge and bulk compositions when reduced at this temperature [3].

2.1.1 *Aerosol synthesis*

The use of aerosol techniques for the production of metal an metal oxide powders is extensively described in the text by Kodas and Hampden-Smith [4]. A schematic showing the apparatus used for this work is shown below in Figure 2.2, and a photograph of the system is shown in Figure 2.3. A 10% nitric acid solution containing a stoichiometric composition of the desired composition is loaded into a container with a

plastic bottom, suspended in the reservoir of a Walgreen's brand ultrasonic humidifier. The humidifier vibrations are transduced through the plastic bottom to produce a fine mist of aerosol droplets of the nitrate

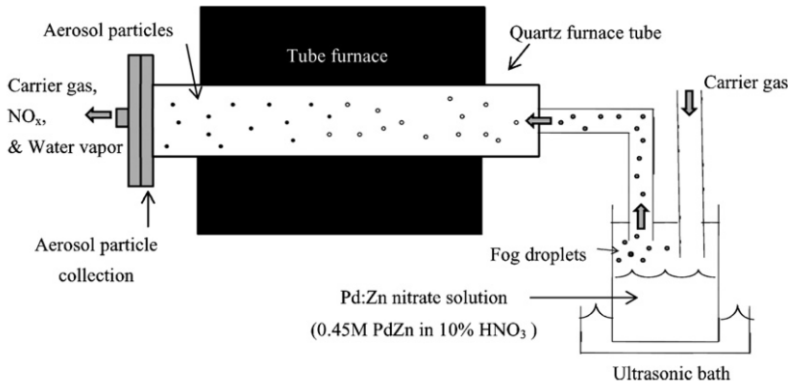

Figure 2.2 Schematic showing the apparatus used for aerosol powder production.

Figure 2.3 Photograph showing the aerosol reactor system.

solution. A carrier gas transports the droplets through a 3-zone furnace, where the fluid in droplets evaporates and nanoparticles of the desired composition are formed. The nanoparticles are captured on a filter placed at the furnace tube exit. The resulting

oxide/nitrate powder was then reduced in forming gas to produce single-phase tetragonal PdZn.

2.1.2 *Dry impregnation*

For the alumina support, Dispal (boehmite) from Sasol was calcined at 650 °C for 10 hr to make γ-alumina, and the BET surface area was determined to be 153 $m^2 g^{-1}$. The La-alumina support, containing 4 wt. % La_2O_3, was obtained from W. R. Grace (MI-386), and has a BET surface area of 176 $m^2 g^{-1}$. The BET surface areas were measured on a Micromeritics Gemini 2360 instrument under liquid nitrogen at 77K. Samples were prepared by dry impregnation of γ-alumina powders with a solution of palladium amine nitrate, diluted to the appropriate concentration to achieve 0.5 wt.% Pd-loading after three impregnations. Samples were dried at 110 °C after each impregnation, and finally calcined at 700 °C for 1 hour in a box furnace in ambient air. The temperature was raised at a slow rate 2 °C/minute to help generate the best dispersion of the Pd oxide phase.

2.2. Characterization

2.2.1 *X-ray diffraction*

Following the discovery of X-rays by William Roentgen in 1895 Max von Laue and Paul Ewald speculated that a crystal might serve as a diffraction grating for electromagnetic radiation, providing that radiation of a short enough wavelength could be employed. Max von Laue further postulated that X-rays might be composed of electromagnetic waves of the desired wavelength. Von Laue went on to conduct the experiment, shining poly chromatic X-rays on a crystal of copper sulfate backed with a

photographic plate. Upon developing the plate, von Laue observed diffraction spots arrayed around the spot left by the primary beam[7, 8]. Further work by W.H. and W.L. Bragg[9] established the field of X-ray crystallography.

The intensity of X-rays scattered by a single electron follows the Thomson equation:

$$\boldsymbol{I_e = I_0 \left(\frac{e^4}{R_0^2 m^2 c^4}\right)\left(\frac{1+cos^2 2\theta}{2}\right)} \qquad \textbf{Equation 2.1}$$

Where: I_e =scattered X-ray intensity

I_0 =incident X-ray intensity

e =electron charge

m =electron mass

c =speed of light in vacuum

2θ =angle between incident and scattered beams

The trigonometric term is the polarization factor. Building on this, the intensity equation for the powder diffractometer is:

$$\boldsymbol{I = |F^2| p \left(\frac{1+cos^2 2\theta}{sin^2 \theta cos\theta}\right)} \qquad \textbf{Equation 2.2}$$

The trigonometric term is the combined Lorentz and polarization factor. The parameters from the Thomson equation are incorporated into the scattering factors, f_n, in the structure factor expression below. The structure factor, F,is the Fourier summation of the electron density in the unit cell:

$$\boldsymbol{F = \sum_n f_n e^{2\pi i(hx+ky+lz)}} \qquad \textbf{Equation 2.3}$$

Where: n =the total number of atoms in the unit cell

f_n =the scattering factor of the nth atom

h, k, l = the Miller indices of the reflection of interest

x, y, z =the atomic coordinates of each atom in the unit cell

The relation of scattering angle, θ, and the distance between planes of atoms in a crystal is Bragg's Law:

$$\boldsymbol{\lambda = 2dsin\theta} \qquad \textbf{Equation 2.4}$$

Where: λ =wavelength of the X-ray

d spacing between planes of atoms

2θ =angle between incident and scattered beams

From the diffractometer intensity equation and the Bragg equation, it is possible to obtain information on a crystal's unit cell size (from d-spacings) and the positions and average electron density of atoms in the unit cell (from intensities).

Crystallite size information can be obtained from the widths of the Bragg diffraction peaks through the Sherrer equation:

$$< \boldsymbol{L} >= \frac{\boldsymbol{k\lambda}}{\boldsymbol{\beta cos\theta}} \qquad \textbf{Equation 2.5}$$

Where: $< L >$=the coherent diffracting distance in a given direction in the crystal

k =the Sherrer constant (usually 0.9)

β=peak FWHM width (with instrumental broadening subtracted)

$\theta = \frac{1}{2}$ the diffraction angle, 2θ

Microstrain can also be a source of peak broadening in diffraction patterns. Because microstrain broadening has a different 2θ dependence than crystallite size broadening, the two can be separated using the Williamson-Hall relation:

$$\boldsymbol{\beta cos\theta = \frac{k\lambda}{<L>} + 4\varepsilon sin\theta} \qquad \textbf{Equation 2.6}$$

Where the variables are the same as above, plus:

ε =microstrain, $\frac{\Delta L}{L}$

More details regarding theoretical and experimental aspects of X-ray diffraction can be found in the books by Cullity[10] and Klug and Alexander[11]. Further discussion of size/strain measurement can be found in the Rietveld analysis section below.

2.2.2 *Neutron diffraction*

The same considerations as X-ray diffraction, described above, can be extended to neutron diffraction, with the difference being that neutrons scatter off of the atomic nuclei instead of scattering off of the electrons. The primary result of this is that while X-ray scattering factors vary monotonically with atomic number, Z, neutron scattering have no such dependence. Whereas X-ray scattering factors for elements close to each other in Z, neutron scattering factors can be widely different for atoms adjacent to each other in Z, and even for different isotopes of the same element. The corollary is that elements widely separated in Z may have very similar neutron scattering factors. Another aspect of neutron scattering is that, since scattering is off of the nucleus, this technique is very sensitive to atom position, and therefore atom vibrational amplitudes, making for accurate determination of Debye-Waller parameters.

2.2.3 *Rietveld analysis*

In 1967 a method was proposed by Hugo Rietveld, involving the nonlinear least squares fitting of crystallographic variables to neutron diffraction peak position and intensity data[12]. The method, now known as Rietveld analysis, has been expanded to include X-ray diffraction data and has proven to be a powerful tool in the analysis of X-ray and neutron powder diffraction data. The Rietveld analysis software employed in this work was GSAS[13].

Variables that are typically refined by this method are lattice constants, atom positions and electron density on those positions, and peak shape variables associated with crystallite size and microstrain (see above). An additional option is the refinement of anisotropic microstrain parameters using the model of Stephens [14], which is a phenomenologically-based model. With this approach, strain parameters are chosen and refined with regard to the crystal system of the phase of interest. From the refined parameter values, a strain isosurface can be computed and displayed (Fig. 2.4)

2.2.4 *X-ray absorption spectroscopy (XAS)*

The discovery of X-rays, coupled with von Laue's discovery of diffraction and the Braggs work with crystals as X-ray spectrometers, formed the experimental foundation for X-ray absorption spectroscopy (XAS)[15]. Einstein's theory on the photoelectric effect[16], coupled with advances in quantum mechanics in the 1920's provided a theoretical basis for the interpretation of X-ray absorption edge data, which

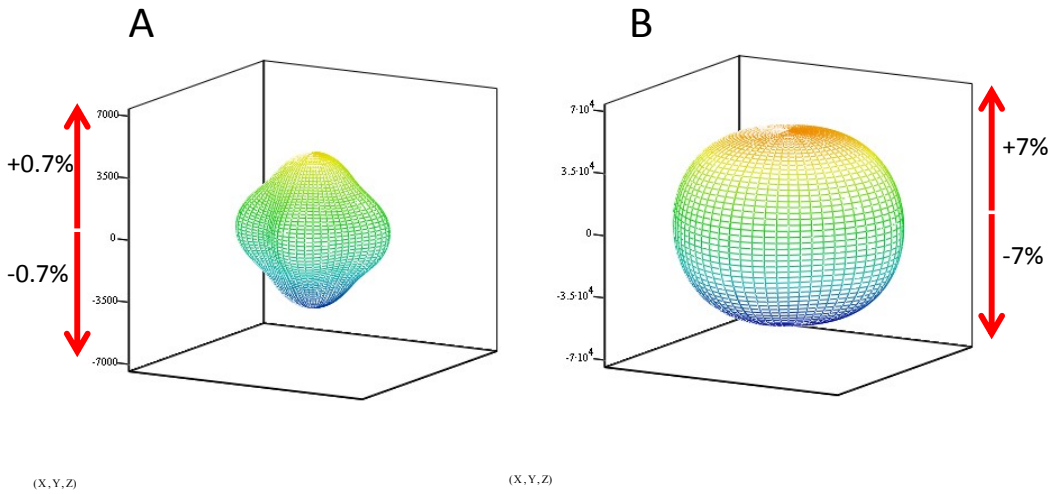

Figure 2.4 Microstrain isosurfaces for A) ZnO and B) PdO. Data was collected in situ at 300 ˚C under flowing air using an Anton-Parr XRK900 heating stage attached to a Rigaku SmartLab diffractometer.

was beginning to be collected in the 1920's. Work on the quantitative understanding of the oscillations observed in absorption edge data was active in the late 1920's and early 1930's[17-21]. However, it wasn't until the availability of intense X-ray sources at synchrotron facilities in the late 1960's and early1970's that this technique was available for routine materials characterization[22]. It was also at about this time that the theory regarding extended x-ray absorption fine structure (EXAFS) was refined[23].

This technique involves the measurement of the absorption of X-rays by a material over an X-ray energy range that includes the absorption edge of an element in the material. This absorption is described by Beer's Law:

$$\boldsymbol{I = I_0 e^{-\mu t}} \qquad \textbf{Equation 2.7}$$

Where: I =transmitted intensity

I_0 =incident intensity

μ =linear absorption coefficient (cm^{-1})

t =sample thickness (cm)

At the absorption edge, the incoming X-rays are of the energy sufficient to eject a core electron from its orbital (the photoelectric effect). At energies above the absorption edge, the photoelectron has enough energy to scatter off of the electrons present in the orbitals of neighboring atoms, causing oscillations in the X-ray absorption (Fig. 2.5). The intensity oscillations in the EXAFS (designated $\chi(E)$) region can be converted to reciprocal (k) space ($\chi(k)$)using the following formula:

$$\boldsymbol{k = \sqrt{\frac{2m}{\hbar^2}(E - E_0)}} \qquad \textbf{Equation 2.8}$$

Where: k =reciprocal space dimension ($Å^{-1}$)

m =electron mass

E =photon energy

E_0=electron binding energy

$\hbar = \frac{h}{2\pi}$; h =Planck's constant

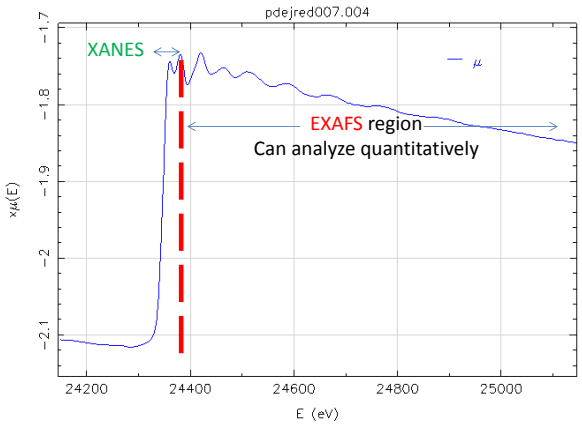

Figure 2.5 X-ray absorption data collected at the palladium K-edge from an alumina-supported palladium catalyst, showing the edge step, the X-ray absorption near edge (XANES) region, and the extended X-ray absorption fines structure (EXAFS) region.

The EXAFS equation, relating k-space ($Å^{-1}$) to R-space (Å) is shown below:

$$\chi(k) = \sum_j \frac{N_j f_j(k) e^{-2k^2\sigma_j^2}}{kR_j^2} \sin\left(2kR_j + \delta_j(k)\right) \qquad \textbf{Equation 2.9}$$

Where: k =reciprocal space dimension ($Å^{-1}$)

N_j = number of neighboring atoms (coordination number or CN)

$f_j(k)$ and $\delta_j(k)$ scattering properties of the neighboring atoms

σ=Debye-Waller factor (vibrational amplitude in $Å^{-1}$)

The Fourier transform of the χ(k) data (Fig. 2.6) provides a function that is similar to a radial distribution function, showing electron density variation as a function of radial distance It is not exactly a radial distribution function because it incorporates multiple scattering distances as well as a phase shift, $\delta_j(k)$. To a first order approximation, the peak intensities are proportional to the number of nearest neighbor atoms. The analysis of

this data, using the software packages Athena and Artemis, provides quantitative estimates of the number of nearest neighbors, or coordination numbers, for each shell of

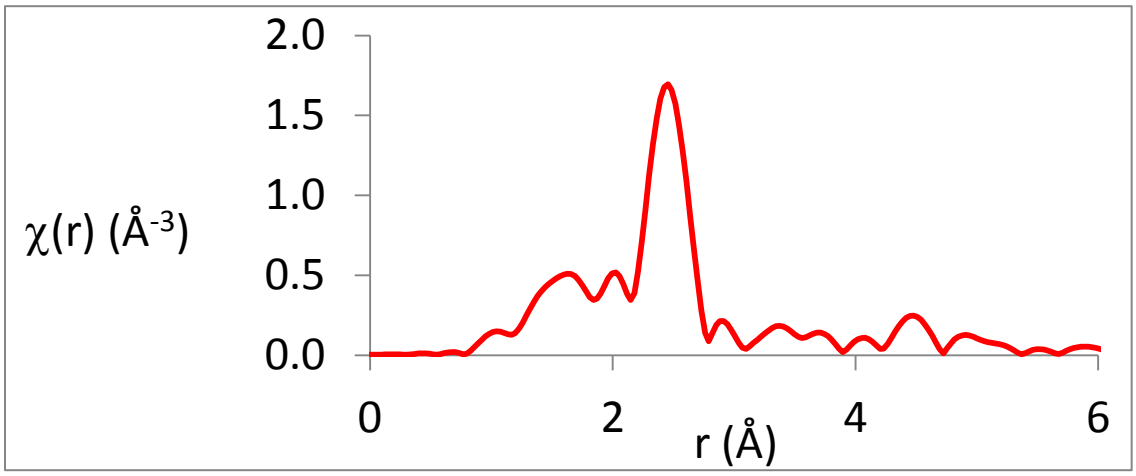

Figure 2.6 The Fourier transform of χ(k) data obtained at the palladium K-edge from an alumina-supported palladium catalyst.

atoms surrounding the absorbing atom, as well as distances to nearest neighbor atoms from the absorbing atom, and the Debye-Waller factors for those atoms. The first-shell coordination number can be used to obtain an estimate of particle size by solving the following equation for R[24]:

$$\boldsymbol{N_{particle}} = \left[\mathbf{1} - \frac{\mathbf{3}}{\mathbf{4}}\left(\frac{\boldsymbol{r}}{\boldsymbol{R}}\right) + \frac{\mathbf{1}}{\mathbf{16}}\left(\frac{\boldsymbol{r}}{\boldsymbol{R}}\right)^{\mathbf{3}}\right]\boldsymbol{N_{bulk}} \qquad \textbf{Equation 2.10}$$

Where: $N_{particle}$ =first shell coordination number obtained from the analysis

N_{bulk} =first shell coordination number of bulk material (12 for F.C.C. metal)

r =atom radius

R =particle radius

2.2.5 *Operando X-ray absorption spectroscopy*

Operando XAS experiments were performed on the highly-dispersed, low Pd-loaded catalysts on γ-alumina and La-stabilized γ-alumina. For catalysts, operando X-ray absorption spectroscopy involves the collection of XAS data under actual catalyst working conditions while simultaneously monitoring the catalyst performance. We performed this experiment at Argonne National Laboratory's Advanced Photon Source beamline 10-ID. The experimental setup is shown in Figure 2.7

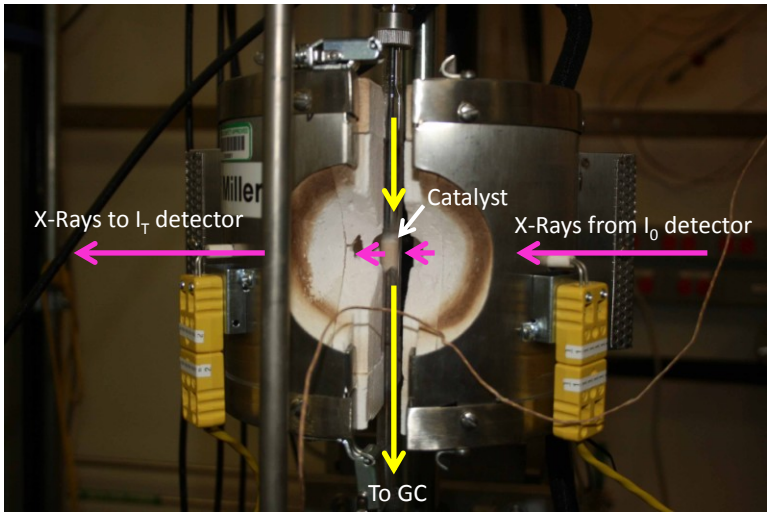

Figure 2.7 Operando XAS experimental setup. An NMR tube in a clamshell furnace is packed with a glass wool supported catalyst bed. X-rays pass through a hole in the furnace, are transmitted though the catalyst bed and continue to a detector (pink lines). A reaction gas composed of 1% CO/He flows through the catalyst bed and on to a gas chromatograph, where the exit gas composition is measured (yellow lines). (The cut-out in the furnace is for the insertion of a detector for measuring X-ray fluorescence signal, which was not used in this experiment.)

2.3. Image analysis

In high angle annular dark field mode, images collected by aberration-corrected electron microscopes are routinely capable of showing distinct single-atoms on a support having sufficient Z (atomic number) contrast. The atom images result from Rutherford backscattering of the electron beam by the atom nuclei, with the backscatter intensity being approximately related to the square of the atomic number of the atom involved in the backscattering, ($Z^{1.7}$)[25]. It is therefore possible to determine the elemental identity of individual atoms in an image through the analysis of image intensities. This has been done in the case of boron, nitrogen, and carbon on a boron nitride support [25] (Fig. 2.8).

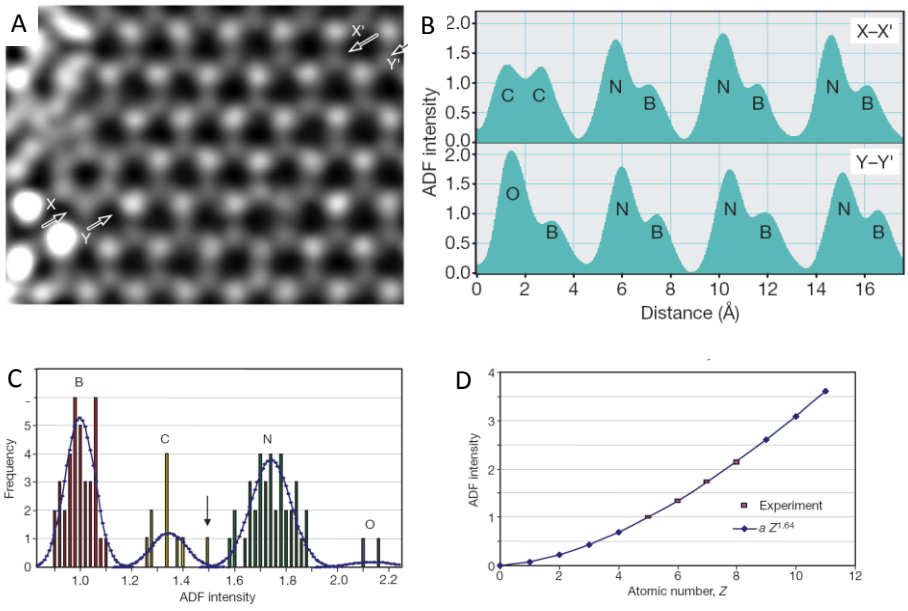

Figure 2.8 A) Aberration-corrected image of B, C, and N in a BN monolayer (Corrected for distortion, smoothed, and deconvolved to remove probe tail contributions to nearest neighbours). B) Intensity variation along traverses X-X' and Y-Y' in A. C) Histogram showing well-resolved intensity distributions for B, C, N, and O. D) Intensity variation as a function of Z [25].

However, this is an example of what information can be gleaned under ideal circumstances, ie. uniform monolayer sample. The case of our supported-metal catalysts was less ideal; the support was composed of flakes of La-stabilized γ-alumina that were covered by Pd nanoparticles as well as an atomically-dispersed high Z species. Because the samples were composed of particles rather than monolayers, the background intensities were quite variable, making the extraction of atom image intensities difficult.

The La in La-stabilized γ-alumina has been shown by to exist as an atomically-dispersed surface species [26]; our question was whether there was atomically-dispersed Pd present as well. To determine this, we performed intensity analysis of La-stabilized γ-alumina (no Pd) and La-stabilized γ-alumina with a 2.5 wt% Pd loading (Fig. 2.9)
The steps of the image analysis are shown in Figure 2.10. The images were first processed using ImageJ software [27] with smoothing using a Gaussian blur filter followed by background subtraction, and regions of interest were identified (white boxes in Figs. 2.10A and B). The regions of interest were converted to false color intensity maps (Fig. 2.10C) and 2-D Gaussian functions were fit to the intensities using MATLAB software [28] (Fig. 2.10D). By performing a least squares fit of Gaussian functions to the intensities, the effects of image noise were averaged out, and the tails of the Gaussian peaks served to account for residual background intensity. The distributions of the intensity measurements, obtained from the images in Figure 2.9 are shown in the histograms in Figure 2.11 A-D below. From the histograms in Figure 2.10, it is apparent that the atomically-dispersed species seen in the 2.5wt% Pd/La-stabilized γ-alumina sample is composed of Pd and La.

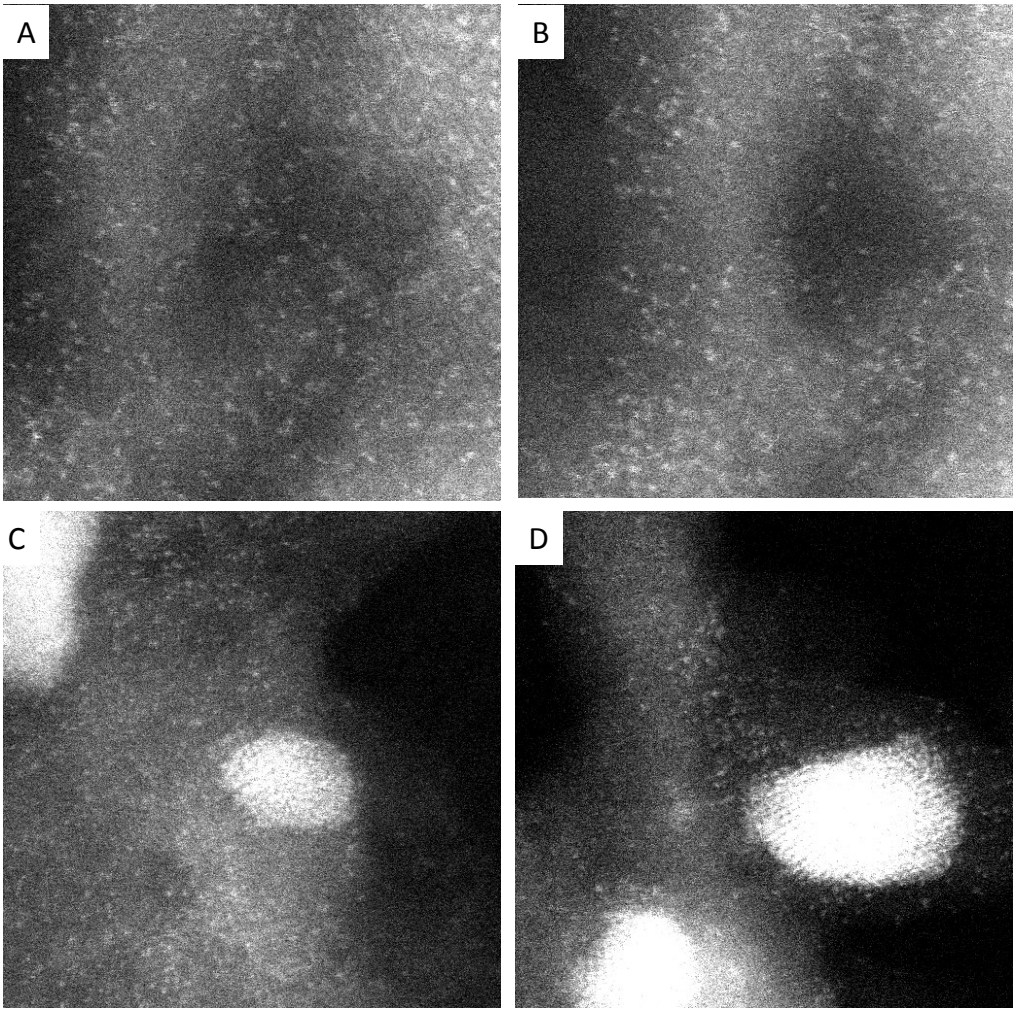

Figure 2.9 Aberration-corrected high angle annular dark field STEM images obtained from La-stabilized γ-alumina (A-B) and 2.5 wt% Pd on La-stabilized γ-alumina (C-D).

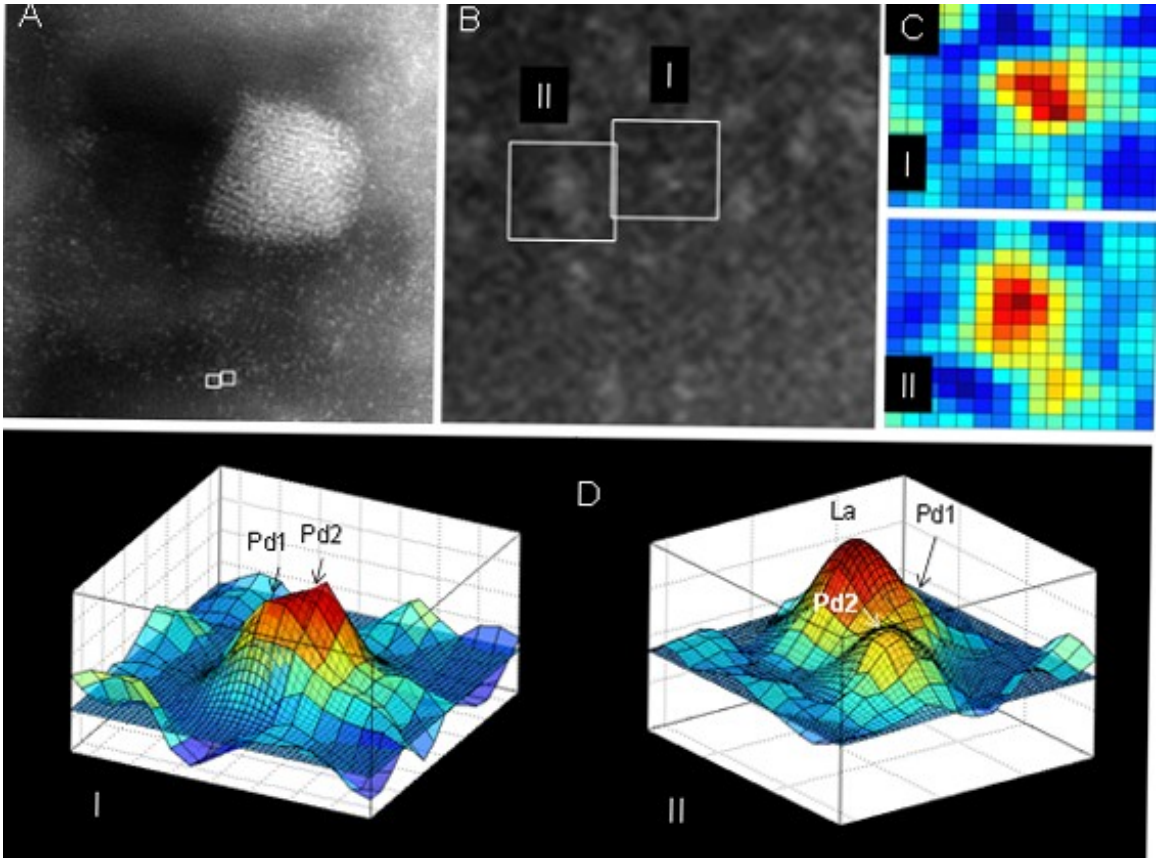

Figure 2.10 Intensity analysis of ACEM images obtained from a La-stabilized γ-alumina support sample with a 2.5 wt.% Pd-loading. **(A)** A typical region of the sample, with a Pd-metal particle surrounded by atomically dispersed Pd and La. **(B)** An enlarged region from **(A)**, showing two regions containing atomically dispersed species. **(C)** Colorized intensity maps from regions I and II. **(D)** 2-D Gaussian-function fits (fine-mesh) to the intensity maps in **(C)**.

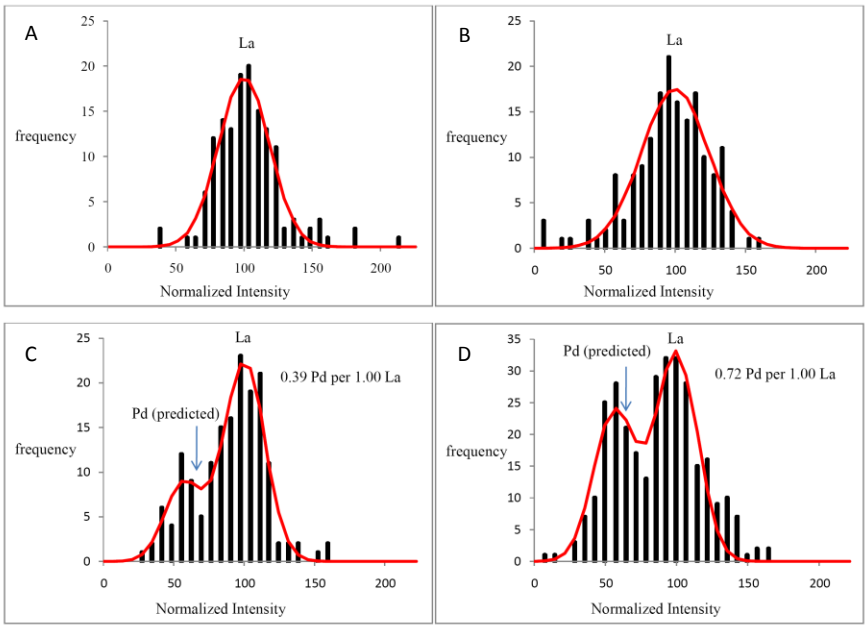

Figure 2.11 Intensity distributions obtained from atomically-dispersed species shown in the images in Figure 2.9. Data shown in histograms A and B were obtained from La-stabilized γ-alumina (no Pd) and histograms C and show data obtained from a 2.5% Pd-loaded La-stabilized γ-alumina sample. The intensities were normalized such that the peak of the high-Z intensity data is 100. The predicted position of Pd is based on the $Z^{1.7}$ relationship of intensities [25].

References

1. Burton, P.D., et al., *Morphological Dependence of ZnO on Methanol Steam Reforming Activity in Pd/Zno Catalysts.* The 2008 Annual Meeting, 2008.
2. Halevi, B., et al., *Aerosol-Derived Bimetallic Alloy Powders: Bridging the Gap.* The Journal of Physical Chemistry C, 2010. **114**(40): p. 17181-17190.
3. Conant, T., et al., *Stability of bimetallic Pd–Zn catalysts for the steam reforming of methanol.* Journal of Catalysis, 2008. **257**(1): p. 64-70.
4. Kodas, T.T. and M.J. Hampden-Smith, *Aerosol processing of materials*. 1999, New York: Wiley-VCH.
5. Peterson, E.J., et al., *Aerosol synthesis and Rietveld analysis of tetragonal (β< sub> 1</sub>) PdZn.* Journal of Alloys and Compounds, 2011. **509**(5): p. 1463-1470.
6. Huang, Y.J. and J.A. Schwarz, *The effect of catalyst preparation on catalytic activity .3. The catalytic activity of Ni/Al2O3 catalysts prepared by incipient wetness.* Applied Catalysis, 1987. **32**(1-2): p. 45-57.
7. Friedrich, W., P. Knipping, and M.v. Laue, *Interferenz-Erscheinungen bei Röntgenstrahlen*. 1912, Munich: Sitzungsberichte der Mathematisch-Physikalischen Classe der Königlich-Bayerischen Akademie der Wissenschaften zu München. 303.
8. Laue, M.v., *X-radiation interferences.* Physikalische Zeitschrift, 1913. **14**: p. 1075-1079.
9. Bragg, W.H. and W.L. Bragg, *The reflection of X-rays by crystals.* Proceedings of the Royal Society of London Series a-Containing Papers of a Mathematical and Physical Character, 1913. **88**(604): p. 428-428.
10. Cullity, B.D., *Elements of x-ray diffraction*. 2nd ed. Addison-Wesley series in metallurgy and materials. 1978, Reading, Mass: Addison-Wesley Pub. Co. 555.
11. Klug, H.P. and L.E. Alexander, *X-ray diffraction procedures for polycrystalline and amorphous materials*. 2nd ed. 1974, New York: Wiley. 996.
12. Rietveld, H.M., *Line profiles of neutron powder-diffraction peaks for structure refinement.* Acta Crystallographica, 1967. **22**: p. 151-&.
13. Larson, A.C. and R.B. VonDreele, *General Structure Analysis System (GSAS)*, 2004, Los Alamos National Laboratory Report LAUR 86-748.
14. Stephens, P.W., *Phenomenological model of anisotropic peak broadening in powder diffraction.* Journal of Applied Crystallography, 1999. **32**: p. 281-289.
15. Vonbordwehr, R.S., *A history of X-ray absorption fine-structure.* Annales De Physique, 1989. **14**(4): p. 377-466.
16. Einstein, A., *Generation and conversion of light with regard to a heuristic point of view.* Annalen Der Physik, 1905. **17**(6): p. 132-148.
17. Kronig, R.D., *On the theory of fine structure in the X-ray absorption spectra.* Zeitschrift Fur Physik, 1931. **70**(5-6): p. 317-323.

18. Kronig, R.D., *On the theory of fine structure in the X-ray absorption spectrum. 2.* Zeitschrift Fur Physik, 1932. **75**(3-4): p. 191-210.
19. Kronig, R.D., *On the theory of fine structure in the X-ray absorption spectrum 3.* Zeitschrift Fur Physik, 1932. **75**(7-8): p. 468-475.
20. Kronig, R.D. and H.A. Kramers, *On the Theory of Absorption and Dispersion in the X-Ray Spectra.* Zeitschrift Fur Physik, 1928. **48**(3-4): p. 174-179.
21. Kronig, R.D.L., *On the theory of dispersion of x-rays.* Journal of the Optical Society of America and Review of Scientific Instruments, 1926. **12**(6): p. 547-557.
22. Lytle, F.W., *The EXAFS family tree: a personal history of the development of extended X-ray absorption fine structure.* Journal of Synchrotron Radiation, 1999. **6**: p. 123-134.
23. Sayers, D.E., E.A. Stern, and F.W. Lytle, *New technique for investigating noncrystalline structures - fourier analysis of extended x-ray - absorption fine structure.* Physical Review Letters, 1971. **27**(18): p. 1204-&.
24. Calvin, S., et al., *Determination of crystallite size in a magnetic nanocomposite using extended x-ray absorption fine structure.* Journal of Applied Physics, 2003. **94**(1): p. 778-783.
25. Krivanek, O.L., et al., *Atom-by-atom structural and chemical analysis by annular dark-field electron microscopy.* Nature, 2010. **464**(7288): p. 571-574.
26. Wang, S.W., et al., *Dopants adsorbed as single atoms prevent degradation of catalysts (vol 3, pg 143, 2004).* Nature Materials, 2004. **3**(4): p. 274-274.
27. Schneider, C.A., W.S. Rasband, and K.W. Eliceiri, *NIH Image to ImageJ: 25 years of image analysis.* Nature Methods, 2012. **9**: p. 671-675.
28. *MATLAB release 2010b*, 2010, The MathWorks, Inc: Natick, Massachusetts, United States.

Chapter 3 Aerosol synthesis and Rietveld analysis of tetragonal (β1) PdZn

Abstract

The β1 PdZn intermetallic of nominal 50:50 Pd:Zn at% was synthesized using an aerosol method. The aerosol method provided atomically mixed precursor oxy-nitrate powder that was then reduced to form β1 PdZn, having a surface area amenable to catalytic measurements. Formation of the β1 PdZn during reduction was found to occur rapidly (4 h) and at moderate temperature (500 ◦C), serving to minimize the loss of volatile Zn. Chemical and structural characterization confirms that β1 PdZn (95–99 wt% phase pure) of the same composition as the nitrate feedstock solution can be prepared using this method. Detailed structural analysis shows that this material contains little or no vacancies and minimal Pd/Zn disorder.

3.1. Introduction

The tetragonal PdZn intermetallic compound of approximate composition 50% (atomic) Zn is currently of interest as a methanol steam reforming (MSR) catalyst for proton exchange membrane (PEM) fuel cells [1]. The catalyst used for this reaction is Pd supported on ZnO, but the PdZn phase forms in-situ during reduction in H_2 and also during reaction, since H_2 is a product of methanol steam reforming [2]. The conversion of Pd to PdZn causes the MSR reaction to switch from 100% selectivity toward CO (on Pd) to nearly 100% selectivity towards CO_2 [3]. This is of crucial importance in the case of

PEM fuel cells, as CO is a known poison in this application. The catalyst that is currently in use commercially for this application is ZnO-supported Cu. It has been noted that PdZn exhibits a similar valence electron density of states (DOS) to that of Cu metal, and suggested that this is the reason for the observed similarity in catalytic behavior between the two phases [4, 5]. However, Cu metal suffers from deactivation with time, a result of surface area loss due to sintering of the metal particles. The PdZn catalyst can be regenerated easily, making it a viable alternative [2].

The PdZn phase is therefore of interest for the MSR reaction; however, XRD and TEM show that the working catalyst contains Pd, PdZn and ZnO phases [6]. It is difficult to identify the role of each of these phases in supported catalysts. Furthermore, the relatively low abundance of the PdZn compared to that of the ZnO support makes it difficult to acquire high quality structural data . It was therefore decided to synthesize bulk, unsupported PdZn for structural characterization by X-ray and neutron powder diffraction methods. A requirement was that the bulk PdZn possess sufficient surface area for reasonable catalytic measurements, precluding traditional monolithic metallurgical synthesis techniques such as arc melting. Volatility of Zn under reducing conditions is an additional challenge during synthesis of PdZn phases of controlled composition. With these factors in mind, an aerosol synthesis route [7] was chosen for the production of bulk PdZn powder. The resulting material was then examined by Rietveld analysis coupled with electron microprobe analysis. Because defects are known to play an important role in many catalytic systems, attention was focused on evaluation of the type and quantity of

defects in β_1 PdZn. These experiments were augmented with density-functional-theory calculations to independently investigate the energetics of Pd ⇔ Zn disorder in β_1 PdZn.

An additional motivation for this work was the lack of an accurate experimental reference X-ray diffraction pattern for β_1 PdZn. The current X-ray diffraction reference patterns for β_1 PdZn are an experimental pattern (PDF number 00-006-0620) and a calculated pattern (PDF number 01-072-2936). Both patterns are based on the same reference [8], yet disagree with one another as to relative peak intensities. In this paper we present experimental data that is in good agreement with the calculated pattern.

3.2. Experimental

The PdZn precursor powder was synthesized using an aerosol method employing a metal nitrate feed solution. A 1:1 Pd:Zn nitric acid solution was prepared by mixing equimolar volumes of Pd and Zn dissolved in nitric acid. The Pd-nitrate solution was obtained from Aldrich, and was composed of 4.5 wt% Pd in 10 volume % nitric acid. An equimolar solution of Zn was prepared by weighing and dissolving $Zn(NO_3)_2 \cdot 6H_2O$ (Aldrich) in 10 volume % nitric acid. Equal volumes of Pd and Zn solutions were measured into a flask using an Ependorff pipette to produce 1:1 PdZn in 10-volume % nitric acid. A schematic diagram of the aerosol system is shown in Figure 3.1.

The aerosol vapor was produced by immersing a cylindrical glass tube, with a plastic diaphragm on the bottom, into the water reservoir of a Walgreen-brand ultrasonic humidifier. The ultrasonic waves propagating through the plastic diaphragm produced a

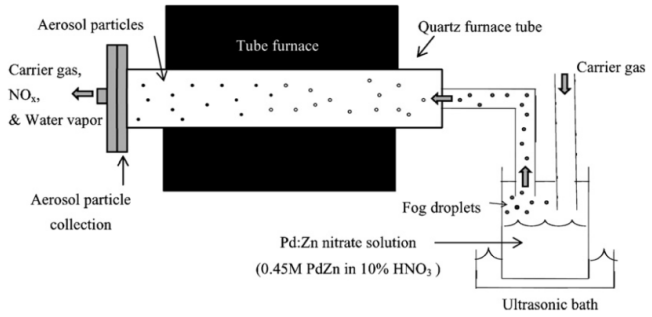

Figure 3.1 A schematic diagram of the aerosol powder synthesis apparatus. The ultrasonic vibrations from the ultrasonic bath are transmitted to the Pd-Zn nitrate solution via a plastic diaphragm, causing the formation of fog droplets.

fog of metal nitrate droplets, which were swept from the glass tube by a nitrogen carrier gas flowing at 1 liter per minute through a 80 cm-long 3-zone tube furnace with a 2.54 cm O.D. quartz furnace tube. The furnace zone temperatures were set at 800 °C at the furnace entrance zone, 800 °C in the middle, and 550 °C at the exit zone. During the transit through the furnace, the solvent in the fog droplets was lost, converting droplets into roughly spherical solid particles. The reactor system was allowed to run until approximately 90% of the nitrate solution was expended. The damp powder was collected at the furnace exit on a filter, where it was allowed to dry, under flowing N_2, after the aerosol generator was turned off. The resulting cake was scraped from the filter paper and then subjected to a reduction treatment (4 hours at 500 °C in 5% H_2 / balance N_2).

The powder surface area was determined by Nitrogen adsorption at 77 K using a Micromeritics Gemini System and Quantachrome Autosorb 1-C/TCD. The samples were outgassed at 120°C for 5+ hrs under vacuum before measurements. The surface areas

were determined from adsorption values using a five point BET analysis at P/P_0 ranging from 0.05 to 0.2. Thermogravimetric analysis (TA model STQ600) was performed on the as-produced aerosol powder under atmospheres of air, N_2, and H_2/N_2. Scanning electron microscopy (SEM) images of the PdZn powder were acquired using a Hitachi S-5200 SEM. The powder was ground lightly in an alumina mortar and pestle to break up clumps, and then pressed onto carbon double-stick tape that had been adhered to an aluminum sample holder. Secondary and backscatter electron images of the polished mount were also collected using an FEI FIB operating at 30 keV. Electron probe microanalysis (EPMA) was performed on a pressed pellet of the PdZn powder that had been mounted in epoxy and polished, with increasingly finer grits, down to 0.3 μm-grit Al_2O_3 polishing compound. The sample was coated with a 15-20 nm thick layer of evaporated carbon, which was nominally the same thickness of carbon coating on the standards that were used in the analysis. Data was collected using a JEOL 8200 microprobe operating at 20 kV and 20 nA with a takeoff angle of 40 degrees. Quantitative analysis was performed using wavelength dispersive spectrometry, employing pentaerythritol (PETL) , lithium fluoride (LIFH), and layered dispersive element (LDE1) crystal monochromators for the measurement of the Pd L-α, Zn K-α, and O-Kα peaks, respectively.. Standard intensities were measured from elemental Pd and $ZnAl_2O_4$ standards, and the pulse-height analyzer for the spectrometer measuring the O-Kα peak (0.525 keV) was optimized to minimize interference from the Pd Mγ peak (0.522 keV). A ZAF correction was applied to the data to account for the effects of atomic number, absorption, and secondary fluorescence. To obtain a representative

chemical characterization of the sample, analyses were collected on a grid, with 50 μm spacing between grid points.

Neutron powder (NPD) diffraction was performed on the HIPD instrument at the Los Alamos Neutron Science Center. Time-of-flight neutron data was collected at 4 K from detector banks at ± 14°, ± 40°, ± 90° and ± 153°. X-ray diffraction data was then collected at room temperature on the same sample using a Rigaku Ultima III theta-theta diffractometer equipped with a Cu-target X-ray tube (Cu K-α_1 = 1.540562 Å, Cu K-α_2 = 1.544390 Å) [9] and a graphite monochromator for the removal of Cu K-β radiation. The sample was loaded into a zero-background sample holder, and data was collected over a scan range of 5-148 degrees two theta with a step size of 0.02 degrees and a scan rate of 0.1 degrees/minute. To obtain an accurate room temperature lattice parameter, a portion of the sample was then mixed with silicon standard SRM640b and a second X-ray diffraction data set was collected using a Scintag PADV theta-two theta diffractometer, also equipped with a Cu-target X-ray tube and a graphite monochromator. The sample was distributed in a thin layer on a lightly-greased quartz zero background plate, and data was collected over a range of 20-95 degrees two theta with a step size of 0.02 degrees and a count time of 12 seconds per step. Rietveld analysis of the neutron and X-ray powder diffraction data was performed using the software package GSAS[10], employing an anisotropic microstrain model in the peak profile function [11]. In the case of the neutron Rietveld refinements, only data from the four high angle detector banks was used (± 90 and ± 153 degrees), due to their relatively high resolution (0.5% and 0.3%, respectively)

compared to that of the four low angle detector banks (± 14(3%) and ± 40 (1.0%) degrees). X-ray and neutron scattering factors [12] are listed in Table 3.1. It is apparent that while for X-ray scattering there is good contrast between Pd and Zn, in the case of neutron scattering there is only slight contrast between these two elements.

Table 3.1 X-ray (XRD) atomic number and Neutron (NPD) scattering lengths and cross-sections.

	Z	bound coherent scattering length (fm)	bound coherent scattering cross section (barn)	total bound scattering cross section (barn)
Pd	46	5.91	4.39	4.48
Zn	30	5.680	4.054	4.131
ratio	1.5	1.04	1.08	1.08

We augmented our experiments with first-principle calculations that are based on density-functional-theory [13] as implemented in the periodic structure software package VASP [14-16]. Electronic exchange and correlations were treated at the GGA level within the parameterization of Perdew, Burke, and Ernzerhof [17]. The interactions between electrons and nuclei was described within the PAW formalism [18, 19]. The electronic configurations (core radii in atomic units in parenthesis) were $5s^2 4p^6 3d^8$ (2.300 a_B), $3d^{10}4s^2$ (2.300 aB), for Pd, and Zn, respectively. The Fermi-level was slightly broadened using 1st order Methfessel and Paxton broadening (σ=0.1 eV)[20], a typical value for metallic systems. All calculations were performed using a cutoff energy of Ecut=600 eV which was found to be sufficient to obtain converged results. The density of the k-point mesh [21] was adjusted such that results were converged to within 1 meV/atom. For $Pd_{50}Zn_{50}$ in the conventional four atom cell we employed a 16x16x16 k-point grid. In order to investigate site-disorder in $Pd_{50}Zn_{50}$ we employed 2x2x2 supercells of the tP4 representation of this phase, containing a total of 32 atoms, and a 8x8x8 k-

point grid. During geometry optimization all degrees of freedom, lattice parameters and internal coordinates were relaxed simultaneously. The component PAW potentials were tested for elemental Pd and Zn metals. The optimized equilibrium lattice parameter for fcc-Pd is a=3.958 Å (16x16x16 k-point grid), consistent with previous work [5], and for elemental hcp-Zn (19x19x11 k-point grid), we obtain a=2.665 Å, and c=4.954 Å. For comparison the experimental lattice parameters are, a=3.891 Å, and a=2.665 Å and c=4.947 Å, for fcc-Pd and hcp-Zn, respectively [22]. This 1-2% overestimation of the lattice parameters is typical for calculations at the GGA-level [19].

3.3. Results and Discussion

3.3.1 *Powder characterization*

Figure 3.2 shows the results of TGA analysis of an as-produced aerosol powder under air, N_2, and H_2/N_2. Onset of reduction of PdO to Pd metal was observed at 650° C under N_2, and at 800 ° C under air. In the H_2/N_2 mixture, complete reduction of ZnO and PdO was observed to have occurred by 400° C with weight loss, resulting from Zn volatility, becoming apparent after approximately 900° C. Based on these TGA results, the as-produced aerosol powder was reduced in flowing H_2/N_2 in a furnace at 500° C for 4 hours to produce the PdZn phase.

Figure. 3.3 shows secondary electron images of the aerosol powder after reduction. The BET surface area of the powder was 4.7 m^2/g, corresponding to

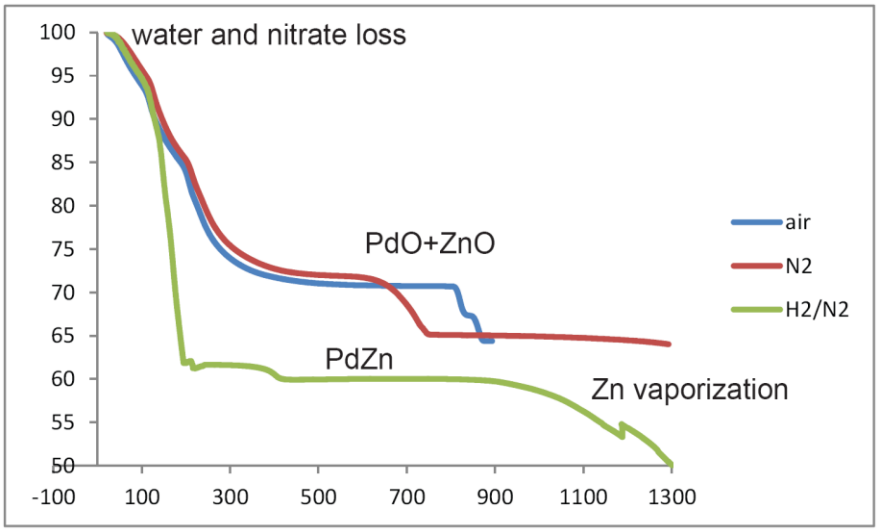

Figure 3.2 Thermogravimetric analyzer (TGA) data obtained from as-produced PdZn aerosol powder.

a 126 nm mean particle diameter [23], which is consistent with the SEM image. Electron backscatter and secondary electron images of the polished sample are shown in Figure 3.4. The electron backscatter image is sensitive to average atomic number differences, with Pd-rich regions appearing as lighter-shade areas in the backscatter image. Electron microprobe analyses were performed at grid points as shown in Figure. 3.4A. Electron microprobe results are summarized in Table 3.2, and Figure. 3.5 is a histogram showing the distribution of Zn compositions, with a mean of 49.6 at% Zn, which is quite close to the nominal, as- prepared composition of 50 at% Zn. The Pd-rich regions were found to be approximately 1at% richer in Pd than average. The standard deviation of 100 electron microprobe analyses was found to be 0.3 % (atomic), yielding a 95% confidence limit of

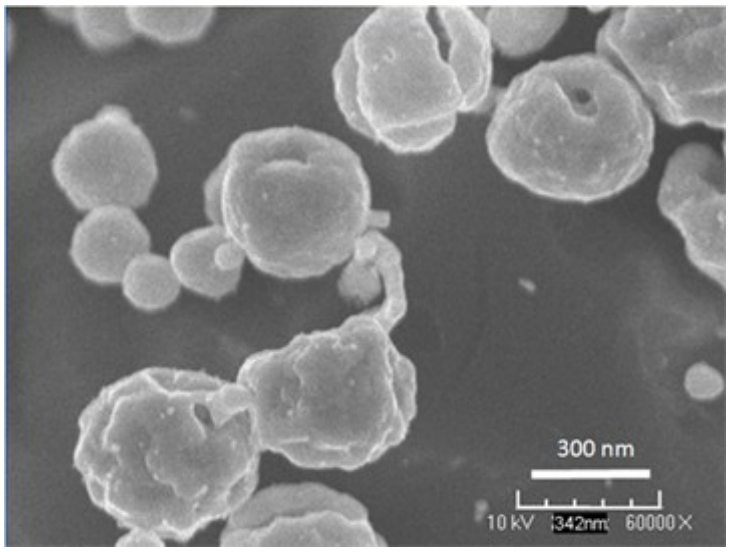

Figure 3.3 Scanning electron micrograph (secondary electron image) of the PdZn aerosol powder, reduced at 500° C for 4 hours in 5%H_2/N_2.

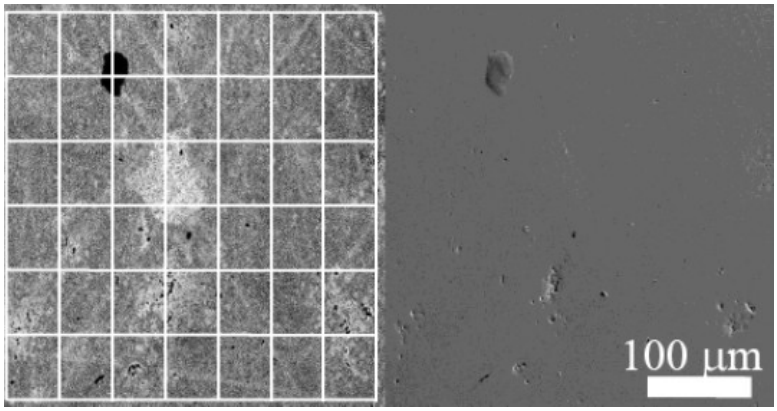

Figure 3.4 Backscatter electron (A) and secondary electron (B) images of the polished PdZn surface. Electron microprobe analyses were collected on the grid at 50 μm steps. Light regions are approximately 1at% rich in Pd over the mean value of 50.4 at% Pd.

Table 3.2 Electron microprobe analysis results. Average of 100 analyses (±1σ).

	Pd	Zn	O	Total
Wt%	60.8(5)	36.7(4)	3.2(4)	100.7(5)
At%	50.4(3)	49.6(3)		100

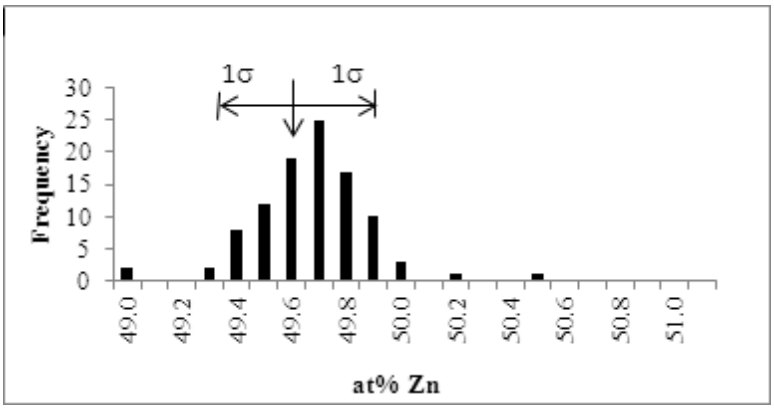

Figure 3.5 Mean chemical composition ($\bar{x}$) and chemical variation ($\pm 1\sigma$) of the aerosol powder, reduced at 500° C for 4 hours in 5%H_2/N_2. Analyses were performed on grids at 50 μm intervals.

±0.06%, demonstrating that the aerosol method is capable of creating powders of a uniform chemical composition that is essentially identical to that of the feedstock nitrate solution. The approximately 3% oxygen (weight) in the analysis is likely due to the presence of a surface oxide. Because the crystallite sizes were significantly smaller than the approximately 1 μm^3 electron probe excitation volume, these results represent the average bulk chemical composition of the sample.

3.3.2 *Structural characterization*

Figure 3.6A shows the X-ray diffraction data (degrees 2θ), and Figure 3.6B is a comparison of the X-ray diffraction data to the neutron diffraction data (d-space (Å)), with the observed and the calculated and difference plots from the final Rietveld

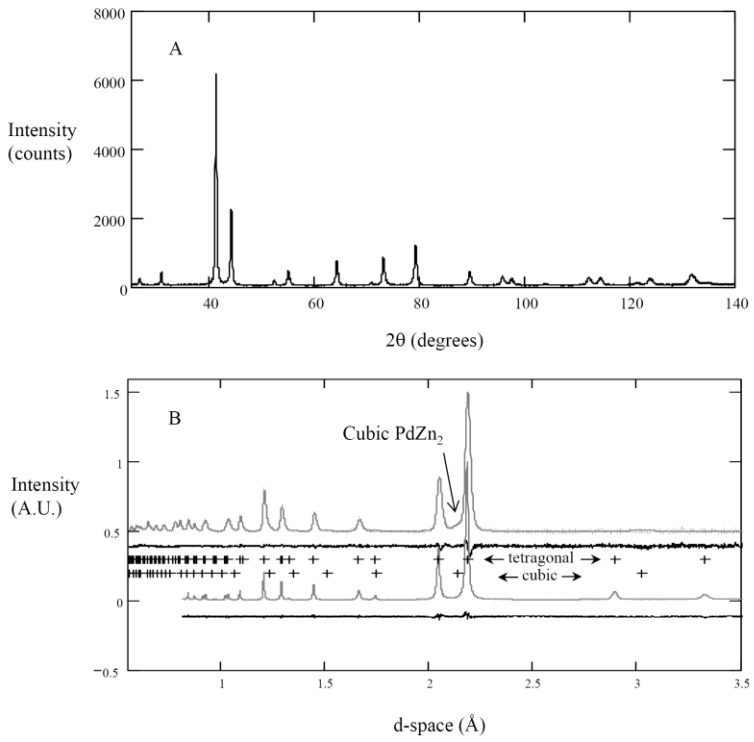

Figure 3.6 Diffraction patterns. **(A)** XRD pattern for tetragonal PdZn. **(B)** Observed, calculated and difference plots for the detector bank-4 neutron data (upper) and the X-ray data (lower). The (+) markers show peak positions for the tetragonal (upper) and cubic (lower) phases.

refinements. Although it was possible to fit all of the X-ray diffraction peaks using the tetragonal β_1 PdZn structure, small but distinct peaks in the neutron diffraction pattern at 2.14 and 1.51 Å were found to be consistent with the presence of a cubic phase, having a lattice parameter of 3.0234(5) Å.

3.3.2.1 Cubic phase

The PdZn phase diagram [24-27] shows that the tetragonal β_1 PdZn phase of interest is bracketed by the cubic β'' (Pd-rich) and β' (Zn-rich) [28] phases at

temperatures greater than 600-650 °C, and by lower symmetry δ (Pd-rich) [29] and ε (Zn-rich) [30] phases at room temperature [26]. The two un-indexed peaks in the neutron diffraction data could not be indexed by either of the room temperature phases, but were consistent in both position and intensity with one of the two cubic phases. The two cubic phases have been described as being Strukturbericht type B2 (CsCl), and to a first approximation can be thought of as the inverse of one another. Interestingly, the lattice parameters of these two phases are quite similar (3.04-3.06 Å for the Pd-rich phase and 3.04 Å for the Zn-rich phase), which is a consequence of the similarity of atomic size of Pd and Zn (1.40 and 1.35 Å, respectively) as well as electronic effects [31]. Unfortunately this precludes the identification of the correct phase by lattice parameter alone.

From refinements using the neutron data, the fraction of this phase was found to be 4.6 ± 0.7 wt%. The presence of this phase was not obvious in the X-ray diffraction data, nor was it apparent in SEM or BSE images. However, for consistency, the cubic phase was included in the refinements of the X-ray data, where the weight fraction was refined to be only 1.3 wt%, with the strongest peak from the cubic phase indistinguishable from the background. The possibility of neutrons having a greater sensitivity to the presence of the cubic phase than X-rays was addressed by comparing the ratio of calculated intensities for the cubic (110) peak and the tetragonal (101) peak (the most intense peaks for both phases), calculated for neutron and for X-ray diffraction. Structure factor calculations were performed for tetragonal PdZn (50 at% Zn) and both Pd-rich (33.3% Zn

(atomic)) and Zn-rich (66.7 at% Zn (atomic)) cubic phases. The sensitivity to detection of the cubic phase can be quantified by the ratio:

$$\frac{12\times F^2_{calc,cubic(110)}}{8\times F^2_{calc,tetragonal(101)}} = \frac{I_{calc,cubic(110)}}{I_{calc,tetragonal(101)}} \qquad \textbf{Equation 3.1}$$

Where 12 and 8 are the reflection multiplicity factors. For neutron scattering, the sensitivity ratios were found to be 1.32 and 1.26 for the Pd-rich and Zn-rich cubic phases, respectively; because of the similar neutron scattering cross-sections for Pd and Zn (Table 3.1), it is expected that neutron diffraction sensitivity to Pd-rich and Zn-rich phases with the same structure should be similar. In the case of X-ray scattering, the sensitivity ratios were 1.69 for the Pd-rich and 1.03 for the Zn-rich cubic phases, showing that X-ray scattering is more sensitive than neutron scattering to the presence of the Pd-rich cubic phase, but less sensitive than neutron scattering to the presence of the Zn-rich cubic phase. The observation that the cubic phase (110) peak is readily apparent in the neutron data, but less so in the X-ray data, suggests that the cubic phase in this sample is $PdZn_2$ (β'). An overall thermal parameter was refined for the cubic phase atoms.

3.3.2.2 Tetragonal phase (β_1)

The phase of interest for catalysis spans the composition range 37-56 at% Zn [24-27], has the AuCu prototype structure, and is commonly given the designation β_1. This phase carries the Strukturbericht designation $L1_0$ and the Pearson symbol tP2 or tP4, depending upon the unit cell chosen to describe the structure [4, 8]. The tP2 structure can be described as a tetragonally-distorted CsCl structure with Pd at the cell corners and a

Zn atom at the body center. Alternatively, the tP4 structure is comprised of a tetragonally-distorted pseudo F.C.C. structure with Pd occupying corner sites and the centers of two opposing faces, and Zn atoms occupy the centers of the four remaining faces. The difference between the tP2 and tP4 structures is that the latter structure allows more crystallographic degrees of freedom, with Pd atoms occupying two crystallographically independent sites. However, in either representation of the structure the atomic positions are fixed by symmetry. (The inverse structure could also be employed, exchanging Pd for Zn, with Zn occupying the two unique sites.) The tP2 structure was employed in our refinements. A feature of β_1 PdZn is its large compositional single phase stability range (36-56 at% Zn), suggesting that defects such as vacancies and/or antisite substitution of Pd for Zn and vice versa may be important in this phase. An anti-site substitution model has been proposed for non-stoichiometric β_1 PdZn on the basis of lattice parameter variation with Zn composition [32].

Because of the presence of finely divided, ~5 wt% cubic phase, the EPMA analysis is representative of the bulk composition, rather than the composition of the 1:1 PdZn phase. The EPMA composition can be corrected to represent that of the 1:1 PdZn phase if the composition of the cubic phase is known. In section 3.2.1 it was shown that the cubic phase composition is probably close to $PdZn_2$, so the bulk EPMA value was corrected accordingly to account for the presence of 5 weight % $PdZn_2$. For refinements using the neutron data, anisotropic thermal parameters for the Pd and Zn sites were used for the tetragonal β_1 phase. Because the neutron diffraction data was collected at 4 K, this

should represent a lower bound for the tetragonal β_1 PdZn thermal parameters. For refinements using the X-ray diffraction data, an isotropic overall thermal parameter was initially refined; however, this was found to result in an unrealistically small thermal parameter value, and the isotropic overall thermal parameter was also found to be correlated with the site occupancies. The thermal parameters in the refinement of the X-ray data were therefore fixed at the anisotropic thermal parameter values that had been obtained from refinement of the neutron data. Three site-occupancy models were used in the analysis of the X-ray and neutron diffraction data; (1) varying the Pd:Zn ratio via *anti-site* substitution of Pd for Zn and vice versa, (2) varying the Pd:Zn ratio via *vacancy* on either the Pd or the Zn-site, (3) holding the Pd:Zn ratio constant at 1:1 and exchanging Pd on the Pd-site with Zn on the Zn-site. For case (3), a *disorder* parameter was defined as follows:

$$\boldsymbol{disorder} = \frac{\boldsymbol{Pd_{Zn}+Zn_{Pd}}}{\boldsymbol{Pd_{Pd}+Zn_{Zn}}} \qquad \textbf{Equation 3.2}$$

Where Pd_{Pd} is the occupancy of Pd on the Pd-site, Zn_{Zn} is the occupancy of Zn on the Zn-site, Pd_{Zn} is the occupancy of Pd on the Zn-site, and Zn_{Pd} is the occupancy of Zn on the Pd-site. The three models are illustrated schematically in Figure 3.7.

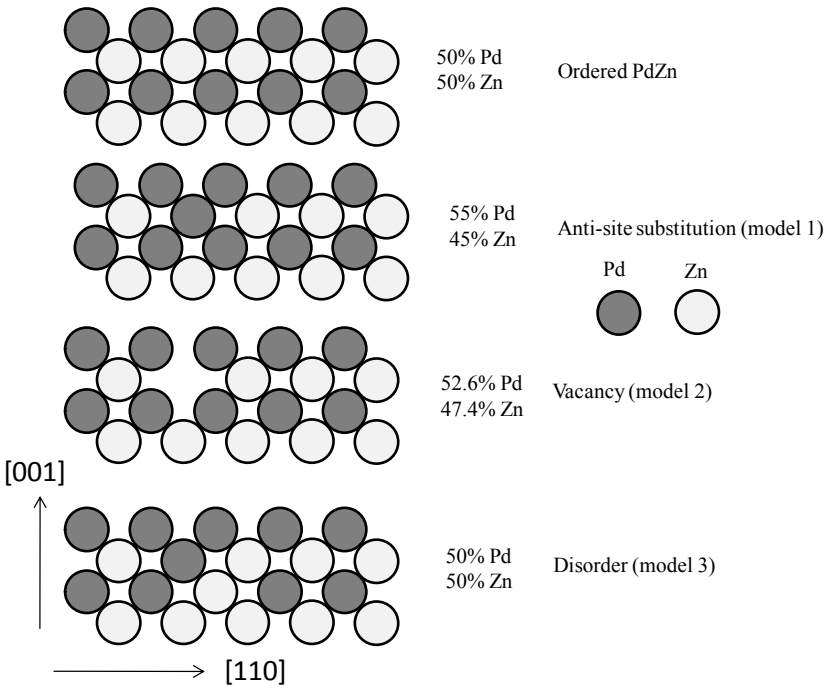

Figure 3.7 Possible variations of Pd and Zn atom arrangements in PdZn.

Because the X-ray scattering contrast between Pd and Zn is atomic number-dependent, X-ray diffraction Bragg peak intensities are expected to be sensitive to Pd/Zn-site disorder as well as anti-site substitution of Pd for Zn (and vice versa). X-ray peak intensities should also be sensitive to vacancies on the Zn-site (ie. Zn occupancy <1), but be unable to distinguish Pd-site vacancies from anti-site substitution of Zn for Pd. In the case of neutron scattering, however, scattering lengths and cross-sections are quite similar for Pd and Zn (Table 3.1). As a result, neutron diffraction Bragg peak intensities are relatively insensitive to site disorder or anti-site substitution in PdZn phases, but should be sensitive to vacancies on either the Pd or the Zn site, serving to complement the X-ray data. To test these models, Rietveld refinements were performed for a range of

fixed Pd:Zn compositions that were varied according to the three occupancy models described above. The minima in the goodness-of-fit (GOF) parameter (reduced χ^2), plotted as a function of composition, were compared to the known β_1 PdZn composition to evaluate the plausibility of each model.

Figure 3.8A shows the results of refinements using the anti-site Pd-Zn substitution model, compared to the chemical composition as measured by electron microprobe analysis (bulk composition) and as-corrected for the presence of 5 wt % $PdZn_2$ (β_1 PdZn composition). For a perfectly ordered PdZn specimen, one would expect a single GOF minimum, located at 50 at% Zn. In fact, two minima in the GOF data at approximately ±5 at% from the observed composition can be seen for the refinements of the XRD anti-site model data, and the observed composition is located at a local maximum in the GOF parameter, close to a composition of 50 at% Zn. This indicates that a model of perfectly ordered tetragonal PdZn does not adequately explain the data. The GOF for refinements of the neutron diffraction data, using model 1, was found to be independent of composition, as expected from the lack of Pd and Zn neutron scattering contrast. The results of refinements using the vacancy model are shown in Figure. 3.8B. For this model, a sharp minimum in the GOF parameter for the X-ray data refinements was found at a composition of 50.8 at% Zn. However, the observed β_1 PdZn composition lies a significant distance from the observed GOF minimum. Also, the GOF parameter for the refinements of the neutron diffraction data was found to be independent of composition for the vacancy model; if vacancies were a significant phenomenon in this sample,

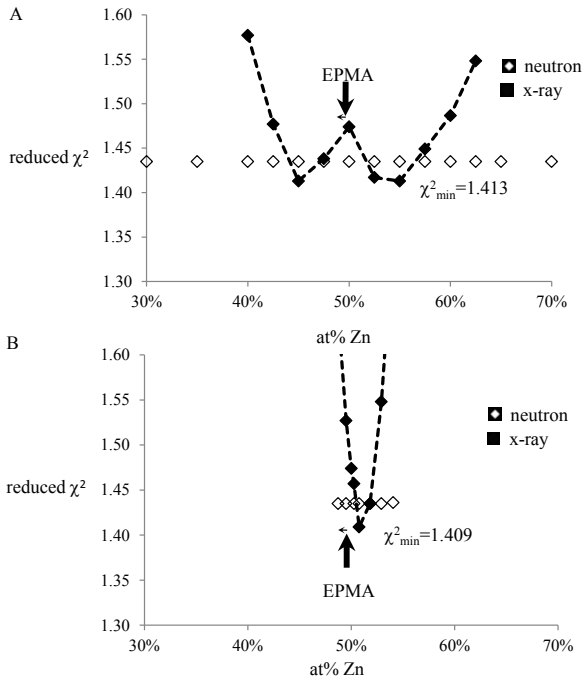

Figure 3.8 A) Variation of the reduced χ^2 parameter with composition for model 1 (anti-site substitution of Pd for Zn and vice versa). B) Variation of the reduced χ^2 parameter with composition for model 2 (vacancy on either the Pd or the Zn-site). The lateral arrow associated with the EPMA value represents the PdZn composition that would be obtained by the correction of the EPMA value to account for the presence of 5 wt% $PdZn_2$.

one would expect it to be manifested by a minimum in the neutron data GOF.

Figure 3.9 shows the variation of the X-ray data refinement GOF parameter with the model 3 disorder parameter (as defined above) for a fixed β_1 PdZn composition of 50 at% Zn, with a minimum located at a disorder parameter value of 0.03. The minimum GOF value of 1.409 is less than or equal to the minimum values that were obtained using models 1 and 2, which means that model 3 accounts for the X-ray diffraction data at least as well as models 1 and 2. Model 3 also satisfies the additional constraint of being close

to the observed composition, indicating that model 3 (i.e. a small amount of Pd-Zn disorder) best describes the state of the sample. The statistics for refinement that was

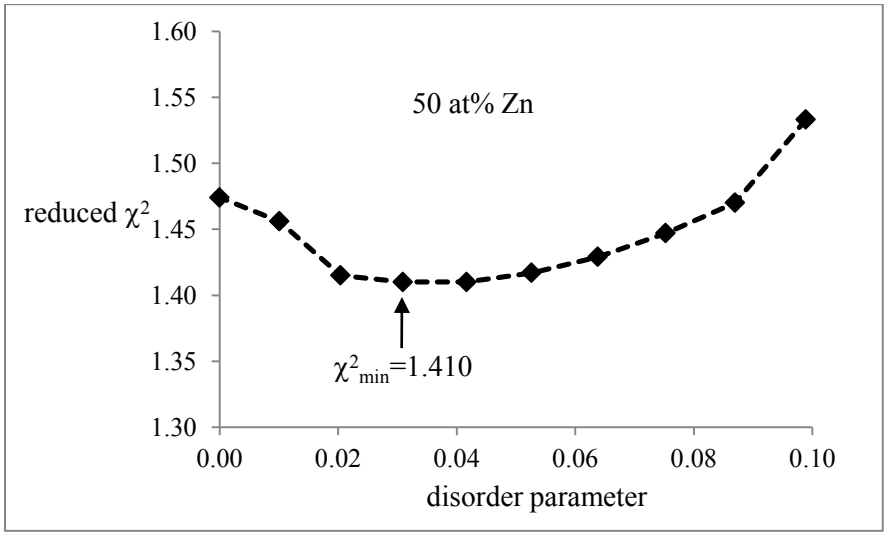

Figure 3.9 Variation of the reduced χ^2 parameter with disorder for model 3 (concomitant exchange of Zn for Pd on the Pd-site and Pd for Zn on the Zn-site, for a fixed 50:50 Pd:Zn atomic composition). The disorder parameter is defined as $\frac{Pd(Zn)+Zn(Pd)}{Pd(Pd)+Zn(Zn)}$, where Pd(Zn) is the fraction of Pd on the nominal Zn-site, Zn(Pd) is the fraction of Zn on the nominal Pd-site, Pd(Pd) is the fraction of Pd on the nominal Pd-site, and Zn(Zn) is the fraction of Zn on the nominal Zn-site.

performed at the GOF minima for the X-ray data refinements are listed in Table 3.3, and refined crystallographic data is summarized in Table 3.4. Because there were no GOF

Table 3.3 Refinement statistics.

XRD	Model 1 (antisite)					Model 2 (vacancy)					Model 3 (disorder)				
Atom % Zn	45.0		55.0			50.8					50.0				
Variables	16		16			16					16				
χ^2 min	1.413		1.413			1.409					1.409				
R_{wp} min	0.1064		0.1066			0.1062					0.1062				
R_{exp} min	0.0533		0.0534			0.0535					0.0535				
Reflections	62		62			62					62				
NPD	Model 1 (antisite)					Model 2 (vacancy)									
Atom % Zn	50.0					50.0									
Variables	128					128									
χ^2 min	1.435					1.435									
Banks	1	2	3	4	Σ	1	2	3	4	Σ					
R_{wp} min	0.0251	0.0237	0.0224	0.0249	0.0241	0.0251	0.0237	0.0224	0.0249	0.0241					
R_{exp} min	0.0175	0.0165	0.0156	0.0174	0.0168	0.0175	0.0165	0.0156	0.0174	0.0168					
D_{wd}	1.219	1.466	1.553	1.313	1.375	1.219	1.466	1.553	1.313	1.375					
Reflections	157	157	122	125		157	157	122	125						

minima in the refinements of the neutron data, neutron statistics and crystallographic data are listed for refinements at the composition of 50 at% Zn.

The DFT optimized lattice parameters for stochiometric and ordered tetragonal (P4/mmm) $Pd_{50}Zn_{50}$ are a=2.920 Å and c=3.412 Å, consistent with previous theoretical work [5] and experiment (a=2.899 Å and c=3.295 Å) [4, 22], as well as our experimental values (4K) (a=2.89458(3) Å and c=3.32724(7) Å). This slight overestimation of lattice parameters is typical for calculations at the GGA-level [19]. We also find that the stochiometric and ordered $L1_0$ phase of PdZn is 0.57 eV/atom more stable than the energy of a mechanical mixture of hcp-Zn and fcc-Pd at the same composition. This large stabilization energy indicates the strong affinity of Pd and Zn to form an alloy. In

Table 3.4 Neutron (NPD) and X-ray (XRD) powder diffraction crystallographic data for PdZn.

Space group	$P\frac{4}{m}mm$		
	Lattice parameters		
	NPD (4 K) (Å)	XRD (R.T.) (Å)[1]	Theory (static)(Å)[2]
a	2.89458(3)	2.89917(7)	2.920
c	3.32724(7)	3.3331(2)	3.412
	Atomic positions		Occupancies (model 3)
Atom site	Wyckoff position	(x,y,z)	Pd Zn
Pd	1a	$(0,0,0)$	0.96 0.04
Zn	1d	$\left(\frac{1}{2},\frac{1}{2},\frac{1}{2}\right)$	0.04 0.96
Thermal Parameters	NPD (4 K) (Å^2)	XRD	
Pd U11	0.0052(1)		
Pd U22	0.0052(1)		
Pd U33	0.0046(2)	(fixed at NPD values)	
Zn U11	0.0049(1)		
Zn U22	0.0049(1)		
Zn U33	0.0062(2)		

[1]SRM640C NIST silicon (a=5.431195 Å) internal standard. [2]The tP2 cell parameters were re-calculated from the tP4 structure using a(tP2)=a(tP4)/sqrt(2)

comparison we find that cubic-B2 PdZn is also strongly stabilized, by 0.56 eV/atom, 10 meV less than the tetragonal $L1_0$ phase. Thus, the L10 structure is expected to be the stable phase as low temperature and the cubic phase may be thermally stabilized at elevated temperatures, consistent with the phase diagram for the Pd-Zn system [24-27] . The calculated energetics for disorder due to Pd ⇔Zn exchange shows that a single exchange is predicted to be energetically disadvantageous by 1.4 eV for the exchange of nearest neighbors (Pd,Zn)-pairs. This energy increases by 0.1 eV as (Pd,Zn) with the largest separation under periodic image convention are exchanged. This high energy associated with disordering leads to the expectation that $Pd_{50}Zn_{50}$ should only possess a

small amount of (Pd,Zn) disorder, corroborating the interpretation of our neutron and X-ray diffraction experiments.

3.3.2.3 *Crystallite size*

Table 3.5 NPD and XRD size parameters and sizes.

	GSAS neutron profile function 4			
	Gaussian size coefficient		Lorentzian size coefficient	
	σ_2^2	*Size (Å)	γ_2	**Size (Å)
NPD 153° bank	11(1)	575(5)	4.4(2)	1023(50)
NPD -153° bank	14(2)	519(5)	4.5(3)	1000(55)
NPD 90° bank	8 (1)	471(3)	4.4 (1)	730(19)
NPD -90° bank	8 (1)	473(4)	4.5 (1)	716(21)
	GSAS x-ray profile function 4 Lorentzian size coefficient			
	L_X	***Size (Å)		
XRD	22.0(3)	401(5)		

$$p = \frac{DIFC \times k}{\sqrt{8(\ln 2)\sigma_2^2}} \qquad ** \; p = \frac{DIFC \times k}{\gamma_2} \qquad *** \; p = \frac{18000 \times k \times \lambda}{\gamma_2}$$

k=0.9 (Sherrer constant) λ=1.540562 (Cu-Kα_1)

Average tetragonal β_1 PdZn crystallite sizes were extracted from the profile parameters that were refined for the X-ray and neutron diffraction data sets, and are listed in Table 3.5. Sizes obtained from refinements using the X-ray and neutron data sets are in reasonable agreement with each other. The observed 40-50 nm sizes indicate that the larger particles seen in Figure 3.3 are polycrystalline. Comparison of the 40-50 nm crystallite sizes, obtained from the diffraction data, to the average particle size of 126 nm, obtained from the BET measurement also suggest that individual particles are composed of several crystallites. As mentioned above, for consistency the cubic phase was included in the refinements using the X-ray diffraction data as well as the neutron diffraction data,

even though its presence in the X-ray data was not readily apparent. Because of the low peak to background ratio for the cubic phase in the X-ray data, the crystallite size profile parameter for the cubic phase was fixed at a value that was consistent with the crystallite size obtained from refinements using the neutron data (9-14 nm).

3.3.2.4 Microstrain

Table 3.6 Neutron diffractometer constants (DIFC) and NPD and XRD anisotropic microstrain parameters

	DIFC	S400	S004	S220	S202	η
NPD 153° bank	5048	5.1(3)	7.5(4)	6.0(5)	-0.6(2)	1.00(2)
NPD -153° bank	5050	3.8(3)	8.3(5)	6.0(5)	-1.2(2)	1.00(3)
NPD 90° bank	3585	2.0(1)	4.1(2)	2.3(2)	-0.1(1)	1.00(2)
NPD -90° bank	3586	1.5(2)	3.5(1)	1.8(2)	-0.2(2)	1.00(2)
XRD		10.4(6)	21(1)	9.0(6)	-6.7(4)	0.66(2)

An anisotropic microstrain model [11] was employed in refinements using both X-ray and neutron data sets. The refined microstrain parameters are listed in Table 3.6, and the microstrain is shown graphically in Figure 3.10. The microstrain obtained from the X-ray data is qualitatively similar to that obtained from the neutron data in that it exhibits a high degree of anisotropy. Quantitative $\frac{\Delta l}{l}$ values along the c-axis are ±0.9% (X-ray) and ±0.6%. (neutron), which are large. Microstrain has been shown to result from chemical effects [33] and/or mechanical effects [34]. In reference [34] it is proposed that nucleation of nanocrystalline α' phase in Ga-stabilized δ plutonium is responsible for microstrain values up to nearly ±0.2% $\frac{\Delta l}{l}$. It is possible that nucleation of

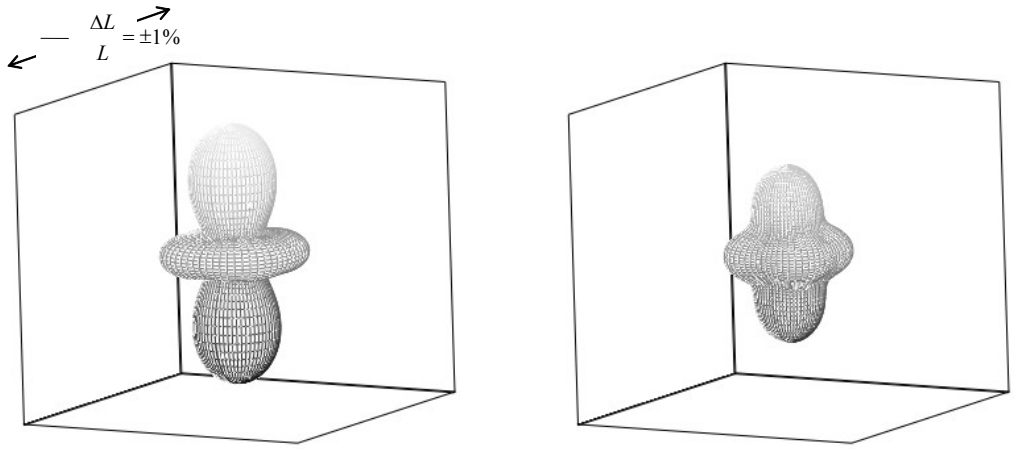

Figure 3.10 Graphical representation of the microstrain, obtained from the XRD data (12a) and the NPD +153° detector bank (12b), which is similar to plots obtained from the NPD -153° and the ±90° detector banks. The edges of the boxes represent ±1% Δl/l.

nanocrystalline cubic $PdZn_2$ (β') is similarly responsible for the observed large anisotropic microstrain that is seen in β_1 PdZn. Chemical effects would be expected to be less important in β_1 PdZn, due to the size similarity of Pd and Zn.

3.4. Conclusions

We have demonstrated that powders of PdZn catalyst of controlled composition can be prepared using an aerosol synthesis method. The high surface area coupled with atomic scale mixing allow for relatively rapid (4 hour) and low temperature (500 °C) formation of powders composed of 95-99 wt% β_1 PdZn, with minor (1-5 wt%) β'' $PdZn_2$ present as a secondary phase. The rapid formation of β_1 PdZn at relatively low

temperature has been shown to result in minimal loss of volatile Zn. Rietveld refinements of neutron and X-ray diffraction data, coupled with electron microprobe analysis, indicate that a small amount of disorder and little or no vacancies are present in β_1 PdZn of composition 50 at% Zn, synthesized under these conditions. This observation is corroborated by our first-principle simulations that show that the energetic allows for a small amount of Pd⇔Zn exchange. We report an experimental X-ray diffraction pattern that is in good agreement with the ICDD calculated reference pattern (PDF number 01-072-2936). The catalytic performance of this powder is currently being investigated and will be described elsewhere [35].

Acknowledgements

Financial support for this work was provided by the US Department of Energy, Grant DE-FG02-05ER15712. Additional support was provided by the US Department of Energy, EPSCoR Grant DE-FG02-08ER46530. We gratefully acknowledge computing resources provided by the New Mexico Computing Applications Center (NMCAC) on Encanto. A portion of the research was performed using EMSL, a national scientific user facility sponsored by the Department of Energy's Office of Biological and Environmental Research and located at Pacific Northwest National Laboratory.

References

1. Iwasa, N., et al., *Dehydrogenation of Methanol to Methyl Formate over Supported Ni, Pd and Pt Catalysts - Anomalous Catalytic Functions of Pdzn and Ptzn Alloys.* Reaction Kinetics and Catalysis Letters, 1995. **55**(2): p. 245-250.
2. Conant, T., et al., *Stability of bimetallic Pd-Zn catalysts for the steam reforming of methanol.* Journal of Catalysis, 2008. **257**(1): p. 64-70.
3. Iwasa, N., et al., *Steam Reforming of Methanol over Pd/Zno - Effect of the Formation of Pdzn Alloys Upon the Reaction.* Applied Catalysis a-General, 1995. **125**(1): p. 145-157.
4. Tsai, A.P., S. Kameoka, and Y. Ishii, *PdZn=Cu: Can an intermetallic compound replace an element?* Journal of the Physical Society of Japan, 2004. **73**(12): p. 3270-3273.
5. Chen, Z.X., et al., *Surface structure and stability of PdZn and PtZn alloys: Density-functional slab model studies.* Physical Review B, 2003. **68**(7).
6. Karim, A., T. Conant, and A. Datye, *The role of PdZn alloy formation and particle size on the selectivity for steam reforming of methanol.* Journal of Catalysis, 2006. **243**(2): p. 420-427.
7. Kodas, T.T. and M.J. Hampden-Smith., *Aerosol processing of materials*. 1999, New York: Wiley-VCH.
8. Nowotny, H. and H. Bittner, **Die Kristallstruktur Von Pdzn.* Monatshefte Fur Chemie, 1950. **81**(5): p. 679-680.
9. Hahn, T., et al., *International Tables for Crystallography*. 3rd, rev. ed. ed. 1992, Dordrecht Boston: Kluwer Academic Publishers.
10. Larson, A.C. and R.B. VonDreele, *General Structure Analysis System (GSAS)*, 2004, Los Alamos National Laboratory Report LAUR 86-748.
11. Stephens, P.W., *Phenomenological model of anisotropic peak broadening in powder diffraction.* Journal of Applied Crystallography, 1999. **32**: p. 281-289.
12. Sears, V.F., *Neutron scattering lengths and cross sections* Neutron News, 1992. **3**(3): p. 29-37.
13. Hohenberg, P. and W. Kohn, *Inhomogeneous Electron Gas.* Physical Review B, 1964. **136**(3B): p. B864-&.
14. Kresse, G. and J. Furthmuller, *Efficiency of ab-initio total energy calculations for metals and semiconductors using a plane-wave basis set.* Computational Materials Science, 1996. **6**(1): p. 15-50.
15. Kresse, G. and J. Hafner, *Ab-Initio Molecular-Dynamics for Open-Shell Transition-Metals.* Physical Review B, 1993. **48**(17): p. 13115-13118.
16. Kresse, G. and J. Hafner, *Norm-Conserving and Ultrasoft Pseudopotentials for First-Row and Transition-Elements.* Journal of Physics-Condensed Matter, 1994. **6**(40): p. 8245-8257.

17. Perdew, J.P., K. Burke, and M. Ernzerhof, *Generalized gradient approximation made simple.* Physical Review Letters, 1996. **77**(18): p. 3865-3868.
18. Blochl, P.E., *Projector Augmented-Wave Method.* Physical Review B, 1994. **50**(24): p. 17953-17979.
19. Kresse, G. and D. Joubert, *From ultrasoft pseudopotentials to the projector augmented-wave method.* Physical Review B, 1999. **59**(3): p. 1758-1775.
20. Methfessel, M. and A.T. Paxton, *High-Precision Sampling for Brillouin-Zone Integration in Metals.* Physical Review B, 1989. **40**(6): p. 3616-3621.
21. Monkhorst, H.J. and J.D. Pack, *Special Points for Brillouin-Zone Integrations.* Physical Review B, 1976. **13**(12): p. 5188-5192.
22. Pearson, W.B., *Handbook of Lattice Spacings and Structures of Metals*. 1st ed. International series of monographs on metal physics and physical metallurgy ; v. 4, 8 Vol. 2. 1967, New York: Pergamon Press. 1044.
23. Ertl, G., H. Knözinger, and J. Weitkamp, *Handbook of heterogeneous catalysis*. 1997, VCH: Weinheim.
24. P. Villars, e.-i.-c., *PdZn phase diagram*, s.e. Okamoto and K. Cenzual, Editor 2006, ASM International.
25. Massalski, T.B., *Binary Alloy Phase Diagrams*. Second ed, ed. T.B. Massalski. Vol. 3. 1990, Materials Park, Ohio: Materials Information Soc.
26. Hansen, M., *Constitution of Binary Alloys*. Second ed. Metallurgy and Metallurgical Engineering Series, ed. R.F. Mehl and M.B. Bever. 1958, New York, Toronto, London: McGraw-Hill.
27. Okamoto, H., *Pd-Zn (Palladium-Zinc)*. II ed. Binary Alloy Phase Diagrams, ed. T.B. Massalski. Vol. 3. 1990: ASM International. 3068-3070.
28. Nowotny, H., E. Bauer, and A. Stempfl, **Ein Beitrag Zum System Palladium-Zink.* Monatshefte Fur Chemie, 1951. **82**(6): p. 1086-1093.
29. Stadelmaier, H.H. and W.K. Hardy, *Ternare Kohlenstofflegierungen Von Palladium Und Platin Mit Magnesium, Aluminium, Zink, Gallium, Germanium, Kadmium, Indium, Zinn, Quecksilber, Thallium Und Blei.* Zeitschrift Fur Metallkunde, 1961. **52**(6): p. 391-396.
30. Alasafi, K.M., T. Chattopadhyay, and K. Schubert, *Pdznn Mixture.* Journal of the Less-Common Metals, 1978. **59**(1): p. P41-P50.
31. Neumann, J.P., H. Ipser, and Y.A. Chang, *Structural Stability of B2 and L1o Phases in System Pd-Zn.* Journal of the Less-Common Metals, 1978. **57**(1): p. P29-P37.
32. Kou, S. and Y.A. Chang, *Thermodynamics of Ordered Beta1-Pdzn Alloys.* Acta Metallurgica, 1975. **23**(10): p. 1185-1190.
33. Peterson, E.J., et al., *MICRO-STRAIN IN Y0.5R0.5Ba2Cu3O7-x (R=Yb, Tm, Er, Ho, Dy, Gd, Eu, Sm, AND Nd).* Advances in X-ray Analysis, 2002. **45**: p. 238-244.
34. Lawson, A.C., et al., *Lattice constants and anisotropic microstrain at low temperature in Pu-242-Ga alloys.* Philosophical Magazine, 2005. **85**(18): p. 2007-2022.

35. Halevi, B., et al., *Aerosol-derived bimetallic alloy powders- bridging the gap.* Journal of Chem Physics C.

Chapter 4 Rietveld analysis of Pt-Sn and Pt-Ru bimetallic catalysts for ethanol oxidation

Abstract

Ethanol oxidation catalysts composed of Pt, Pt-Sn, and Pt_Ru having controlled bimodal particle size distributions were synthesized using a sacrificial templating technique. Rietveld analysis of X-ray diffraction data was used to quantify crystallite size, lattice parameters, and metal vacancies in these samples. Stable refinements were achieved by considering the Bragg diffraction peaks to be composed of phases with similar lattice parameters but different crystallite size. In the case of the Pt-Sn sample, the Pt_3Sn (100) and (110) peaks were found to be more intense than expected. This was accounted for by the introduction of vacancies on the Sn-site, The presence of Sn vacancies was corroborated independently by a Vegard's law type consideration of the effect of metal vacancies on lattice parameter.

4.1. Introduction

Direct ethanol fuel cells (DEFC) are of interest due to the ready availability of ethanol and the established infrastructure for the production and distribution of ethanol. Ethanol use in fuel cells is considered to be preferable to the use of methanol because of the toxicity of methanol.

The reactions occurring in a DEFC are:

$C_2H_5OH + 3H_2O \rightarrow 12H^+ + 12e^- + 2CO_2$ ethanol oxidation (anode) **Equation 4.1**

$12H^+12e^- \rightarrow 6H_2O$ oxygen reduction (cathode) **Equation 4.2**

Bimetallic Pt-Sn and Pt-Ru intermetallics are potential ethanol oxidation catalysts. In this work, these materials were synthesized using a biporous silica template [1]. The goal of this work was to produce a hierarchy of catalyst features on different size scales. Rietveld analysis of X-ray diffraction data obtained from these samples was used to characterize catalyst particle size and structural parameters including lattice parameters and metal vacancies.

4.2. Experimental

Silica template material was synthesized using water phase, containing tetraethylorthosilicate (TEOS, Purum>98%), cetyltrimethylammonium bromide (CTAB) and 1N hydrochloric acid and oil phase, containing polyetherpolysiloxane/dimethicone co-polyol surfactant (ABIL EM 90, Degussa) and hexadecane. Water and oil phase were combined, emulsified, heated to 80C under a reduced pressure of 70 mTorr for 3 hours. After removal of the water phase, material was centrifuged to separate oil phase and particles, which than are calcined in air at 500°C for 5 hours. Silica particles (200 mg) were dry impregnated with solution of sucrose (437.5 mg) in 2M H_2SO_4 (933 µl) and acetone (1820 µl). After silica is impregnated with first half of carbon precursor solution, the resulting material was dried in the oven at 100°C for 15 min and then at 150°C for another 15 min. Then this material was impregnated with the second of the carbon

precursor, dried at 100°C for 15 min and then at 150C for 1 hour. After material was cooled down, it was dry impregnated with metal precursor solution. Metal precursor solutions were prepared by dissolving $H_2PtCl_6 \cdot 6H_2O$ or $H_2PtCl_6 \cdot 6H_2O$ and $SnCl_2 \cdot 2H_2O$ or $H_2PtCl_6 \cdot 6H_2O$ and $RuCl_3$ in 2M H_2SO_4 in quantities necessary to make nominal 10wt% and 45wt% metal loading samples of PtSn with 80:20 Pt:Sn ratios(designated 10PtSn and 45PtSn), PtRu with 50:50 Pt:Ru ratios (designated 10PtRu and 45PtRu) and 10wt% Pt. After all metal precursor solution was added to the silica particles, they were dried in the oven at 70 °C and then pyrolyzed in flowing N_2 for 4 h at 800 °C, with the ramp rate 3 °C per min. After pyrolysis, silica was etched in 6 M KOH for 4 days. The material was then filtered, washed five times with DI water, and dried in the oven at 70 °C.

X-ray diffraction data was collected using a Scintag PADV diffractometer equipped with a graphite monochromator and scintillation detector and using Cu Kα radiation. Rietveld analysis was performed using GSAS [2]

4.3. Results and discussion

Crystallite size, weight fractions and lattice parameters obtained from the Rietveld analysis as well as lattice parameter reference values, obtained from the literature, are listed in Table 4.1. A composite of all XRD data is shown in Figure 4.1 Evident for the 10wt% samples are only Pt and Pt-solid solution peaks. The 45PtSn also displays Pt_3Sn peaks and the 45PtRu sample contains Ru(Pt) and a trace of RuO_2. The Pt(111) and Pt(200) regions of the XRD data obtained from the 10Pt sample are shown in Figure 4.2.

The peaks present in this data set exhibit an unusual shape, with broad bases combined with sharp peak tops. While attempts to fit these peaks using a single peak profile function resulted in poor fits, an excellent fit to the data was obtained through the use of a combination of a sharp peak profile function to fit the peak tops and a broad peak profile function to fit the peak tails. This result is shown in Figure 4.2, and indicates that there is a bimodal distribution of crystallites sizes in this sample. The lattice parameters obtained for this sample are in agreement with literature values (Table 4.1).

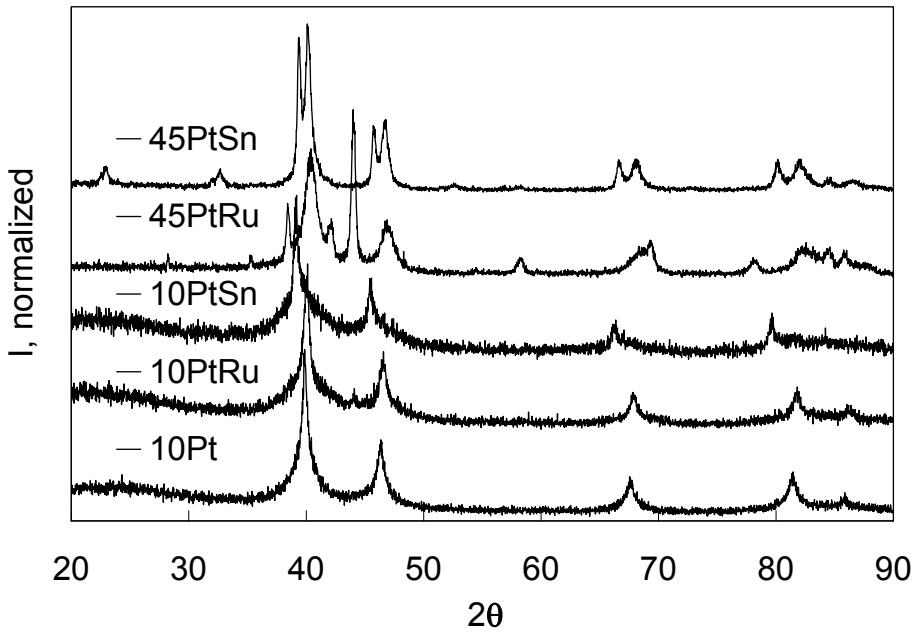

Figure 4.1 Normalized X-ray diffraction data for the 10PtSn, 10PtRu, 45PtSn, and 45PtRu samples.

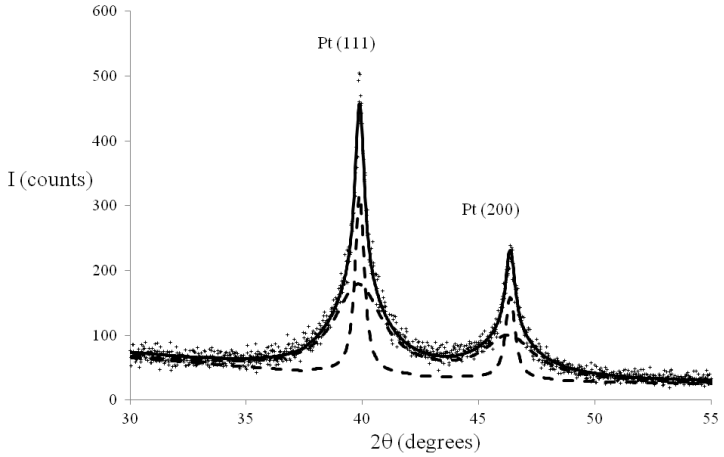

Figure 4.2 X-ray diffraction data narrowed to main Pt peaks for the Pt/Carbon sample. The (+) symbols represent observed data, dashed lines represent the large (narrow peak) and small (broad peak) crystallite contributions to the overall fit (solid line).

Similar multimodal-sized crystallite distributions were obtained for the 10PtSn and 10PtRu samples. However, the lattice parameters obtained from these samples differed significantly from the pure Pt values, with the 10PtSn sample having lattice parameters 0.4% (small crystallites) to 1.8% (large crystallites) larger than the literature value for Pt, and the 10PtRu sample having lattice parameters 0.40% (large crystallites) to 0.43% (small crystallites) smaller than the literature value for pure Pt. However, since Sn and Ru are soluble to high levels in Pt the observed change in Pt lattice parameter is expected and consistent with Sn and Ru dissolved in Pt and their relative atomic sizes [3]; addition of Sn (1.45 Å) to Pt (1.35 Å) in solid solution (Pt(Sn)) would be expected to

Table 4.1 XRD and Rietveld refinement analysis summary.

Sample	Phase	Crystallite size (nm)	Wt. Fraction	Lattice parameter(s) (Å) [Vegard law composition]	
Pt	Large Pt	21(1)	0.065(3)	3.9223(3)	
	Small Pt	3.4(1)	0.176(3)	3.927(1)	
	Graphite		0.759(6)		
10PtSn	Large Pt(Sn)	26(1)	0.080(3)	3.9947(4)	[28% Sn]
	Small Pt(Sn)	2.3(1)	0.435(3)	3.940(2)	[5% Sn]
	Graphite		0.48(2)		
10PtRu	Large Pt(Ru)	19.7(5)	0.082(1)	3.9074(4)	[10.5% Ru]
	Small Pt(Ru)	2.6(1)	0.215(2)	3.906(2)	[11.5% Ru]
	Graphite		0.702(7)		
45PtSn	Pt(Sn)	20(1)	0.076(3)	3.9697(5)	[17% Sn]
	Large Pt_3Sn	48(1)	0.170(4)	3.9797(2)	
	Medium Pt_3Sn	23(1)	0.426(5)	3.9052(3)	
	Small Pt_3Sn	9.0(1)	0.328(3)	3.8984(4)	
45PtRu	Pt(Ru)	26(1)	0.387(2)	3.8811(4)	[28% Ru]
				a	c
	Ru(Pt)	5.9(1)	0.596(3)	2.7136(3)	4.3055(6)
	RuO2	74(16)	0.017(2)	4.493(1)	3.104(2)
Lattice parameter reference values			Pt [4]	3.9231	
			Pt_3Sn [5]	4.004	
			Pt_3Sn [6]	4.0005	
			Pt_3Sn [7]	4.018	
				a	c
			Ru [4]	2.70389	4.28168
			RuO_2 [8]	4.4919	3.1066

result in lattice parameter expansion, while similar addition of Ru (1.30 Å) to Pt alloy component concentrations (Pt(Ru)) should result in lattice parameter contraction. The Pt(Sn) and Pt(Ru) lattice parameters can be quantitatively related to composition via Vegard's law [9] which suggests an empirical linear relation between crystal lattice parameters of an alloy and the composition:

$$a_{Pt(Sn)} = 3.928 + 0.0024\, F_{Sn} \qquad \textbf{Equation 4.3}$$

$$a_{Pt(Ru)} = 3.9231 + 0.001489\, F_{Ru} \text{ [10]} \qquad \textbf{Equation 4.4}$$

where $a_{Pt(Sn)}$ and $a_{Pt(Ru)}$ are the measured lattice parameters and F_{Sn} and F_{Ru} are the fractions of Sn and Ru, respectively. Compositions that were obtained in this manner are listed in Table 4.1.

From the phase diagrams the equilibrium solid solution limit of Sn in Pt is only a few percent[5]; however, the observed Pt(Sn) compositions for the catalysts in this study range from near the Pt(Sn) solubility limit up to somewhat above the Pt_3Sn line compound composition[5]. The compositions that are observed for the two Pt(Sn) populations present in the 10PtSn sample are close to what would be expected for an equilibrium PtSn composition falling in the 2-phase region between Pt(Sn) and Pt_3Sn. However, the diagnostic Pt_3Sn (100) and (110) diffraction peaks were not observed for this sample, indicating that the phase having approximately Pt_3Sn composition is completely disordered, and possibly meta-stable.

In the case of the Pt-Ru system the solubility limits of Ru in Pt[11] span 0-62 at%Ru so that both Pt:Ru formulations should yield phase pure Pt(Ru). The 10PtRu

material consists of Pt(Ru) of near-nominal 10% Ru composition, with a bimodal distribution of average diameter crystallites as indicated in Table 4.1. However, the 45PtRu sample contains both Pt(Ru) concentrated in larger particles and Ru(Pt) concentrated in smaller particles, suggesting that higher loading of the Templated Backbone lead to less homogeneous composition of materials. The improved compositional homogeneity of the 10wt% loading materials may be due to reduction of the precursors by the Templated Carbon or reduced wicking for high loading samples due to increased loading.

The 45PtSn sample nominal composition should lead to a material composed of a mixture of Pt_3Sn and Pt(Sn). Instead, the sample was composed of Pt and Pt_3Sn suggesting that the Pt(Sn) phase is meta-stable under the synthesis condition used. The Pt_3Sn structure is similar to the F.C.C. Pt structure, but with the ordered addition of one Sn for one Pt. This ordering reduces the Pt_3Sn symmetry to primitive cubic, allowing the presence of the observed Pt_3Sn (100) and (110) peaks, which would be absent in the case of random substitution of Sn for Pt. Splitting of the Pt_3Sn (100) and (110) peaks, as seen in Figure 4.3, indicated the presence of at least 2 Pt_3Sn populations having slightly different lattice parameters. As with the Pt, 10PtSn, and 10PtRu samples, the Bragg diffraction peak shapes were indicative of multi-modal crystallite size distributions. Because of the significant peak overlap of the possible combinations of phases, six multi-phase/size models were tested and evaluated with respect to their reduced χ^2 goodness of fit parameters, listed in Table 4.2. The model having the best fit was that composed of three distinct Pt_3Sn size populations (large, medium and small), with a mono-modal

Pt(Sn) size distribution. The overall Rietveld fit to the data with the contributions of each population is shown in Figure 4.4.

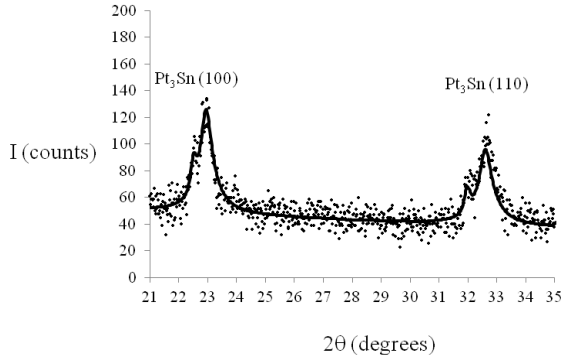

Figure 4.3 Observed data (+) and fit (solid line, model 6) for the 45PtSn sample, showing the splitting of the Pt_3Sn (100) and (110) peaks.

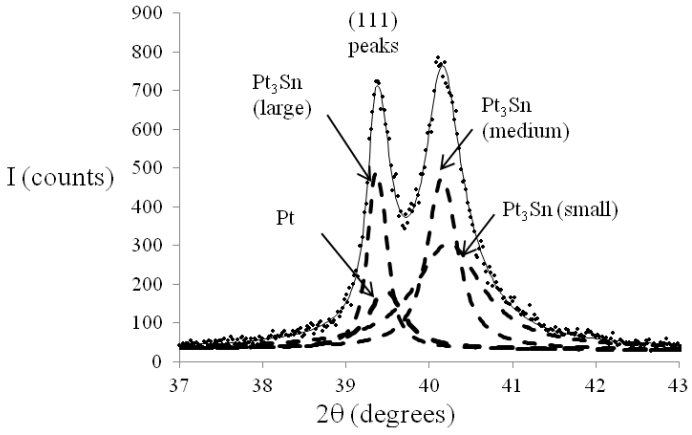

Figure 4.4 Observed data (+) and fit (solid line, model 6) for the 45PtSn sample, showing the best fit contributions of each population (dashed lines).

Table 4.2 Rietveld model goodness of fit summary for 45PtSn and 45PtRu.

Model		Reduced χ^2	# Variables
1	2 phase-2 Pt_3Sn	1.213	20
2	3 phase-Pt + 2 Pt_3Sn	1.194	24
3	3 phase-3 Pt_3Sn	1.147	24
4	4 phase-2Pt + 2 Pt_3Sn	1.126	28
5	4 phase-4 Pt_3Sn	1.111	29
6	4 phase-Pt + 3 Pt_3Sn	1.105 (best model)	29
7	3 phase-Pt + Ru + RuO_2	1.126 (best model)	15
8	4 phase-2Pt+ Ru+ RuO_2	1.129	24
9	4 phase-Pt + 2Ru +RuO_2	1.129	24

In the course of the refinements it was found that the observed intensities of the Pt_3Sn (100) and (110) peaks were somewhat larger than predicted by the standard Pt_3Sn model. This results from greater than expected X-ray scattering contrast between the Pt and Sn-sites, which in turn could be explained by either 1) greater than expected X-ray scattering on the Pt-site or 2) less than expected X-ray scattering on the Sn-site. The first possibility is unlikely, as it would require the presence of a significant amount of a contaminant having an atomic number greater than that of Pt occupying the Pt-site. Conversely, Sn-site X-ray scattering could be reduced by the presence of vacancies on the Sn-site. Vacancies on the Sn-site were therefore introduced into the Rietveldt refinement model, resulting in much-improved fits to the Pt_3Sn (100) and (110) peaks. An independent verification of the presence of vacancies in the Pt_3Sn phases is provided by a consideration of the observed Pt_3Sn lattice parameters as compared to values obtained from the literature (Table 4.1). The observed Pt_3Sn lattice parameters are

significantly smaller that the literature values, indicating the presence of Pt_3Sn vacancies. A simple quantitative treatment of vacancies in metals [12] provides the relationship

$$\Delta a = \left(2^{-\frac{1}{3}} - 1\right) a_m \Delta c_v \qquad \textbf{Equation 4.5}$$

where Δa is the lattice parameter decrease, a_m is the lattice parameter of the vacancy-free phase, and Δc_v is the fraction of vacancies. A comparison of vacancy fractions obtained from peak intensity (Rietveld) analysis vs. lattice parameter measurements is shown in Figure 4.5.

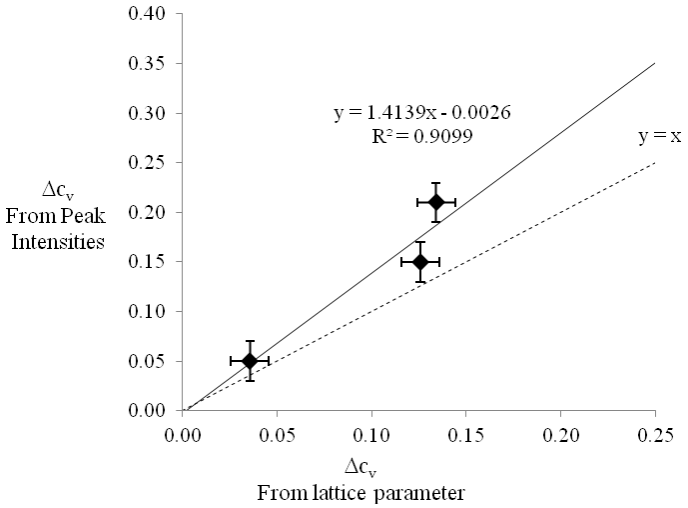

Figure 4.5 Pt_3Sn vacancy concentrations as determined independently by diffraction peak intensity and lattice parameter. Points with perfect agreement between the two methods would plot on the dashed line.

4.4. Conclusions

Rietveld refinement of XRD data determines that the catalysts are composed of metallic particles with bimodal size distribution corresponding to the pore sizes of the HSS template used. Further, the compositions of the 2 size modalities differ for PtRu and PtSn. For PtRu materials there is an observed loss in Ru, possibly due to volatilization during the synthesis. For the PtSn materials the lack of Pt_3Sn phase particles with diameters less than approximately 9 nm suggests that Pt_3Sn is unstable for such small sizes, or that Sn volatilization during synthesis leads to surface Pt enrichment so that Pt_3Sn does not form for small particles. Atomic vacancies in Pt_3Sn were quantified independently using Rietveld analysis and a Vegard's Law approach, with reasonable agreement between the two methods.

Acknowledgements

We gratefully acknowledge support from DOE 629 EPSCoR NM Implementation Award.

References

1. Pylypenko, S., et al., *Templated Platinum/Carbon Oxygen Reduction Fuel Cell Electrocatalysts.* Journal of Physical Chemistry C. **114**(9): p. 4200-4207.
2. Larson, A.C. and R.B. VonDreele, *General Structure Analysis System (GSAS)*, 2004, Los Alamos National Laboratory Report LAUR 86-748.
3. Slater, J.C., *Atomic Radii in Crystals.* Journal of Chemical Physics, 1964. **41**(10): p. 3199.
4. Wyckoff, R., *Crystal Structures*. Second ed. 1963, New York, New York: Interscience Publishers.
5. Durussel, P., R. Massara, and P. Feschotte, *The Binary-System Pt-Sn.* Journal of Alloys and Compounds, 1994. **215**(1-2): p. 175-179.
6. Charlton, J.S., Cordeyha.M, and I.R. Harris, *A Study of Sm-119 Mossbauer Isomer Shifts in Some Platinum-Tin and Gold-Tin Alloys.* Journal of the Less-Common Metals, 1970. **20**(2): p. 105-&.
7. Shelton, K.L., P.A. Merewether, and B.J. Skinner, *Phases and Phase-Relations in the System Pd-Pt-Sn.* Canadian Mineralogist, 1981. **19**(4): p. 599-605.
8. Baur, W.H. and A.A. Khan, *Rutile-Type Compounds .4. Sio2, Geo2 and a Comparison with Other Rutile-Type Structures.* Acta Crystallographica Section B-Structural Crystallography and Crystal Chemistry, 1971. **B 27**(NOV15): p. 2133-&.
9. Vegard, L., *The constitution of the mixed crystals and the filling of space of the atoms.* Zeitschrift Fur Physik, 1921. **5**: p. 17-26.
10. Le Page, Y., C. Bock, and J.R. Rodgers, *Small step graphs of cell data versus composition for ccp solid-solution binary alloys: Application to the (Pt,Ir), (Pt,Re) and (Pt,Ru) systems.* Journal of Alloys and Compounds, 2006. **422**(1-2): p. 164-172.
11. Massalski, T.B., *Binary Alloy Phase Diagrams*. Second ed, ed. T.B. Massalski. Vol. 3. 1990, Materials Park, Ohio: Materials Information Soc.
12. Mittemeijer, E.J., *X-ray Diffraction Analysis of the Microstructure of Precipitating Al-Based Alloys*, in *Analytical Characterization of Aluminum, Steel, and Superalloys*, D.S. MacKenzie and G.E. Totten, Editors. 2006, CRC Press Taylor & Francis Group, LLC: Boca Raton, Fl. p. 344-346.

Chapter 5 Low Temperature CO Oxidation Catalyzed by Regenerable Atomically Dispersed Palladium on Alumina

Abstract

Catalysis by single isolated atoms of precious metals has attracted much recent interest since it promises the ultimate economy in atom efficiency. Previous reports have been confined to reducible oxide supports such as FeO_x, TiO_2 or CeO_2. Here we show that isolated Pd atoms can be stabilized on industrially relevant γ-alumina supports. At low Pd loadings (≤0.5 wt%) these catalysts contain exclusively atomically dispersed Pd species. The addition of lanthanum-oxide to the alumina, long known for its ability to improve alumina stability, is found to also help in the stabilization of isolated Pd atoms. Aberration-corrected scanning transmission electron microscopy (AC-STEM) confirms the presence of intermingled Pd and La on the γ-alumina surface. Operando X-ray absorption spectroscopy, performed on Pd/La-alumina and Pd/γ-alumina (0.5 wt% Pd) demonstrates the presence of catalytically active atomically dispersed ionic Pd in the Pd/La-doped γ-alumina system. CO oxidation reactivity measurements show onset of catalytic activity at 40 ˚C, indicating that the ionic Pd species are not poisoned by CO. The reaction order in CO and O_2 is positive, suggesting a reaction mechanism that is different from that on metallic Pd. The catalyst activity is lost if the Pd species are reduced to their metallic form, but the activity can be regenerated by oxidation at 700 ˚C in air. The high-temperature stability and regenerability of these ionic Pd species on

commercial alumina supports makes this catalyst system of potential interest for low-temperature exhaust treatment catalysts.

5.1. Introduction

Automotive catalytic converters have played a central role in improving air quality in urban environments. Precious metals such as Pt, Rh and Pd, in the form of nanoparticles, constitute the catalytically active phase that helps to mitigate pollutants such as hydrocarbons, nitrogen oxides and CO, thus helping reduce smog and ozone. Exhaust treatment catalysts are very effective when heated above 200 °C, but provide limited reactivity at lower temperatures because the platinum group metals are poisoned by CO at lower temperatures. As a consequence, most of the pollutants from a modern automobile are emitted during the first 30 seconds of starting a car, when the catalyst is still being warmed up. As advanced combustion engines are developed, we expect that the temperature of automotive exhaust will drop and catalysts will need to function at lower temperatures. The US Department of Energy road map has set a goal for light-off below 150 °C [1]. Therefore, there is an urgent need to develop catalysts that are not poisoned by CO and become active at low temperatures. Herein we demonstrate that atomically dispersed Pd^{2+} ions, bound to surface oxygen atoms on alumina, resist CO poisoning and are able to achieve high activity for CO oxidation at low temperatures.

A recent report by Flytzani-Stephanopoulos[2] reviews the evidence that atomically dispersed, ionic Au species, are present on Au/TiO_2 and are responsible for increased catalytic reactivity. Similar results on single atom catalysts were reported by

for Pt on the reducible oxide FeOx[3]. There is increasing interest in catalysis by single atoms which promise high atom efficiency and improved low temperature reactivity as well as selectivity. For example, Ir/FeOx[4] and $Pd/CeO_{2[5]}$ also exhibit improved low temperature reactivity which may be related to the presence of atomically dispersed species. However, in each of these catalysts, the support was a reducible metal oxide which can provide labile oxygen species that can participate in the reaction. In our work we have focused on γ-alumina as a support, since it is the most widely commercialized support for heterogeneous catalysts due to its high specific surface area (100-200 m^2/g) and thermal stability.

The structure of γ-alumina can be thought of as an fcc (face centered cubic) packing of oxygen atoms, with Al^{3+} cations filling octahedral and tetrahedral interstitial sites among the oxygen atoms. The γ-alumina structure has been considered as a defective spinel structure [6], in which the Mg^{2+} atoms in spinel ($MgAl_2O_4$) have been removed, and the Al_2O_3 stoichiometry is accommodated by cation vacancies. More recently, a non-spinel structure, energetically more stable and more reflective of experimental data has been proposed [7, 8]. This structural model also has the advantage of being practical for density functional theory (DFT) calculations, capturing the essence of the γ-alumina structure in a smaller unit cell than the spinel structure, and is the model used in our work. For consistency with the literature, however, Miller indices used in this work refer to the spinel unit cell. Both the defective spinel and the non-spinel models proposed for the γ-alumina structure contain Al^{3+} vacancy-defect sites, manifested as 4-fold hollow sites on the γ-alumina (100) surface. A second feature, common to all

models, are penta-coordinated Al^{3+} surface sites, also known as coordinatively unsaturated Al^{3+} sites (CUS) [9, 10], formed by the truncation of AlO_6 octahedra at the γ-alumina (100) surface.

In practice, high working temperatures inevitably lead to the transformation of the transitional γ-alumina to thermodynamically stable corundum, with concomitant loss of surface area. However, the addition of a few mol % La_2O_3 to γ-alumina has been found to result in improved surface area stability at high temperatures [11-13]. Using X-ray photoelectron spectroscopy (XPS), Haack, et al. [14] determined that, for La/Al ratios less than 0.15, La is likely present as a dispersed, low-coordinated La^{3+} phase, rather than as La_2O_3. Lanthanum oxide has been routinely added to γ-alumina in automobile catalysts since these discoveries, but the location of the La^{3+} was somewhat of a mystery until the advent of aberration-corrected electron microscopes, in conjunction with DFT calculations. It was shown by Wang, et al. [15] that atomically dispersed La^{3+} is present on the γ-alumina surface, settling into 4-fold hollow, Al^{3+} vacancy sites. These surface La^{3+} ions appear to pin the oxygen substructure, hindering the reconstructive transformation from the fcc (abcabc…) arrangement to the hcp (hexagonally close packed) (ababab…) packing of the corundum structure.

In the case of palladium, XPS observations by Otto et al. [16] demonstrated the existence of two types of palladium oxide present on γ-alumina. One oxide was characterized by relatively large particles with a Pd 3d binding energy characteristic of PdO, and which could be readily transformed to Pd metal at room temperature in hydrogen. The second oxide, predominant at low palladium loadings (≤0.5 wt.%), was

characterized by a binding energy shift of 1.6 eV, higher than that for PdO, and was found to be resistant to reduction to Pd metal at room temperature in hydrogen. It was proposed by these authors that this second chemical state of palladium could correspond to highly dispersed Pd^{2+} due to a strong metal-support interaction. More recently, palladium has been observed to be stabilized as an atomically dispersed, as well as catalytically active species, on mesoporous alumina [17]. At low Pd loadings (<0.1 wt%), the Pd present on this support was observed to be predominantly atomically dispersed as Pd^{2+}. It was also found that these species were catalytically active for the selective aerobic oxidation of allylic alcohols, with a turnover frequency one order of magnitude higher than that observed for Pd-metal particles. There are, however, no reports of the stabilization of atomically dispersed Pd at elevated temperatures, such as those encountered in automotive catalysts.

This work has focused on the synergistic effects of La and Pd, supported on γ-alumina. We compare the CO oxidation reactivity of atomically dispersed Pd, loaded onto pure γ-alumina and La-doped γ-alumina supports. Aberration-corrected electron microscopy was used to characterize dispersion of La and Pd species on the surface of the γ-alumina support. To correlate catalytic behavior with the chemical state of Pd, simultaneous CO oxidation and Pd K-edge X-ray absorption spectroscopy (XAS) measurements were also performed. On the basis of these experiments, coupled with DFT calculations, a structural model for atomically dispersed Pd on La-alumina is proposed, as well as a possible CO oxidation mechanism.

5.2. Results

5.2.1 *Imaging of atomically dispersed Pd*

In previous work [18], we reported the role of lanthana on the particle size of Pd and the reactivity for CO oxidation in a 2.5 wt% Pd/Al_2O_3 catalyst. At this high metal loading, most of the Pd is present in the form of metallic nanoparticles. However, we noticed that Pd particles on the La-alumina support were smaller, were more readily oxidized, and desorbed CO at low temperatures, mitigating the poisoning effect. As a result, there was a modest improvement in low temperature performance of the Pd/La-alumina catalysts, compared to the Pd/alumina. Additionally, high-angle annular dark-field transmission electron microscopy (HAADF TEM) coupled with energy-dispersive X-ray spectroscopy (EDS) provided evidence for the presence of atomically dispersed Pd and La in this catalyst. Figure A.1 in Appendix A shows an EDS spectrum of a region of this 2.5 wt% Pd catalyst that is devoid of Pd-metal particles. Both Pd and La characteristic X-ray peaks are seen in the spectrum, indicating that these elements are present on the γ-alumina support at concentrations high enough to be detected by EDS but otherwise not visible in the HAADF images. The average concentration of the atomically dispersed Pd was estimated to be about 0.5 wt% and this loading is similar to that seen previously in automotive catalysts for the 'oxidized' form of Pd which was thought to interact strongly with the alumina support [16].

An image of the 2.5 wt%Pd/La-alumina catalyst, obtained using an aberration-corrected (AC) microscope is shown in Figure 5.1A. This image confirms that isolated single atoms (the bright dots) are present on the alumina support in close proximity to the

Pd metal nanoparticle. The contrast of these isolated single atoms results from electron scattering from the nucleus, with intensity related approximately to the square of the atomic number (Z^2). The dependence of contrast on atomic number has previously been employed to distinguish the identity of individual atoms in a thin sample of boron nitride,[19] but application of this approach to identify the single atoms in a heterogeneous catalyst is more difficult due to the strong and varying background from the alumina support. We developed a method of image analysis that involves fitting the overlapping atom intensities to 2-dimensional Gaussian functions (Figure 5.1B-D) allowing for the extraction of single-atom intensities and facile background subtraction. The histogram of intensities shows a bimodal distribution for Pd/La-alumina (Figure 5.1F) while a single peak is seen for the La-alumina sample (no Pd) (Figure 5.1E). The ratio of image intensities (ie. peak positions on the x-axis) of the two peaks in the bimodal distribution agrees with the ratio of the square of the atomic numbers for La and Pd, indicating that the atomically dispersed species, seen in Figure 5.1A, are composed of Pd that is comingled with La on the alumina support.

Because the concentration of the atomically dispersed species in the 2.5 wt% Pd catalyst was estimated to be 0.5 wt%, we prepared a series of catalysts with this lower loading. The rest of the manuscript describes the characteristics of these 0.5 wt% Pd/alumina catalysts. An AC-STEM image of this catalyst is shown in Figure 5.S2. Bright dots corresponding to atoms of Pd and La are seen. The number of these bright dots was counted and when normalized to the surface area, the concentration was found to be consistent with the loading of this sample, as explained in Appendix A. Hence, we

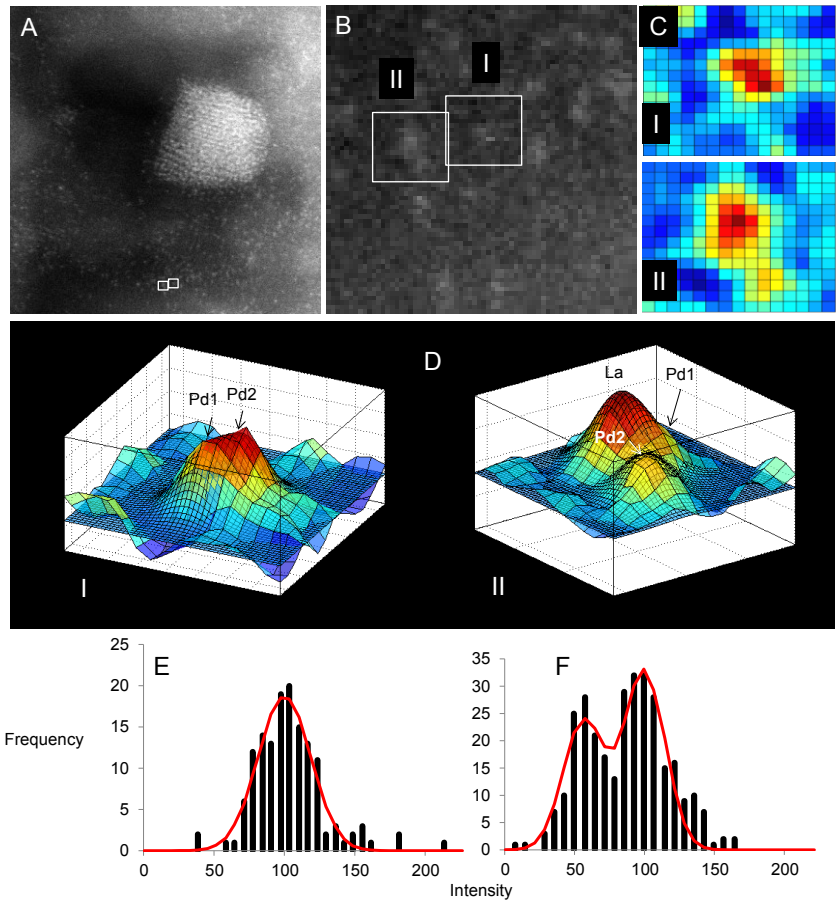

Figure 5.1 Intensity analysis of ACEM images obtained from a La-stabilized γ-alumina support sample with a 2.5 wt.% Pd-loading. **(A)** A typical region of the sample, with a Pd-metal particle surrounded by atomically dispersed Pd and La. **(B)** An enlarged region from **(A)**, showing two regions containing atomically dispersed species. **(C)** Colorized intensity maps from regions I and II. **(D)** 2-D Gaussian-function fits (fine-mesh) to the intensity maps in **(C)**. **(E)** and **(F)** Normalized intensity distributions, obtained from 2-D Gaussian-function fits of images obtained from La-alumina **(E)** and Pd-La-alumina **(F)** showing well-resolved peaks corresponding to Pd and La electron backscatter intensity in the case of the Pd-La-alumina sample. The red lines represent Gaussian-function least-squares fits to the intensity distributions.

conclude that when prepared carefully and calcined in air, these catalysts do not show any particulate Pd phase as seen by XRD, TEM or EXAFS. When studying the reactivity of atomically dispersed Pd species, it is important to prepare samples devoid of metallic Pd particles so that the reactivity can be ascribed to only one form of Pd. In previous work with Au catalysts, the authors had to leach out the metallic component before performing catalytic tests [2, 20]. Even if the initial catalyst is in the form of atomically dispersed species, the catalyst can evolve during reaction measurement, as shown by Guan, et al. [21] and more recently by Corma, et al. [22]. These authors suggest that atomically dispersed species can serve as precursors for the formation of very small clusters of the metal. Hence, it is necessary to use *in situ* spectroscopy to confirm the identity of the species responsible for catalytic reactivity. In this work we used X-ray absorption spectroscopy while performing reaction rate measurements to confirm the role of atomically dispersed Pd for low temperature CO oxidation.

5.2.2 *CO oxidation reactivity*

To probe the catalytic behavior of these samples, we used the CO oxidation reaction under conditions of a modest excess of O_2 (~50% excess O_2). For metallic Pd under these conditions CO oxidation is known to be positive first-order with respect to O_2, and negative first-order with respect to CO[23]. The negative first order kinetics for CO oxidation on platinum group metals are caused by the inhibition due to strong binding of CO to the metal surface. CO acts as a poison and must desorb before the reaction can proceed. When CO is removed from the surface, the catalyst 'lights-off' with the rate increasing quickly with increasing reaction temperature. The exothermic reaction makes

the process auto-catalytic allowing 100% conversion to be achieved rapidly. While light-off curves are useful for benchmarking catalyst performance, to derive kinetics we need to perform measurements at low conversion. We first describe the light-off characteristics of these catalysts and then explore the reaction kinetics.

The light-off curves (Figure 2) were obtained by monitoring CO_2 formation as the catalyst was ramped from room temperature to 300 °C at a rate of 2 °C/min. The catalyst was then cooled to room temperature in the reaction mixture and a second light-off was performed to investigate the stability of the atomically dispersed Pd^{+2} species. As can be seen in Figure 5.2, the first light-off curve for the Pd/La-alumina catalyst shows a distinct S-shape with a positive curvature (negative second derivative) at high conversions during the first cycle. The second light-off curve shows a similar shape as the first one, but as higher conversions are approached, we see a second inflexion point as the curve changes to a negative curvature (positive second derivative). In contrast to the light-off curves for Pd/La-alumina, the Pd/alumina catalyst shows only a sharp increase in CO oxidation reactivity as higher conversions are reached (negative curvature). These characteristicshapes of the light-off curves are indicative of a shift in reaction order for CO oxidationfrom positive order in the case of the S-shaped curve to a negative order for the curves that rise sharply at higher conversions [24]. A negative order of reaction leads to an increase in reaction rate as adsorbed CO is depleted at high conversions. Since metallic Pd shows a negative order of reaction with respect to CO, the observed

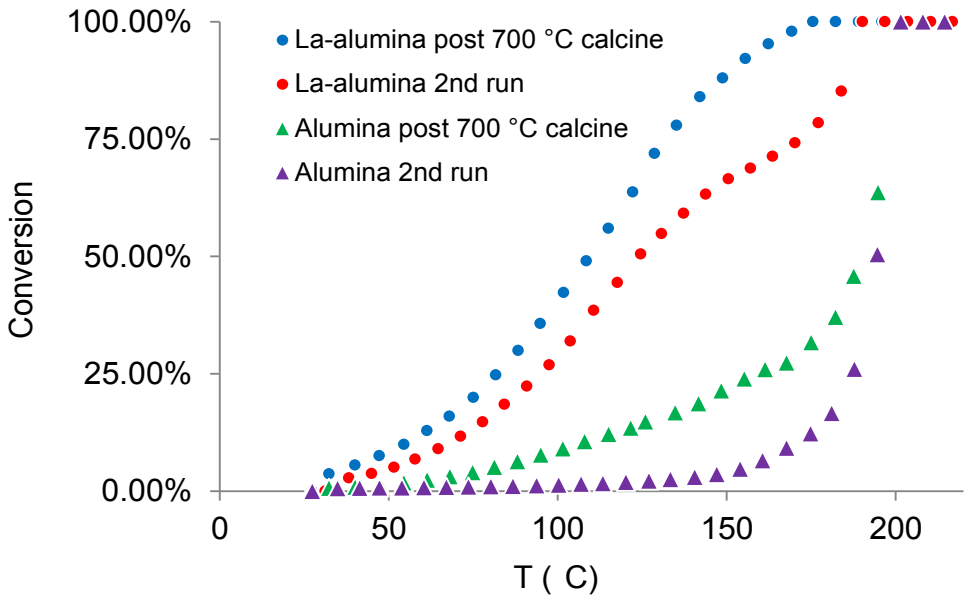

Figure 5.2 CO-oxidation light-off curves for 0.5 wt.% Pd on alumina and La-alumina. The first run was performed after calcining the sample, in situ, at 700 °C for 30 minutes. After the completion of the first run (T_{max}=300 °C), the sample was cooled to room temperature in the reaction mixture and the second run was performed.

changes in the light-off curves suggest that the Pd^{+2} is being reduced during reaction, forming metallic Pd.

The deactivation of the catalyst was studied under isothermal conditions (70°C) to investigate the stability of the high activity state of these catalysts (Fig. A.3) and we see that while the Pd/La-alumina and Pd/alumina deactivate at similar rates, the Pd/alumina sample reactivity eventually approaches zero at 70 °C, while the Pd/La-alumina sample remains active . These longer-term isothermal reaction runs also confirm that the CO_2 formation is catalytic and not caused by the stoichiometric reduction of PdO to Pd, which would take <10 seconds at the flow rates we have used. The turnover frequencies for CO

oxidation were estimated assuming that all of the Pd was atomically dispersed; we find the TOF on Pd/La-alumina to be an order of magnitude greater than on metallic Pd with an activation energy of ~37 kJ/mole, considerably lower than the activation energy of 60-80 kJ/mole for metallic Pd (Table 5.1 gives more details). The temperature dependence of TOFs for Pd alumina, La-alumina and a reference sample of Pd metal powder are presented in Appendix A (Fig. A.4). We also present analysis of transport effects under our experimental conditions and conclude that, due to the low loading of Pd, the kinetic data at low conversion are not subject to any heat and mass transfer limitations (see Appendix A).

5.2.3 *CO oxidation Reaction Kinetics*

Additional experiments were performed where the temperature was kept constant so that the reactivity as a function of reactant composition could be studied. Because the sample reactivity was continuously decaying, the reaction orders were determined by switching

Table 5.1 Turnover frequencies and activation energies for 0.5 wt.% Pd on alumina and La-alumina. The first CO oxidation light-off run was performed after the sample was calcined at 700 °C for 30 minutes in air. After the reactor reached the maximum temperature of 300 °C, the sample was cooled to room temperature and a second CO oxidation light-off run was performed. Reference values obtained from a pure Pd metal powder are also included.

Turnover frequencies (s^{-1})						
	Pd/alumina		**Pd/La-alumina**		**Pd metal[3]**	
	70 °C	125 °C	70 °C	125 °C	70 °C	125 °C
1st run[1]	$3.8x10^{-4}$	$1.6x10^{-3}$	$1.9x10^{-3}$	$7.5x10^{-3}$	$1.3x10^{-4}$	$2.5x10^{-3}$
2nd run[2]	$9.7x10^{-5}$	$2.4x10^{-4}$	$1.2x10^{-3}$	$5.6x10^{-3}$	$6.2x10^{-5}$	$2.0x10^{-3}$

Activation energies (kJ/mol)			
	Pd/alumina	**Pd/La-alumina**	**Pd metal[3]**
1st run[1]	39.4	37.4	56.5
2nd run[2]	22.2	34.3	56.5

1 The first CO oxidation light-off run was performed after the sample was calcined at 700 °C for 30 minutes in air.

2 After the reactor reached the maximum temperature of 300 °C, the sample was cooled to room temperature and a second CO oxidation light-off run was performed.

3 Reference values obtained from a pure Pd metal powder.

reactant flows and comparing the changes in reaction rate before and after the switch in reactant flow rates (Figure 5.3). More details are provided in Appendix A (Fig. A.5), showing how the orders of reaction were derived. Reaction orders are summarized in Table 5.2. Even though the catalyst activity declines, the reaction order for the Pd/La-alumina sample is stable, with the CO reaction order remaining at +0.35 and the O_2 reaction order at +0.15. The positive reaction order with respect to CO, seen for the Pd/La alumina is indicative of a reaction mechanism that is different from that seen on metallic Pd. It is clear that the presence of La helps to stabilize the chemical configuration

responsible for the high reactivity of Pd^{+2} for CO oxidation. The low positive order with respect to O_2 is consistent with a Mars-van Krevelen mechanism, with the oxygen being derived from the surface, rather than the gas phase.

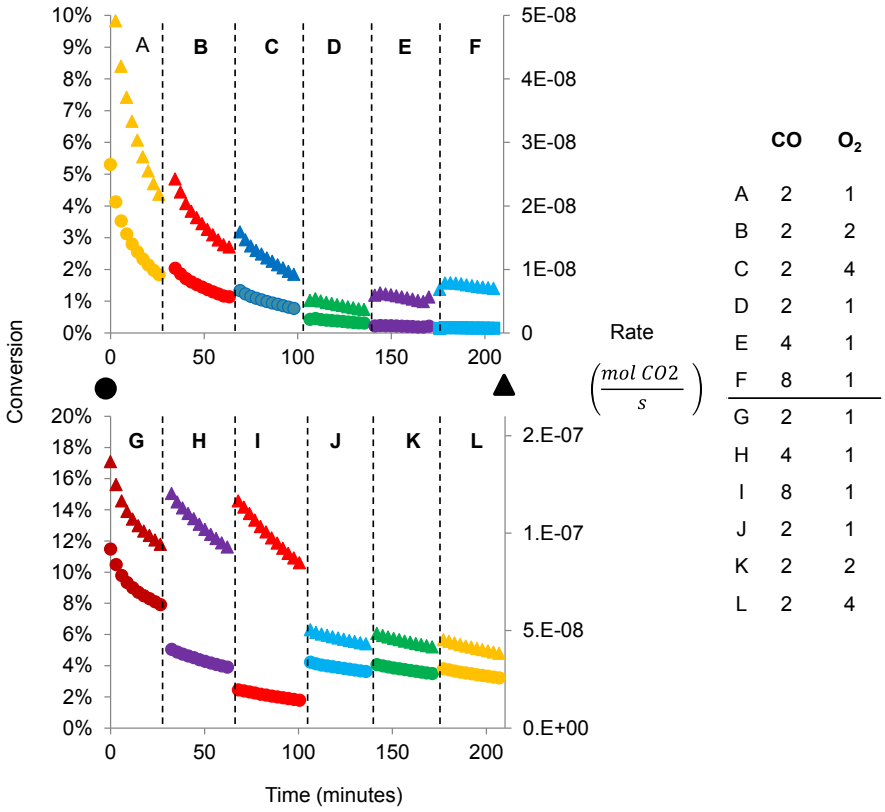

	CO	O_2
A	2	1
B	2	2
C	2	4
D	2	1
E	4	1
F	8	1
G	2	1
H	4	1
I	8	1
J	2	1
K	2	2
L	2	4

Figure 5.3 Isothermal reaction rate measurements to determine orders of reaction for 0.5 wt% Pd on alumina (top), and on La-alumina (bottom). The reaction order for each reactant gas was obtained from the rate change occurring when one of the gas flows was increased or decreased. The table lists reaction gas proportion ($CO:O_2$) for each condition (A-L). The circles refer to the left ordinate axis (% CO conversion) while the triangles refer to the right ordinate axis (rate – moles of CO_2/s for 100 mg of catalyst).

Table 5.2 Reaction order with respect to CO and O_2 for 0.5 wt.% Pd on alumina and La-alumina at 70 °C.

Order of Reaction	**CO**	**O_2**
0.5 wt.% Pd/La-Alumina	0.35	0.15
0.5 wt.% Pd/Alumina	-0.20	0.18
0.5 wt.% Pd/Alumina-Deactivated	-1.20	0.84

The Pd/alumina sample shows distinctly different behavior. The reaction order for CO is negative (-0.2) and continues to decline with time on stream. The order of reaction with O_2 is + 0.16 similar to that on Pd/La-alumina. A notable feature of this catalyst is a spike in CO_2 production for the first data point obtained while increasing the O_2 flow rate (Fig. A.7). This spike suggests that metallic Pd is being oxidized and then this oxide gets converted to CO_2 as steady flows are established. Such spikes were not seen on the Pd/La-alumina catalyst.

After the Pd/alumina has deactivated, it can be regenerated by oxidation at 700 °C and fresh catalyst reactivity behavior is reproduced (Fig. A.7 and Fig. A.8). However, if the catalyst is allowed to deactivate and not re-oxidized, the reaction kinetics change to approximately – 1 order in CO and + 1 order in O_2, the behavior expected for metallic Pd (Fig. A.9). This is consistent with the change in reaction mechanism seen qualitatively by the changes in curvature in Figure 2, transitioning from a more reactive initial state and finally reverting to the behavior of metallic Pd. The results suggest that while

atomically dispersed Pd can be generated on alumina, these species are not stable and transform into a metallic phase. However, on La-alumina these species are more stable, as we show via operando XAS, discussed in the next section. Our reaction rate measurements were performed at temperatures up to 300 °C. Under these conditions the loss of activity due to transformation to metallic Pd clusters was recovered fully via calcination in air.

5.2.4 *Operando X-ray Absorption Spectroscopy (XAS)*

We examined the nature of the Pd during CO oxidation reaction via operando XAS at the Pd K-edge. For the operando study, reaction gases were passed through a vertical packed bed reactor positioned in the X-ray beam with exit gas compositions being analyzed using a gas chromatograph. Figure 4 shows XANES and EXAFS data collected during CO oxidation over a range of temperatures (fits of the EXAFS data are shown in Figure S10). Isosbestic points, indicating that the spectra can be derived by a linear combination of two end member states, are marked by arrows in Figs. 4A and 4B. In Figure 4A, it can be seen that the spectrum from the reference Pd foil passes through the isosbestic points shared by the 0.5 wt.% Pd/alumina sample. This indicates that the spectra collected during CO oxidation can be represented by a linear combination of end member spectra collected from the initial, oxidized sample and from the foil. In contrast, as can be seen in Fig 4B, it is apparent that the Pd foil reference spectrum does not pass through the isosbestic points formed by the spectra collected from the 0.5 wt.% Pd/La-alumina sample in its initial state and during CO oxidation. For this sample, the spectra

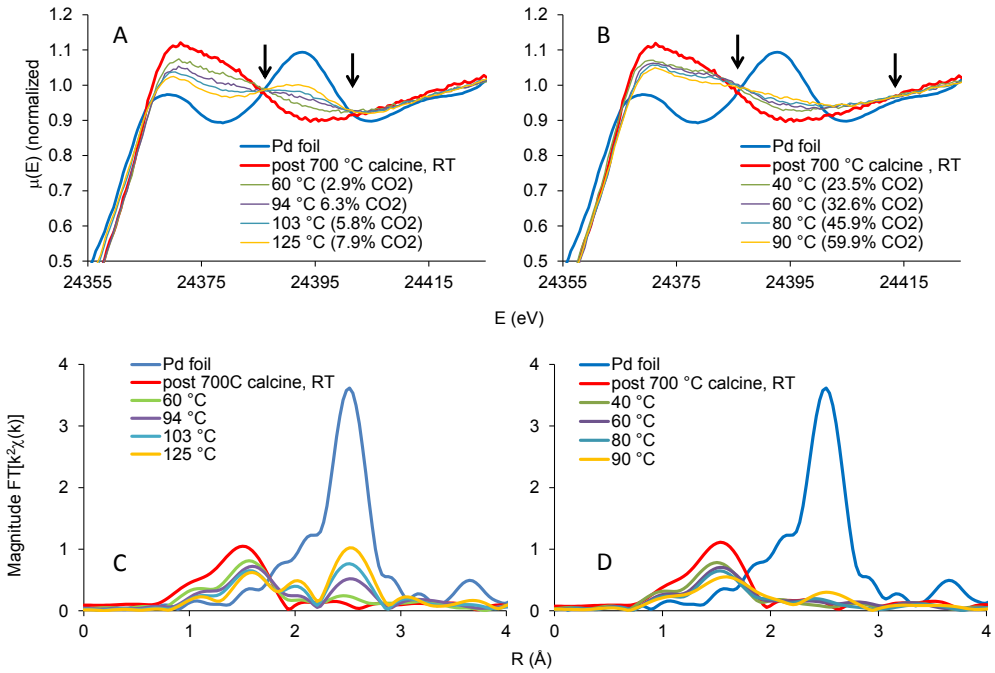

Figure 5.4 XANES spectra and EXAFS k^2-weighted Fourier transforms, obtained at multiple temperatures during CO oxidation, from samples composed of 0.5 wt.% Pd on alumina **(A** and **C)**, and on La-alumina **(B** and **D)**. Arrows point to isosbestic points. Numbers in parentheses are the percent conversion of CO to CO_2 at the time of data collection.

can be described as a linear combination of the initial state spectrum and a third chemical state for the Pd in this sample. This is also reflected in the EXAFS data (Figs 5.4C and 5.4D). In the initial, oxidized state, both samples show only the peak associated with the Pd-O first shell. The absence of a second shell is evidence that, in their initial state, neither sample contains any bulk PdO. In the case of the 0.5 wt% Pd/alumina sample, the decrease in the Pd-O first shell peak height during CO oxidation is immediately accompanied by an increase in the Pd-metal first shell peak height, reflecting the growth of Pd-metal at the expense of Pd-oxide. However, for the 0.5 wt% Pd/La-alumina sample, the PdO first shell peak decreases immediately during CO oxidation at 40 °C, but no Pd-

metal first shell peak is seen until 90 °C. This is evidence for the presence of a third chemical state for Pd in this sample, characterized by an average Pd-O coordination that is significantly less than four. The edge energy observed for this state (24,351.6 ± 0.3 eV) falls between that for Pd metal (24,350 eV) and PdO (24,353 eV). The value of the edge energy for the active state, after accounting for experimental error, is sufficiently different from the Pd^0 and Pd^{2+} reference compounds indicating that this third chemical state is Pd^{+1}.

Figure 5.5 shows the time-resolved variations of the Pd-metal fraction (from linear combination fits of the XANES spectra) and the average Pd-O coordination number (from EXAFS data fits) respectively, together with the % CO conversion (from measurement of the CO_2 fraction in the exit gas). Gas compositions were switched between oxidizing conditions and CO oxidation by keeping the O_2/He flowing and switching the CO flow on and off. This allowed any reduced Pd to get oxidized before restarting CO oxidation at the next higher temperature. In the case of the 0.5 wt% Pd/alumina sample, growth of Pd-metal is seen to begin immediately upon exposure of the sample to CO oxidation conditions at 60 °C (blue), and the catalyst is seen to deactivate as the Pd-metal fraction increases. Partial recovery of the oxide species is obtained upon switching to oxidizing conditions (red). The maximum CO conversion for this sample was approximately 13%. In contrast, the 0.5 wt% Pd/La-alumina sample shows no Pd-metal growth during CO oxidation until 90 °C, and again shows partial oxide species recovery upon switching to oxidizing conditions. However, CO conversion

is significantly higher for this sample, starting at approximately 20% at 40 °C and reaching close to 100% at 90 °C. The EXAFS fitting procedure assumes that a separate Pd metal and oxide phase exists in the sample, the relative amounts determined from the XANES linear combination fits. Using the metal and oxide fractions, the coordination numbers were derived. The Pd-O first shell coordination number for the 0.5 wt% Pd/alumina sample (Figure 5 II A) is seen to decrease slightly from 4 during CO oxidation and fully recover upon switching to oxidizing conditions. In contrast, for the 0.5 wt% Pd/La-alumina sample the Pd-O coordination drops sharply to approximately 3 upon exposure to CO oxidation conditions, recovering nearly fully when switching to oxidizing conditions (Figure 5 II B). From this data it is apparent that the presence of La in the Pd/γ-alumina catalyst stabilizes a state that is highly active toward CO oxidation.

It was found that, while the Pd/La-alumina catalyst deactivated with time on stream, it was possible to restore this catalyst to its initial state via a high temperature oxidation treatment. Figure 5.6A shows sequential light-off curves, obtained from the same Pd/La-alumina catalyst sample. The first run light-off curve shows the initial, high-activity state of the sample, while the second run curve displays partial deactivation. The sample was then treated, in place, to a 30 min, 700 ˚C oxidation treatment (1% O_2/He). It can be seen by the third cycle that that the oxidation treatment has nearly restored the catalyst to

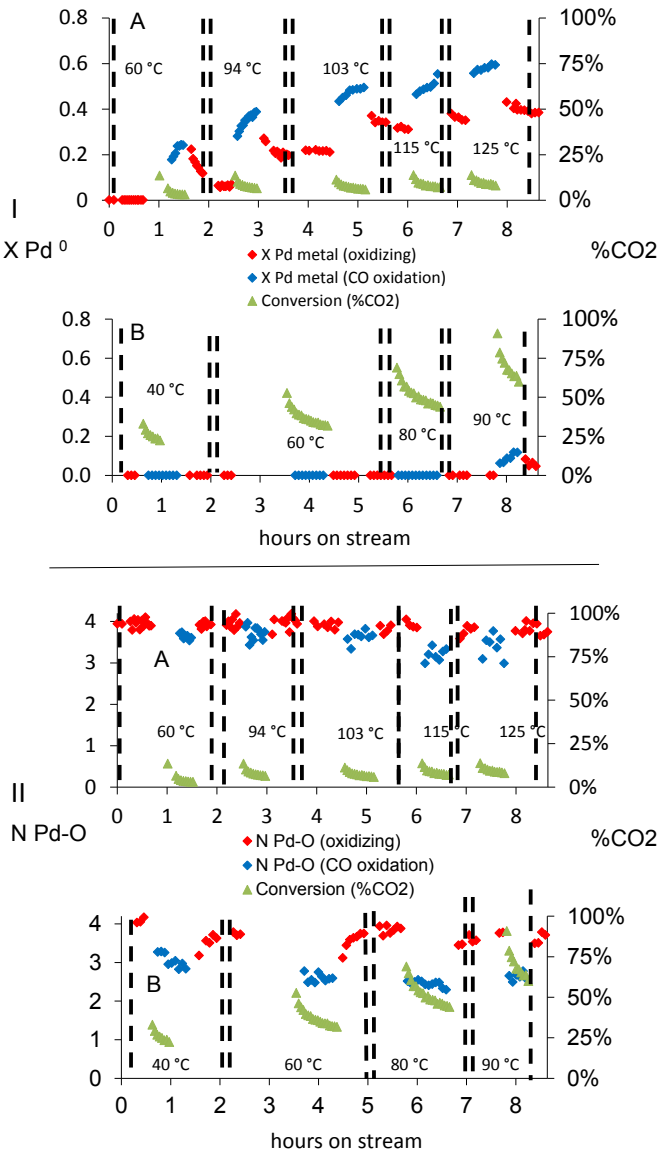

Figure 5.5 Operando CO oxidation reaction/XAS measurements. **(I)** Pd-metal fraction and CO conversion variation as a function of time and temperature during alternating CO oxidation reaction and oxidizing conditions. **(A)** Alumina support. **(B)** La-alumina support. (Pd loading 0.5 wt.%.) **(II)** Pd-O coordination number and CO conversion variation as a function of time and temperature during alternating CO oxidation reaction and oxidizing conditions. **(A)** Alumina support. **(B)** La-alumina support. (Pd loading 0.5 wt.%.).

its initial state. The fourth cycle again shows partial deactivation of the catalyst. Figure 6B (EXAFS Fourier transforms) shows the evolution of the Pd/La-alumina catalyst from its initial state, through CO oxidation at increasing temperatures, and finally to the restored state, following a 700 ˚C oxidation treatment. The initial state shows the Pd oxide first shell (Pd-O), with no Pd oxide second shell (Pd-Pd), which is indicative of atomically dispersed Pd (A). As CO oxidation occurs at increasing temperatures, the Pd metal first shell begins to grow in (B). The sample was taken to 300 ˚C under CO oxidation, and then to 700 ˚C in 1% O_2/He.

In order to explore the structural relationship between La and Pd on γ-alumina, a more detailed analysis of the EXAFS data obtained from the initial-state samples was performed. Examination of several lanthanum palladates reveals a common structural relationship between Pd and La in these compounds, involving square-planar Pd connected to La through two bridging oxygens. The compound La_2PdO_4 was chosen to serve as an analogue, providing initial estimates of structural parameters (Figure 5.7A). Integration of this structural relationship with the γ-alumina structure was achieved by placing the La atom into the 4-fold hollow site provided by an Al^{+3} vacancy,[15] and by replacing an adjacent penta-coordinated Al^{3+} ion (ionic radius (VI octahedral) 0.53 Å) with a Pd^{2+} ion (ionic radius (IV square planar) 0.64 Å) [25] (Fig 7B). The resulting Pd environment, used in the fit to the EXAFS data, is shown in Figure 7C. The apical oxygen, shown in Figure 7C, was omitted from the fits, as inclusion of this oxygen was found to significantly reduce the precision of the fit variables. Although the EXAFS

Fourier transform magnitude at values of R greater than 2 Å is rather low, reasonable fits of the real and imaginary components (Figure S10) and reasonable variable values and uncertainties were obtained (Table 5.3), demonstrating that the structure shown in Figures 5.7B and 5.7C is a plausible representation of the structure of the atomically dispersed Pd on the alumina surface.

5.2.5 *DFT calculations*

To corroborate the experimental results, plane-wave density functional theory (DFT) calculations have been performed using the Vienna *ab initio* simulation package (VASP) [26-28] with the gradient-corrected PW91 exchange-correction functional [29]. Our model for Pd-doped γ-alumina involves the (001) surface of Al_2O_3 [7] (four-fold symmetry) with Pd replacing a surface Al. The details of the DFT calculations and additional results, including the optimized surface structure, can be found in Appendix A. Supported single Pd atoms have been predicted[30] to diffuse easily across the Al_2O_3 surfaces with diffusion barriers on the order of 0.3 eV, and are expected to nucleate[31] quickly to form larger clusters. However, when incorporated into the alumina lattice the Pd atom has both the binding energy and geometrical arrangement necessary to account for the experimental observations that show four fold coordination with oxygen atoms. A reaction mechanism is proposed based on the DFT calculations as displayed in Figure 8, where the energetics is also shown. In this putative mechanism, the catalytic cycle is initiated by the adsorption of CO onto the Pd, which then reacts with a lattice

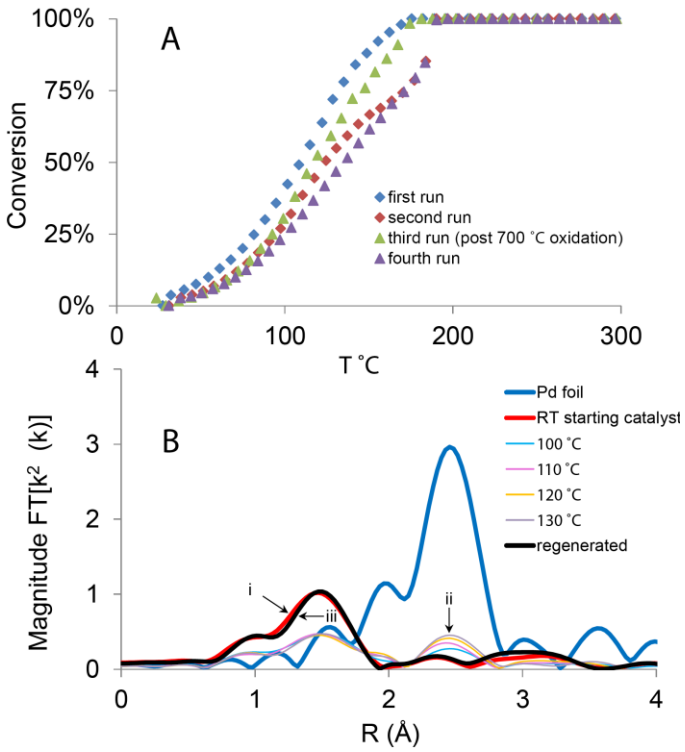

Figure 5.6 (A) CO oxidation light-off curves for the 0.5 wt% Pd on La-alumina sample, showing that the catalyst is nearly regenerated after a 30 m, 700 ˚C oxidation treatment. **(B)** EXAFS Fourier transform plots showing (i) the state of the starting catalyst, and (ii) the growth of Pd metal during CO oxidation. The catalyst was heated to 300 ˚C under CO oxidation and then re-oxidized at 700 ˚C, restoring the catalyst to its starting state (iii).

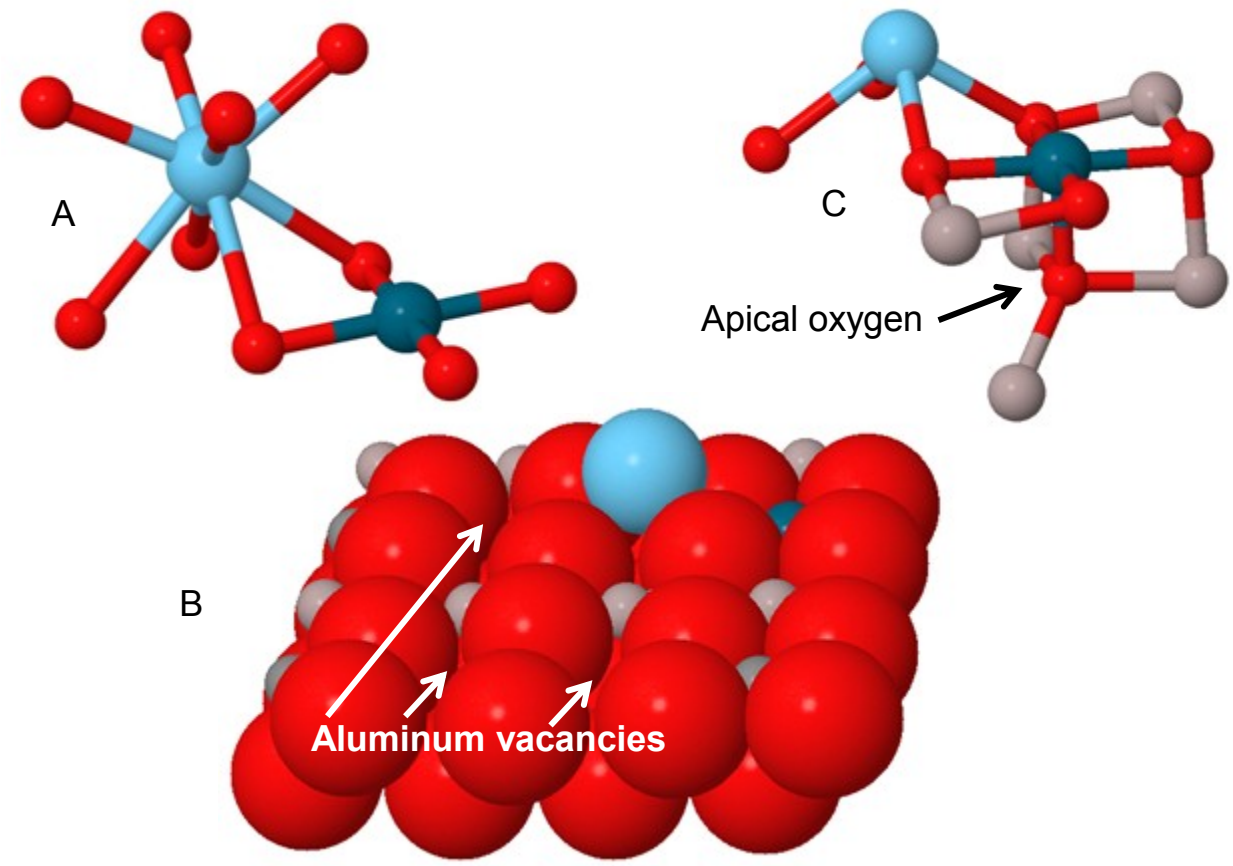

Figure 5.7 (A) La and Pd relationship in the La_2PdO_4 structure. **(B)** Space-filling γ-alumina (100) surface model (spinel basis) with La and Pd. **(C)** Model for EXAFS fit, based on B. Atoms are: oxygen/red, aluminum/gray, palladium/dark blue, and lanthanum/light blue.

oxygen (O_{lat}) coordinated with Pd. After overcoming an activation barrier of 0.26 eV, an intermediate (INT1) was found with E_r = -0.46 eV. At the transition state, the C-O bond length and the C-O_{lat} distance are computed to be 1.16 and 1.82 Å, respectively. Several steps are needed to eventually produce CO_2, which promptly desorbs removing O_{lat} in the process. The second half of the catalytic cycle starts with the newly formed oxygen vacancy from the first step, in which Pd is now coordinated to three lattice oxygen atoms with distances of 2.15, 2.27, and 2.49 Å. The adsorption of an O_2 molecule ($O_{2\ gas}$ / O_{gas})

at the vacancy is highly exothermic, with its bond length elongated from 1.23 Å in the isolated molecule to 1.45 Å. This is followed by the adsorption of CO on Pd, which promptly reacts with the pre-adsorbed $O_{2\ gas}$ nearby. This step has an energy barrier of 0.27 eV and the exothermicity is found to be -3.66 eV. At the transition state, the C-O and the C-O_{gas} bond lengths are calculated to be 1.16 and 1.94 Å, respectively. By releasing the CO_2 product, the Pd recovers its tetra-coordinated state on the γ-Al_2O_3(100) surface. Additional results from the DFT calculations, including geometry, energetics, and charge analyses, can be found in Appendix A.

5.3. Discussion

The stabilization of atomically dispersed transition metals such as Au, Pt, and Rh on reducible oxides such as TiO_2, FeO_x and CeO_2 has been reported recently [2, 3, 20]. These catalysts have been shown to be active for reactions such as CO oxidation, water gas shift and also for olefin hydrogenation. However, reports on the stabilization of precious metals on high surface alumina are very scarce [9, 32]. The presence of atomically dispersed Pd on alumina was suggested based on XPS spectra in the early 80s. Hence, the present study is consistent with these previous observations that have demonstrated that the alumina surface has sites where isolated ionic forms of transition metals can be present. What has not been recognized in previous work is that atomically dispersed La^{+3} may play an important role in stabilizing ionic forms of Pd^{+2} on the alumina surface. We showed previously [18, 33] that the presence of the La^{+3} on the

Table 5.3 Results of fits to EXAFS data collected from 0.5 wt.% Pd on alumina and La-alumina samples, post 700 °C calcine.

			Alumina		La-alumina	
	# variables		12		14	
	Reduced χ^2		12.1		38.0	
	R-factor		0.0240		0.0116	
	S_0^2		0.832		0.872	
	ΔE_0 (eV)		1.3±2.4		5.6±1.8	
			1st shell			
Model values			Alumina sample		La-alumina sample	
atoms	r_{model}(Å)	N	r_{fit}(Å)	σ^2(Å^2)	r_{fit}(Å)	σ^2(Å^2)
sq-planar O1	2.02	4	2.02±0.02	0.004±0.002	2.01±0.01	0.005±0.002
			2nd shell			
atoms	r_{model}(Å)	N	r_{fit}(Å)	σ^2(Å^2)	r_{fit}(Å)	σ^2(Å^2)
Al3 2e 1	2.78	1	†2.78±0.10	†0.008±0.009	†2.80±0.07	†0.008±0.009
Al3 2e 2	2.80	1	†2.81±0.10	†0.008±0.009	†2.83±0.07	†0.008±0.009
Al5 4f 1	2.94	1	3.1±0.2	0.00±0.02	3.02±0.07	0.00±0.02
Al6 4f 1	2.94	1	3.0±0.2	0.00±0.03	3.2±0.2	0.00±0.03
Al2 2e 1	3.34	1	3.4±0.2	0.00±0.01	3.4±0.1	0.00±0.01
			3rd shell			
	r_{model}(Å)	N			r_{fit}(Å)	σ^2(Å^2)
La 1	3.43	2			3.74±0.07	0.012±0.009

† constraints: $\Delta r_{Al3\ 1e} = \Delta r_{Al3\ 2e}$ and $\sigma^2_{Al3\ 1e} = \sigma^2_{Al3\ 2e}$

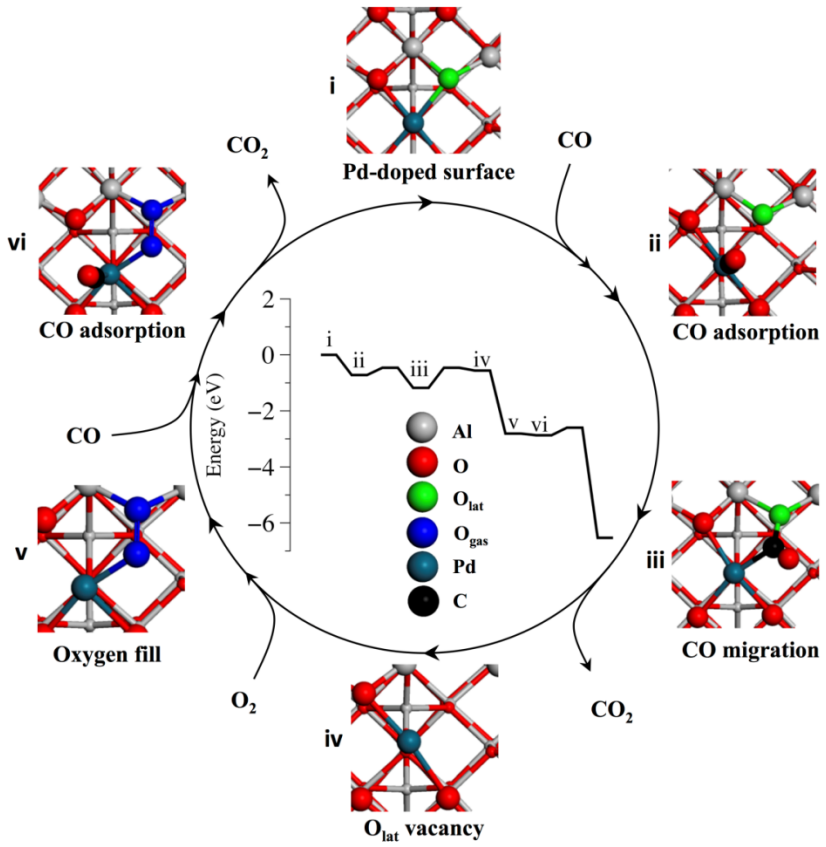

Figure 5.8. Proposed reaction mechanism for CO oxidation on isolated Pd on the γ-alumina (100) surface.

surface may also help in slowing rates of catalyst sintering and help nucleate sub-nm clusters of the metal that may be responsible for the enhanced reactivity seen on the La-alumina catalysts.

Since isolated single atom species may not be stable during reaction, it is necessary for practical applications to develop methods to regenerate these species. We show in this work that high-temperature calcination in air helps to re-disperse the Pd and restore catalytic activity. The atomic dispersion of the Pd after high temperature

calcination was confirmed by XAS; we have also performed AC-STEM studies to verify this re-dispersion process. The energetics of re-dispersion of Pd suggests that sub-nm clusters of Pd may be easier to disperse through this route, while bulk PdO is very stable and may not be easily redispersed. A high-temperature calcination step (700 °C) seems to be most effective at restoring catalytic activity of the isolated Pd species, although 500 °C calcination was also found to partially restore the lost catalytic activity. It is possible that desorption of hydroxyl groups from the alumina surface facilitates the re-dispersion process (we see evidence for loss of water during calcination). It was shown recently that calcination of alumina to 700 °C creates a more active form of alumina[34]. Since oxidation of Pd commences around 200 °C and is complete by 500 °C, the beneficial effect of higher temperature calcination must be the rearrangements on the alumina surface that are perhaps similar to those described by Wischert, et al. [34]. The facile re-dispersion of single isolated Pd atoms makes this Pd/alumina system more suitable for industrial applications.

DFT computations in the literature suggest that, among the transition metals, Pd would likely be the most strongly bound to alumina [32]. This may explain why we are able to generate catalysts that are composed exclusively of isolated Pd species. Previous studies of single-atom catalysts of Au, Rh or Pt always reported the co-existence of the atomically dispersed and nanoparticle phases, making it difficult to derive specific reactivity for the single-atom species. In several studies, the authors leached out the nanoparticle phase (for example using cyanide) leaving behind the atomically dispersed species on the support. This step was not needed in our experiments due to the higher

stability of the Pd on alumina, especially in the presence of La^{3+}. The study of complex oxides has shown that cations of Pd, Au or Pt can be stabilized in these oxides[35]. A common feature in these mixed oxides is the presence of high oxidation state cations like La^{3+}. We therefore believe that the role of La^{3+} on the alumina surface is similar to that in these mixed oxides.

For oxidation reactions, the proposed mechanism involves the participation of oxygen atoms from the support. In the case of reducible oxides, it is expected that the removal of oxygen from the support is facile causing the cations in the support to change oxidation state when it is reduced. This is the case with CeO_2 or TiO_2 that are known to be easy to reduce. However, these reducible oxide supports are also susceptible to loss of surface area during high temperature operation, and they tend to form strongly bound carbonates or other reaction products that can poison the catalyst. There have been very few reports of the reactivity of atomically dispersed Pd on non-reducible supports such as alumina[10, 17, 32]. The presence of atomically dispersed Pt has been demonstrated previously[9, 10] but these species show CO oxidation light off temperature higher than that of Pt metal[1]. Our results show that the atomically dispersed Pd sites show exceptional activity at low temperatures where metallic Pd surface sites are not active because they are poisoned by strongly adsorbed CO. The ionic form of Pd is not poisoned by adsorbed CO since it is bound less strongly, consistent with the positive order in CO oxidation kinetics. The weakly bound, reversible CO adsorption seems to be the key difference between Pd metal sites and isolated atomic species. Providing oxygen from the support makes it possible to complete the catalytic cycle with a lower activation

barrier than on metallic Pd. The barrier calculated from the DFT calculations (0.27 eV) is similar to the apparent activation energy measured experimentally. Furthermore, since the oxygen comes from the support, it is therefore reasonable that the order of reaction with oxygen is near zero. As we explain in the Appendix A, doping of the ionic Pd in alumina (which is achieved only after high temperature calcination) yields oxygen atoms that bridge the Al and Pd sites. These bridging oxygens, being different from those seen on stable alumina surfaces, can participate in the CO oxidation reaction. We therefore propose a reaction mechanism that differs from the conventional Langmuir Hinshelwood mechanism which operates on metallic Pd surfaces. The Bader charge analysis presented in Appendix A shows that we should not consider these active sites as being single atom analogs of homogeneous catalysts but rather they involve the participation of the extended alumina support surface.

In summary, this work shows how atomically dispersed La^{3+} ions may play a key role in helping to stabilize atomically dispersed ionic Pd on the alumina surface. Our XANES results show that atomically dispersed Pd^{1+} is the active center for CO oxidation, and that the catalytic behavior of these species is *very* different from that of Pd metal. A novel catalytic mechanism is proposed to explain the unexpected reactivity for the isolated Pd species. The ability to atomically disperse transition metals on industrially relevant high surface area supports paves the way to develop more efficient use of expensive platinum group metals as catalysts.

5.4. Methods

5.4.1 *Electron Microscopy*

Aberration-corrected high-angle annular dark-field (AC HAADF) images were collected at Oak Ridge National Laboratory - High Temperature Materials Laboratory, using a JEOL 2200FS electron microscope, equipped with a CEOS GmbH (Heidelburg, Ger.) corrector on the probe-forming lenses. Images were obtained from a sample composed of La-alumina (4 wt. % La_2O_3; W. R. Grace (MI-386)), loaded with 2.5 wt.% Pd. Images were also collected from the same support material, without Pd, for comparison to the images obtained from the Pd-loaded sample. Measurement of the electron backscatter intensity was performed by fitting 2-dimensional Gaussian functions to the clusters of atoms seen in the images, using a MATLAB algorithm.

5.4.2 *Catalyst Preparation*

For the alumina support, Dispal (boehmite) from Sasol was calcined at 650 °C for 10 hr to make γ-alumina, and the BET surface area was determined to be 153 $m^2 g^{-1}$. The La-alumina support, containing 4 wt. % La_2O_3, was obtained from W. R. Grace (MI-386), and has a BET surface area of 176 $m^2 g^{-1}$. The BET surface areas were measured on a Micromeritics Gemini 2360 instrument under liquid nitrogen at 77K. Samples were prepared by dry impregnation of γ-alumina powders with a solution of palladium amine nitrate, diluted to the appropriate concentration to achieve 0.5 wt.% Pd-loading after three impregnations. Samples were dried at 110 °C after each impregnation, and finally

calcined at 700 °C for 1 hour in a box furnace in ambient air. The temperature was raised at a slow rate 2 °C/minute to help generate the best dispersion of the Pd oxide phase.

5.4.3 *CO oxidation reactivity*

For CO oxidation reactivity measurements, 100 mg of sample was packed between quartz wool plugs inside a stainless steel reactor tube mounted in a high-temperature oven. The sample was pretreated as follows: 100 mg of sample was heated to 700 °C under O_2/He for at least 30 minutes. Samples were cooled under oxidizing conditions to room temperature where the CO oxidation reaction mixture was introduced. The flow rates consisted of 0.8ml/min O_2, 0.7ml/min CO, and 70ml/min He. The samples were then heated to 300°C at 2°C/min and cooled back down to room temperature in the reaction mixture, and a second, identical ramp was then performed. Reaction kinetics measurements were conducted after another 700 °C pretreatment, and then cooling the sample to 70 °C. The reactant mixtures were allowed to flow and as the catalyst activity was lost over time, the reactant flow rates were varied by either increasing the O_2 flow rate while keeping CO flow constant or by an increase in CO flow rate with constant O_2 flow. Exit gas composition was measured using a Varian CP-4900 Micro-GC gas chromatograph (GC), utilizing a TCD detector.

5.4.4 *X-ray absorption Spectroscopy*

Operando X-ray absorption spectroscopy (XAS) was performed at the Argonne National Laboratory Advanced Photon Source beam-line 10-ID. The samples (200 mg) were packed into 10 mm (I.D.) quartz NMR tubes and were supported between two

quartz wool plugs. The tubes were mounted vertically in a tube furnace, and gas flow was from top to bottom through the packed sample bed. Gas flow rates were controlled using Sierra mass flow controllers. The exit gas composition was analyzed using the same Varian CP-4900 Micro-GC gas chromatograph. After being loaded into the reactor tube, the samples were given an oxidizing pretreatment in flowing 1% O_2/He at 50 ml/min, by ramping to 700 °C at 20 °C/min and holding for 30 min. The samples were then cooled to room temperature under flowing gas, and XAS data was collected, without intervening exposure to ambient air. The CO reaction mixture consisted of 0.7 mL/min CO, 0.8 mL/min O_2, diluted in He with a total gas flow rate of 140 mL/m. This was achieved by mixing ~1% O_2/He and ~1% CO/He using the mass flow controllers. The experimental procedure was to ramp the temperature with the CO flow turned off, stabilize the temperature, turn on the CO flow for 30-45 m, and finally turn the CO off and ramp to the next temperature. (Turning off the CO gas feed reduced the total flow by approximately one half.) Gas analysis and XAS collection were performed continuously during these changes in flow rates and temperatures.

The XANES and EXAFS data were analyzed using the Athena and Artemis software [36, 37]. Palladium oxide and metal fractions were determined from linear combination fits of XANES Pd-oxide and metal end member standards. The XANES spectrum obtained from the initial, post-700 ˚C oxidation state of each catalyst was chosen as the palladium oxide standard. It was assumed that this spectrum represented atomically dispersed palladium in square-planar coordination with oxygen, and palladium

oxide S_0^2 values were refined for the alumina and La-alumina samples using these spectra. Pd-foil reference spectra were chosen as the Pd metal standards. In the non-isosbestic cases (ie. when Pd-metal was present in La-alumina-supported catalyst) a third linear combination standard, representing $Pd^{\delta+}$, was used. The metal-free sample with the smallest Pd-O coordination number (the final 80 ˚C CO-oxidation spectrum) was chosen to represent this end member.

The EXAFS data was analyzed using a two-phase, oxide/metal model. The phase fractions were fixed at the values obtained from the linear combination fits of the XANES data. The Pd-oxide Pd-O and Pd-metal Pd-Pd coordination numbers were refined for each spectrum with the Pd-oxide and Pd metal S_0^2 values fixed at those obtained from the Pd-oxide and metal standards.

Acknowledgements

We gratefully acknowledge funding for this work provided by the U.S. DOE, Office of Science grant DE-FG02-05ER15712. S.L. thanks the National Natural Science Foundation of China (21203026). R.S.J. and H.G. thank the US National Science Foundation (CHE-0910828). Use of the Advanced Photon Source is supported by the Office of BasicEnergy Sciences of the U.S. DOE under contract number W-31-109-Eng-38. Materials Research Collaborative Access Team (MRCAT, Sector 10 ID-B) operations are supported by the Department of Energy and the MRCAT member institutions. STEM imaging was performed at the High Temperature Materials Laboratory, operated by Oak Ridge National Laboratory and supported by DOE, EERE Office of Vehicle

Technologies. J.T.M. was supported by the U.S. Department of Energy, Office of Basic Energy Sciences, Chemical Sciences under contract DE-AC-02-06CH11357. F.H.R. acknowledges support from the Department of Energy, Office of Basic Energy Sciences, Chemical Sciences, under Grant DE-FG02-03ER15408. C.H.F.P. and J.H.K. were supported by the U.S. Department of Energy, Office of Basic Energy Sciences, Division of Chemical Sciences, Geosciences and Biosciences. Their studies were performed in the Environmental Molecular Sciences Laboratory, a national scientific user facility sponsored by the U.S. Department of Energy's Office of Biological and Environmental Research and located at Pacific Northwest National Laboratory. E.J.P. thanks Bruce Ravel and Anatoly Frenkel for discussion and guidance with regard to the XAS analysis

References

1. Moses-DeBusk, M., et al., *CO Oxidation on Supported Single Pt Atoms: Experimental and ab Initio Density Functional Studies of CO Interaction with Pt Atom on theta-Al2O3(010) Surface.* Journal of the American Chemical Society, 2013. **135**(34): p. 12634-12645.
2. Flytzani-Stephanopoulos, M., *Gold Atoms Stabilized on Various Supports Catalyze the Water–Gas Shift Reaction.* Accounts of Chemical Research, 2013.
3. Qiao, B.T., et al., *Single-atom catalysis of CO oxidation using Pt-1/FeOx.* Nature Chemistry, 2011. **3**(8): p. 634-641.
4. Lin, J., et al., *Remarkable Performance of Ir1/FeOx Single-Atom Catalyst in Water Gas Shift Reaction.* Journal of the American Chemical Society, 2013. **135**(41): p. 15314-15317.
5. Boronin, A.I., et al., *Investigation of palladium interaction with cerium oxide and its state in catalysts for low-temperature CO oxidation.* Catalysis Today, 2009. **144**(3-4): p. 201-211.
6. Sohlberg, K., S.J. Pennycook, and S.T. Pantelides, *The bulk and surface structure of gamma-alumina.* Chemical Engineering Communications, 2000. **181**: p. 107-135.
7. Digne, M., et al., *Use of DFT to achieve a rational understanding of acid-basic properties of gamma-alumina surfaces.* Journal of Catalysis, 2004. **226**(1): p. 54-68.
8. Krokidis, X., et al., *Theoretical study of the dehydration process of boehmite to gamma-alumina.* Journal of Physical Chemistry B, 2001. **105**(22): p. 5121-5130.
9. Kwak, J.H., et al., *Coordinatively unsaturated AlI^{3+} centers as binding sites for active catalyst phases of platinum on gamma-Al_2O_3.* Science, 2009. **325**: p. 1670-1673.
10. Mei, D.H., et al., *Unique role of anchoring penta-coordinated Al^{+3} sites in the sintering of gamma-Al_2O_3-supported Pt catalysts.* Journal of Physical Chemistry Letters, 2010. **1**(18): p. 2688-2691.
11. McVicker, G.B., R.L. Garten, and R.T.K. Baker, *Surface-area stabilization of Ir-Al_2O_3 catalysts by CaO, SrO, and BaO under oxygen atmospheres - Implications on mechanism of catalyst sintering and re-dispersion.* Journal of Catalysis, 1978. **54**(2): p. 129-142.
12. Schaper, H., et al., *Thermal stabilization of high surface-area alumina.* Solid State Ionics, 1985. **16**(1-4): p. 261-265.
13. Schaper, H., E.B.M. Doesburg, and L.L. Vanreijen, *The influence of lanthanum oxide on the thermal-stability of gamma alumina catalyst supports.* Applied Catalysis, 1983. **7**(2): p. 211-220.

14. Haack, L.P., et al., *Characterization of lanthanum-modified gamma-alumina by X-ray photoelectron-spectroscopy and carbon-dioxide absorption.* Applied Catalysis a-General, 1992. **82**(2): p. 199-214.
15. Wang, S.W., et al., *Dopants adsorbed as single atoms prevent degradation of catalysts (vol 3, pg 143, 2004).* Nature Materials, 2004. **3**(4): p. 274-274.
16. Otto, K., L.P. Haack, and J.E. Devries, *Identification of 2 types of oxidized palladium on gamma-alumina by X-ray photoelectron-spectroscopy.* Applied Catalysis B-Environmental, 1992. **1**(1): p. 1-12.
17. Hackett, S.E.J., et al., *High-activity, single-site mesoporous Pd/Al_2O_3 catalysts for selective aerobic oxidation of allylic alcohols.* Angewandte Chemie-International Edition, 2007. **46**(45): p. 8593-8596.
18. Gaudet, J.R., et al., *Improved low-temperature CO oxidation performance of Pd supported on La-stabilized alumina.* ACS Catalysis, 2013: p. 846-855.
19. Krivanek, O.L., et al., *Atom-by-atom structural and chemical analysis by annular dark-field electron microscopy.* Nature, 2010. **464**(7288): p. 571-574.
20. Guan, Y. and E.J.M. Hensen, *Cyanide leaching of Au/Ceo2: Highly active gold clusters for 1,3-butadiene hydrogenation.* Physical Chemistry Chemical Physics, 2009. **11**(41): p. 9578-9582.
21. Guan, Y.J., et al., *Gold stabilized by nanostructured ceria supports: Nature of the active sites and catalytic performance.* Topics in Catalysis, 2011. **54**(5-7): p. 424-438.
22. Corma, A., et al., *Exceptional oxidation activity with size-controlled supported gold clusters of low atomicity.* Nature Chemistry, 2013. **5**(9): p. 775-781.
23. Berlowitz, P.J., C.H.F. Peden, and D.W. Goodman, *Kinetics of CO oxidation on single-crystal Pd, Pt, and Ir.* Journal of Physical Chemistry, 1988. **92**(18): p. 5213-5221.
24. Duprat, F., *Light-off curve of catalytic reaction and kinetics.* Chemical Engineering Science, 2002. **57**(6): p. 901-911.
25. Shannon, R.D. and C.T. Prewitt, *Effective ionic radii in oxides and fluorides.* Acta Crystallographica Section B-Structural Crystallography and Crystal Chemistry, 1969. **B 25**: p. 925-&.
26. Kresse, G. and J. Hafner, *Ab initio molecular dynamics for liquid metals.* Phys. Rev. B, 1993. **47**: p. 558-561.
27. Kresse, G. and J. Furthmuller, *Efficient iterative schemes for ab initio total-energy calculations using plane wave basis set.* Phys. Rev. B, 1996. **54**: p. 11169-11186.
28. Kresse, G. and J. Furthmuller, *Efficiency of ab initio total energy calculations for metals and semiconductors using plane wave basis set.* Comp. Mater. Sci., 1996. **6**: p. 15-50.
29. Perdew, J.P., et al., *Atoms, molecules, solids, and surfaces: Applications of the generalized gradient approximation for exchange and correlation.* Phys. Rev. B, 1992. **46**: p. 6671-6687.

30. Valero, M.C., P. Raybaud, and P. Sautet, *Influence of the hydroxylation of gamma-Al2O3 surfaces on the stability and diffusion of single Pd atoms: A DFT study.* Journal of Physical Chemistry B, 2006. **110**(4): p. 1759-1767.
31. Valero, M.C., P. Raybaud, and P. Sautet, *Nucleation of Pd-n (n=1-5) clusters and wetting of Pd particles on gamma-Al2O3 surfaces: A density functional theory study.* Physical Review B, 2007. **75**(4).
32. Narula, C.K. and G.M. Stocks, *Ab initio density functional calculations of adsorption of transition metal atoms on theta-Al_2O_3 (010) surface.* Journal of Physical Chemistry C, 2012. **116**(9): p. 5628-5636.
33. Xu, Q., et al., *The sintering of supported Pd automotive catalysts.* Chemcatchem, 2011. **3**(6): p. 1004-1014.
34. Wischert, R., et al., *Gamma-alumina: The essential and unexpected role of water for the structure, stability, and reactivity of "defect" sites.* Journal of the American Chemical Society, 2012. **134**(35): p. 14430-14449.
35. Kurzman, J.A., L.M. Misch, and R. Seshadri, *Chemistry of precious metal oxides relevant to heterogeneous catalysis.* Dalton Transactions, 2013. **42**(41): p. 14653-14667.
36. Ravel, B., *ATOMS: crystallography for the X-ray absorption spectroscopist.* Journal of Synchrotron Radiation, 2001. **8**: p. 314-316.
37. Ravel, B. and M. Newville, *ATHENA, ARTEMIS, HEPHAESTUS: data analysis for X-ray absorption spectroscopy using IFEFFIT.* Journal of Synchrotron Radiation, 2005. **12**: p. 537-541.

Appendix A Supporting Information (Chapter 5)

A.1 TEM-EDS.

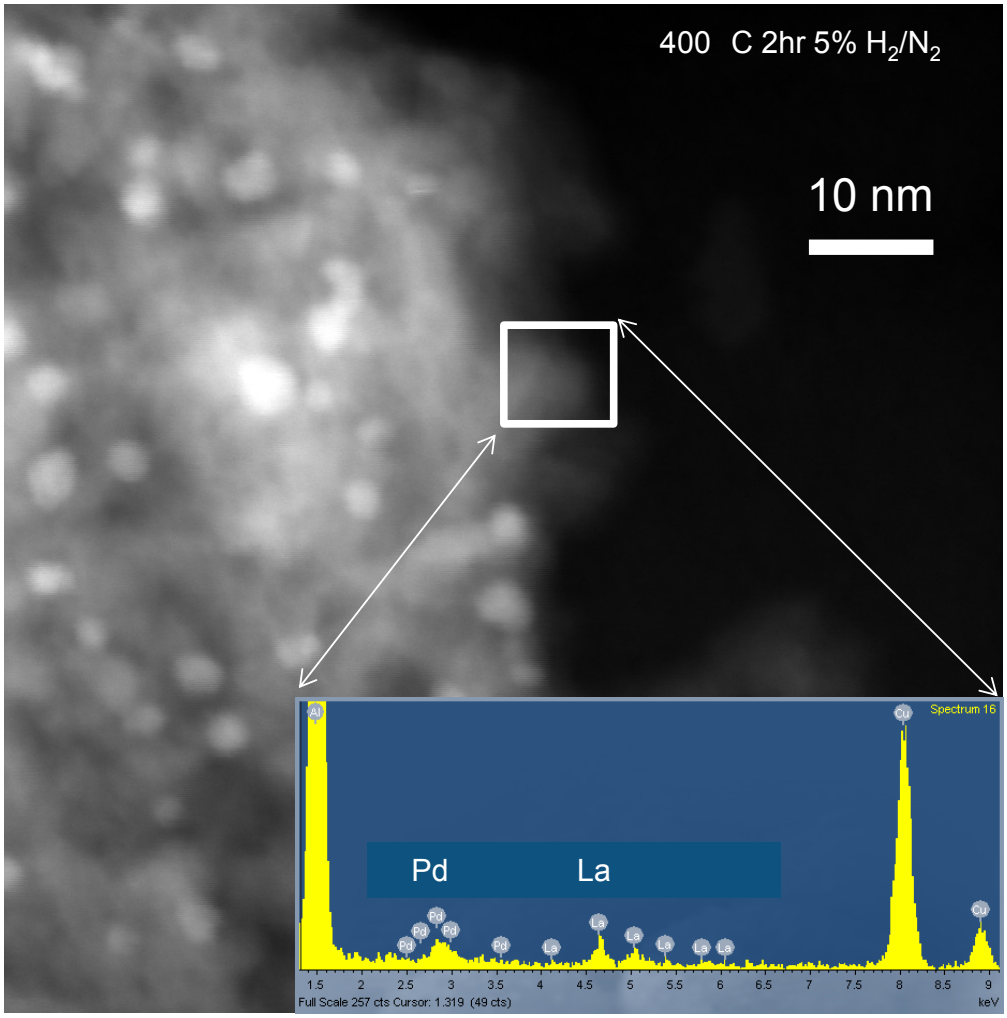

Figure Error! No text of specified style in document.**.1** Energy Dispersive Spectroscopy (EDS) analysis of the boxed region in the 2.5 wt% Pd/La-alumina catalyst. The region in the box is devoid of any detectable metallic particles (which are the bright objects in the figure). EDS analysis shows the presence of Pd and La from this region.

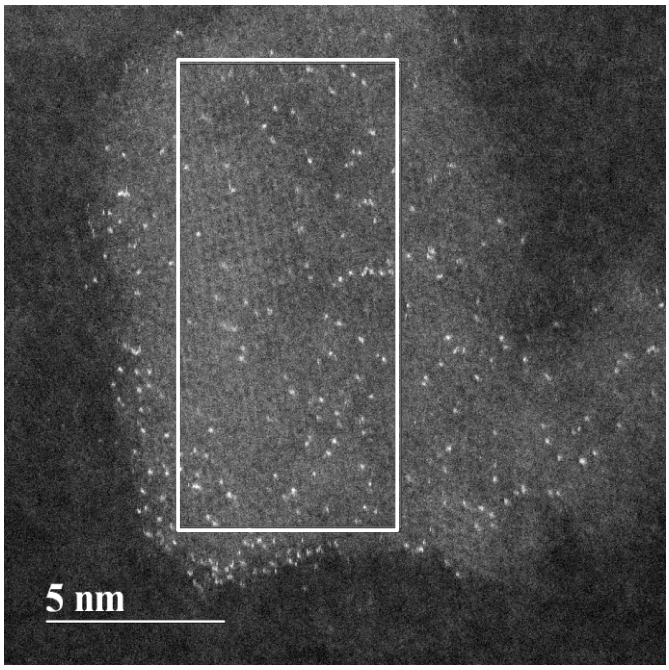

Figure Error! No text of specified style in document.**.2** Aberration corrected STEM image of 0.5 wt.% Pd on 4 wt.% La/Alumina.

By using the projected area of an alumina flake, we can estimate the number of atoms per unit surface area. We count 91 atoms in an area measured to be 79.75nm^2 (white rectangle). This comes to 1.14 atoms/nm$^{\mathbf{2}}$. The expected number of atoms based on a loading of 0.5 wt.% Pd and 4 wt.% La is shown in Table 5.S1 below and the total number of atoms is consistent with the number of atoms we have counted on the alumina surface. The number of observed atoms is much less than the expected number of sites (based on the geometric model presented in Figure 5.7) where La^{3+} or Pd^{2+} could be accommodated on the alumina surface. Steric and charge effects may limit the amount of La^{3+} that can be accommodated without forming a separate La_2O_3 phase. Beguin et al[1] suggest this

upper limit is about 10 wt% Lanthanum, suggesting that we have the possibility to increase the number of cationic anchoring sites.

From our calculation using 0.5wt% Pd and 4.0wt% La on our $Pd/LaAl_2O_3$ sample with a specific surface area of 176 m^2/g we get the results in the table below, similar to the image calculation.

Table Error! No text of specified style in document.**.1** Pd and La atom surface density.

atoms Pd/area m^2	1.60759E+17
atoms La/area m^2	9.85297E+17
Total Atoms/area m^2	1.14606E+18

A.2 CO oxidation kinetics

A.2.1 *CO oxidation reactivity as a function of time*

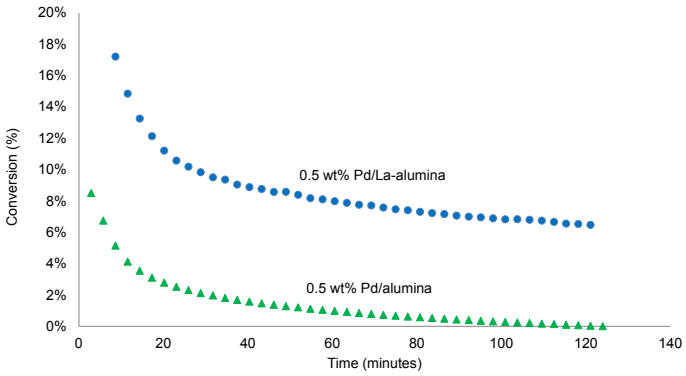

Figure Error! No text of specified style in document.**.3** Deactivatition of Pd/alumina and Pd/La-alumina with time.

We assume all atoms of Pd are on the surface, hence from the known weight of catalyst and the metal loading, we know the total weight of metal used, and we can convert it to moles of Pd_s. We calculate TOF as follows:

$$\boldsymbol{TOF = \frac{mol\ CO_2\ produced}{mols\ Pd_s - sec}} \qquad \textbf{Equation 5.1}$$

We use the data at low conversions where we can assume differential reactor conditions. We used 0.7ml/min CO, 0.8ml/min O_2, and 70ml/min He with 100mg of catalyst loaded into our reactor. The 0.5wt%Pd on La-Al_2O_3 is much more active than the 0.5wt% Pd/Al_2O_3 catalyst whose reactivity is higher than that of Pd metal powder

which is used as a reference. The plot below shows the TOFs for the catalysts tested along with the apparent activation energies derived from the slope of the line.

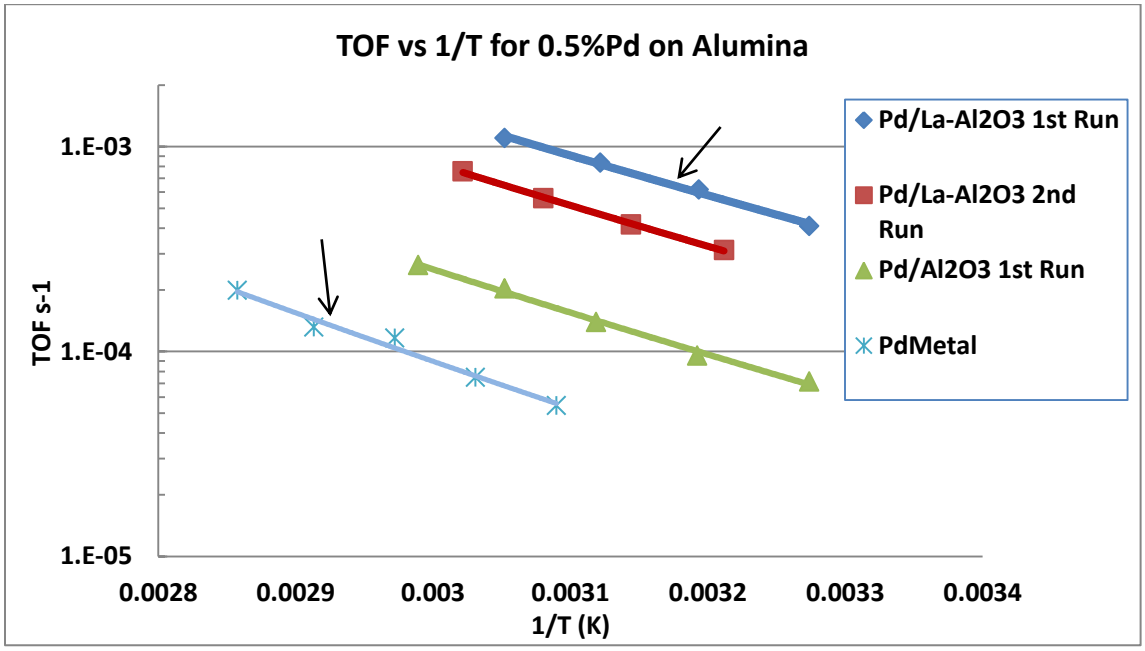

Figure Error! No text of specified style in document.**.4** Turn over frequency (TOF) vs 1/T plot for multiple Pd/Al_2O_3 samples with indicated activation energies.

A.2.2 *Order of reaction for 0.5wt%Pd/La-Al_2O_3*

These catalysts deactivate during CO oxidation runs performed under stoichiometric conditions, hence a modified procedure was used to determine reaction orders in CO and O_2. The catalyst was first pretreated at 700°C under oxidizing conditions (7%O_2/He) for 30 minutes, then cooled down to 70°C. Once the temperature was stable, CO was introduced into the reactor while lowering the O_2 flow rate to provide stoichiometric conditions (2 CO : 1 O_2). Those reaction conditions were changed over time (~ every 30

minutes) in order to study the effects of variation in CO and O_2 partial pressures. Pairs of data points before and after the switch were used to derive the order of reaction. Since the switch in flow rate occurred rapidly, we can assume that the catalyst is in the same state (of deactivation) and hence the changes in reactivity can be related to the changes in gas composition. The experiments were conducted by first varying CO flow rates and then O_2 flow rates, as shown below. In replicate experiments the order was reversed; i.e., the O_2 flow rates were varied first followed by the CO flow rate variations.

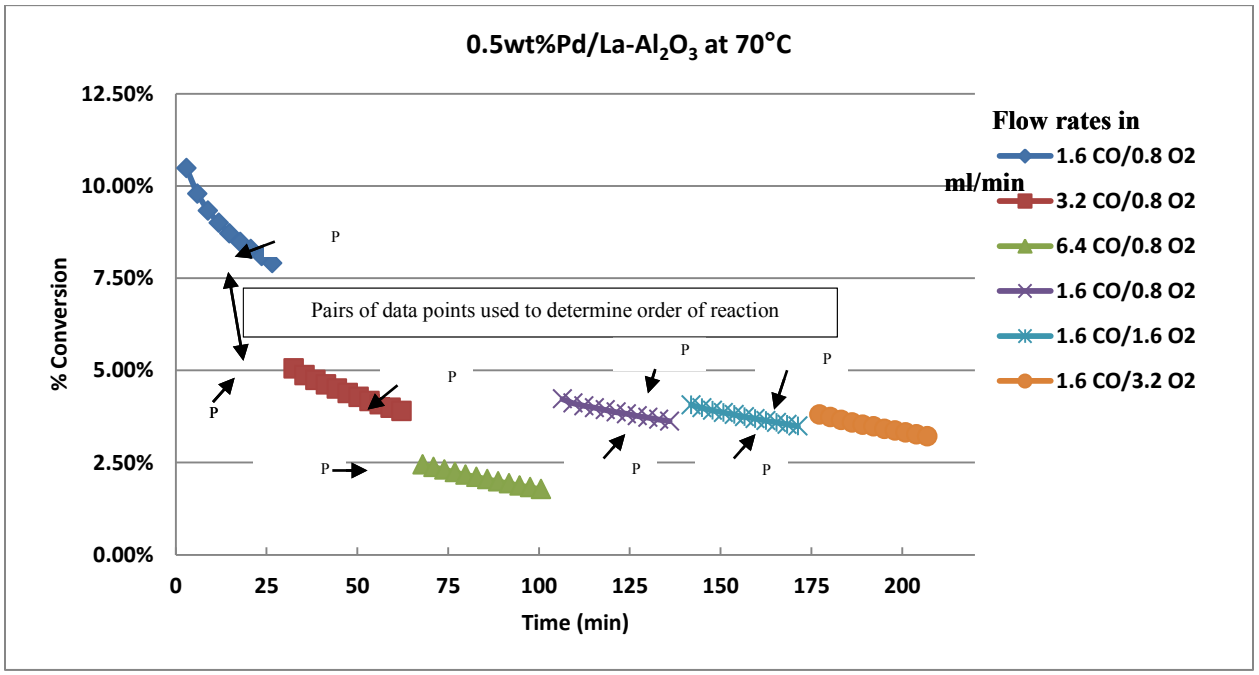

Figure Error! No text of specified style in document.**.5** Order of reaction plots of 0.5 wt.% Pd samples La-alumina (70 °C).

Since the rate is a function of PCO and PO_2:

$$rate = k[CO]^a[O_2]^b$$ **Equation 5.2**

We can solve for a and b using the measured rates of reaction. Multiple experiments allowed us to obtain averages over different times on stream as reported in Table 5.2

Table Error! No text of specified style in document..**2** Rates and partial pressures recorded for 0.5wt%Pd/La-Al_2O_3.

Run # for Pd/La-Al_2O_3	**P[CO] (torr)**	**P[O_2] (torr)**	**Rate CO_2mols-prod/sec**
Point 1	14	7	$9.4x10^{-8}$
Point 2	28	7	$1.2x10^{-7}$
Point 3	28	7	$9.27x10^{-8}$
Point 4	52	7	$1.16x10^{-7}$
Point 5	14	7	$4.3x10^{-8}$
Point 6	14	14	$4.8x10^{-8}$
Point 7	14	14	$4.1x10^{-8}$
Point 8	14	28	$4.5x10^{-8}$

For the 0.5 wt% Pd/La-Al_2O_3 catalyst, and using the data in Table 5.S2, the ratio of rates allows us to solve for the order in CO:

$$\frac{\mathbf{9.4*10^{-8}=k[14]^a[7]^b}}{\mathbf{1.2*10^{-7}=k[28]^a[7]^b}}$$ **Equation 5.3**

$$0.78 = 0.5^a$$

$$\ln(0.78) = \ln(0.5)^a = a * \ln(0.5),$$

Therefore $a = \frac{\ln(0.78)}{\ln(0.5)} = 0.36$.

Using points 3 and 4 we get an $a = 0.35$

When a similar calculation was performed for variations in the flow rates of O_2, the average reaction order is calculated to be 0.15. Based on multiple experiments we derived the following kinetics for this reaction at 70 °C for the 0.5 wt% Pd/La-Al_2O_3 catalyst.

$$\boldsymbol{rate_{Pd/La-Al2O3} = k[CO]^{0.35}[O_2]^{0.15}} \qquad \textbf{Equation 5.4}$$

A.2.3 *Order of reaction for 0.5 wt% Pd/Al_2O_3*

Similar experiments and runs were performed for the 0.5wt%Pd on Al_2O_3, but rapid deactivation allowed only one set of variations to be performed (i.e., vary CO flow or vary O_2 flow) before the catalyst activity at 70 °C was too low to obtain reliable data. When we increased the flow rate of O_2, we saw a large spike in CO_2 production, as shown in the figure below. This increase in reactivity is associated with the oxidation of metallic Pd to PdO and its rapid conversion to metallic Pd forming excess CO_2. Such spikes were not seen on the 0.5 wt% Pd/La-Al_2O_3 catalyst confirming the XAS observations of stable ionic Pd on this catalyst.

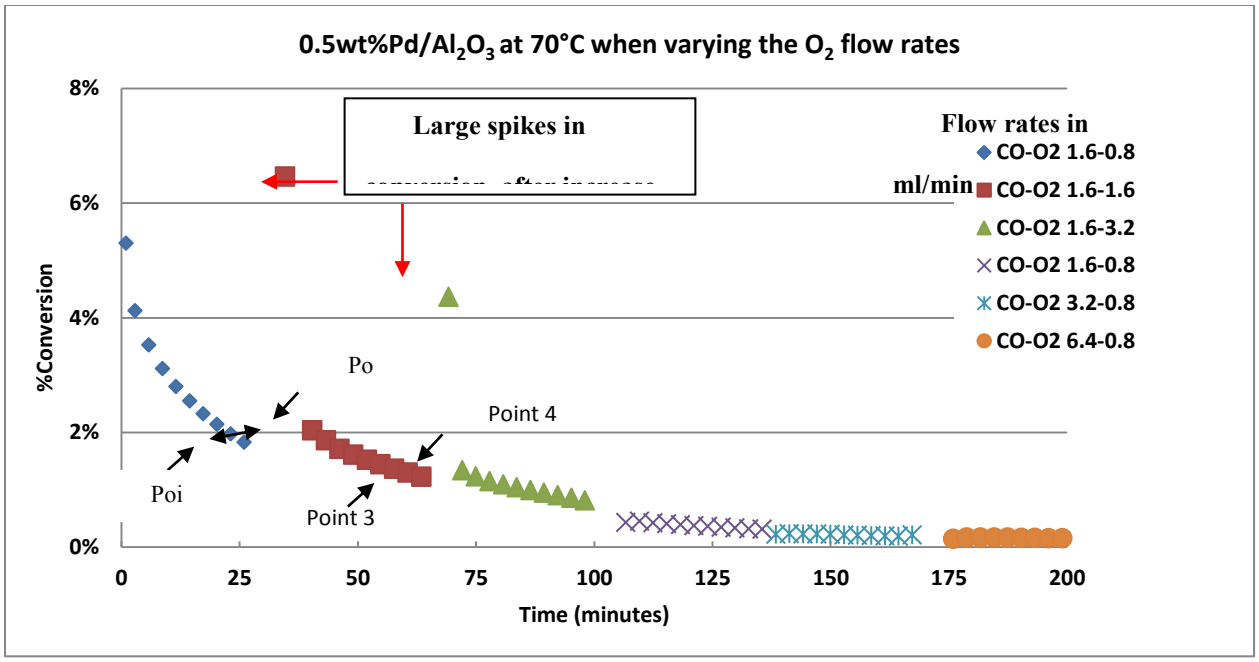

Figure Error! No text of specified style in document.**.6** Order of reaction plots for 0.5 wt.% Pd samples supported on alumina (70 °C).

Table Error! No text of specified style in document.**.3** Experiments where O_2 partial pressure was increased.

Run Pd/Al_2O_3	P[CO]	$P[O_2]$	Rate CO_2mols-prod/sec
Point 1	14	7	$2.2x10^{-8}$
Point 2	14	14	$2.4x10^{-8}$
Point 3	14	14	$1.4x10^{-8}$
Point 4	14	28	$1.6x10^{-8}$

For this catalyst, the ratio of the rates using data from Table 5.S3 is:

$$\frac{\mathbf{2.2*10^{-8}=k[14]^{a}[7]^{b}}}{\mathbf{2.4*10^{-8}=k[14]^{a}[14]^{b}}} \qquad \textbf{Equation 5.5}$$

which then yields:

$0.89 = 0.5^{b}$

$\ln(0.89) = \ln(0.5)^{b} = b * \ln(0.5)$,

$b = \frac{\ln(0.89)}{\ln(0.5)} = 0.17$.

Using points 3 and 4 we get a b = 0.19, with an average of 0.18

This order is similar to that of the La-alumina catalyst which showed a reaction order of 0.16. After one such run, the catalyst had deactivated significantly, so it was subjected to the 700°C oxidation to regenerate the catalyst and then experiments involving variation in CO flow rates were performed.

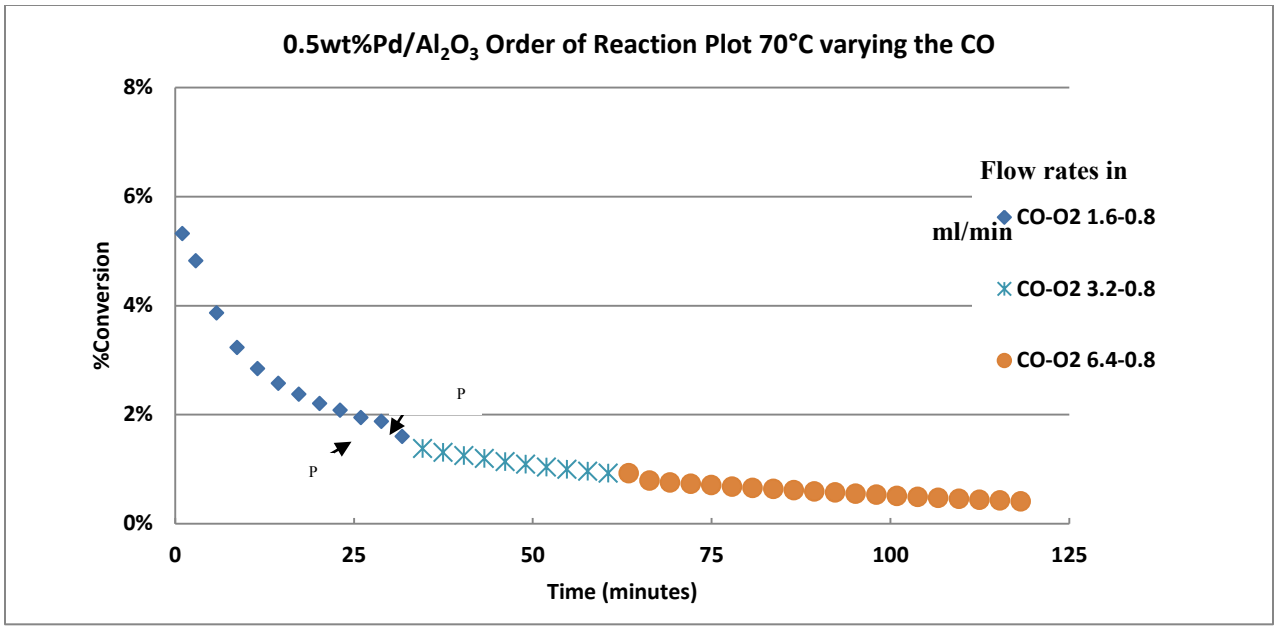

Figure Error! No text of specified style in document.**.7** Order of reaction plots of 0.5 wt.% Pd samples supported on alumina (70 °C), Increase in CO only.

Table Error! No text of specified style in document..**4** Experiments where CO partial pressure was increased.

Run Pd/Al_2O_3	P[CO]	$P[O_2]$	Rate CO_2mols-prod/sec
Point 1	14	7	$1.9x10^{-8}$
Point 2	28	7	$1.7x10^{-8}$
Point 3	28	7	$1.1x10^{-8}$
Point 4	52	7	$9.5x10^{-9}$

For this catalyst the equation the ratio of the rates using data from Table 5.S4 is:

$$\frac{\mathbf{1.9*10^{-8}=k[14]^a[7]^b}}{\mathbf{1.7*10^{-8}=k[28]^a[7]^b}} \qquad \textbf{Equation 5.6}$$

which then yields:

$1.1 = 0.5^a$

$\ln(1.1) = \ln(0.5)^a = a * \ln(0.5)$,

$a = \frac{\ln(1.1)}{\ln(0.5)} = -0.16$.

Using points 3 and 4 we get an a = -0.24, with an average of -0.2

The catalyst was negative order for CO (-0.2) compared to a positive order of 0.36 for the La-stabilized catalyst. For the 0.5wt%Pd/Al_2O_3 the kinetics are:

$$rate_{Pd/Al2O3} = k[CO]^{-0.2}[O_2]^{0.18}$$ **Equation 5.7**

A.2.4 *Reaction orders for deactivated 0.5 wt% Pd/Al_2O_3*

Orders of reaction were also determined for the 0.5wt%Pd/Al_2O_3 after it had become deactivated (shown as run 2 in the light-off curves in Figure 5.2 in the manuscript). In this state the catalyst behaves similar to Pd metal with the behavior shown in the plot and table below. The experiments were carried out at a higher reaction temperature of 175°C to measure kinetics as opposed to the 70°C due to the lower reactivity of this catalyst.

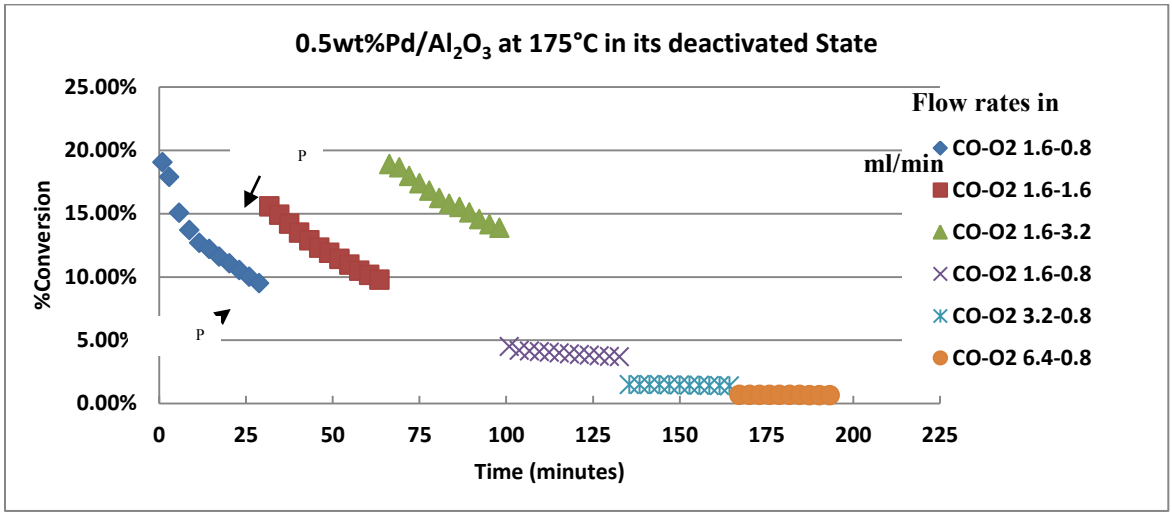

Figure Error! No text of specified style in document.**.8** Order of reaction plots of deactivated 0.5 wt.% Pd samples supported on alumina (175 °C).

For this deactivated catalyst, the ratio of the rates using data from Table S6 is:

$$\frac{\mathbf{1.15*10^{-8}=k[14]^a[7]^b}}{\mathbf{1.89*10^{-8}=k[14]^a[14]^b}}$$ **Equation 5.8**

Which yields:

$0.61 = 0.5^b$

$\ln(0.61) = \ln(0.5)^b = b * \ln(0.5)$,

$b = \frac{\ln(0.61)}{\ln(0.5)} = 0.72$.

Using points 3 and 4 we get an b = 0.95, with an average of 0.84

When calculating a, the first set of points give an a = -1.3 and the second set gives a value = -1.1. The average is = -1.2.

The reaction kinetics for these catalysts are similar to those for Pd metal which we reported previously [2]. These results confirm that the Pd/Al_2O_3 catalyst without the high temperature oxidizing pretreatment behaves similar to metallic Pd. The actual rates of reaction (and TOFs) are considerably greater than Pd due to the small cluster size.

$$\mathbf{rate_{Pd-deact/Al2O3} = k[CO]^{-1.2}[O_2]^{0.84}}$$ **Equation 5.9**

Table Error! No text of specified style in document.**.5** Rates and partial pressures recorded for order of reaction experiments for 0.5 wt% Pd/Al_2O_3 after deactivation.

Run # for	P[C	P[O_2	Rate CO_2mols-

Pd/Al_2O_3	O] (torr)	] (torr)	prod/sec
Point 1	14	7	$1.15x10^{-8}$
Point 2	14	14	$1.89x10^{-8}$
Point 3	14	14	$1.19x10^{-8}$
Point 4	14	28	$2.3x10^{-8}$
Point 5	14	7	$4.5x10^{-9}$
Point 6	28	7	$1.8x10^{-9}$
Point 7	28	7	$1.68x10^{-9}$
Point 8	52	7	$8.2x10^{-10}$

A.2.5 *Mears analysis for external mass transport limitations*

A Mears analysis [3] was performed to ensure that mass diffusion limitations were not encountered during reaction conditions for our palladium on alumina samples. Conditions for our experiments used 0.7ml/min CO, 0.8ml/min O_2, and 70ml/min He with 100mg of catalyst loaded into our reactor. The temperature was varied from room temperature to 300°C with a 2°C/min ramp. We used the rate of reaction at 170°C to investigate the role of transport limitations on reactivity. The Mears criterion is:

$$\frac{k_1' R_p}{k_c} < 0.15 \qquad \textbf{Equation 5.10}$$

Where: $k_1' = k_1 \rho_c$ measured reaction rate constant(sec^{-1})

k_1: volumetric rate (mols/sec-m^3)

ρ_c: bulk density of Al_2O_3 (kg/m^3)

R_p: particle radius (m)

k_c: gas-solid mass transfer coefficient (m/s)

$$\boldsymbol{k_c = \frac{2\mathcal{D}_{CO-He}}{d_p}} \qquad \textbf{Equation 5.11}$$

Where: $\mathcal{D}_{CO-He} = 1.3 \times 10^{-4} \frac{m^2}{s}$: diffusion coefficient of CO in He @170°C

$d_p = 250 \times 10^{-6} m$: particle size

Then:

$$k_c = \frac{2 * 1.3 \times 10^{-4}}{250 \times 10^{-6}} = 1.04 \frac{\text{m}}{\text{s}}$$

Taking the value of k_1 from the reactivity data of Pd/La-Al_2O_3 at 170°C and with the bulk density of the catalyst (alumina) used to get the bed volume $\rho_c = 830\ \text{kg/m}^3$, and the ideal gas law to get concentration

$$\boldsymbol{PV = nRT} \qquad \textbf{Equation 5.12}$$

Where: $P = 84\ kPa$

$R = 8.314\ \frac{m^3 - Pa}{mol - K}$

$T = 443.14\ K$

n/V is calculated to be 22.8 mol/m^3.

The rate was calculated experimentally using:

$$\frac{\boldsymbol{mol\ CO2\ produced}}{\boldsymbol{s}} = \frac{\boldsymbol{Known\ Feed\ of\ CO\ (sccm)} \times \frac{\boldsymbol{1mol}}{\boldsymbol{22{,}400\ cc}} \times \boldsymbol{fraction\ converted}}{\boldsymbol{60\frac{s}{min}}} \qquad \textbf{Equation 5.13}$$

The bed length was calculated to be $1.2\text{x}10^{-3}\text{m}^3$ giving a volumetric flow rate of 0.473mols/sec-m^3 over the bed length. Using k_l and ρ_c calculated to be $k_1' = 0.02s^{-1}$.

Substituting in the values obtained we calculate:

$$\frac{\boldsymbol{k'_1 R_p}}{\boldsymbol{k_c}} = \frac{\boldsymbol{0.02 * (125 \times 10^{-6})}}{\boldsymbol{1.040}} = \quad \boldsymbol{2.5x10^{-6} < 0.15} \qquad \textbf{Equation 5.14}$$

So we can conclude that our system is free of external concentration gradients between the catalyst particle surface and the fluid bulk.

A.2.6 *Mears criterion for interphase heat transfer limitation*

A Mears criterion was also calculated to ensure that heat transfer limitations were not encountered during reaction conditions for our Palladium on Alumina samples. The Mears analysis concludes that there should be no heat limitations if:

$$\frac{\boldsymbol{|\Delta H_R|\ \mathcal{R}\ R_p\ E_a}}{\boldsymbol{R_g\ h\ T_0^2}} < \boldsymbol{0.15} \qquad \textbf{Equation 5.15}$$

Where: ΔH_R: heat of reaction (J/mol)

$\mathcal{R}$: measured rate of reaction per particle volume (mols/sec*m^3)

R_p: particle radius (m)

E_a: activation energy (J/mol)

R_g: ideal gas constant (J/mol*K)

h: gas-solid heat transfer coefficient (W/m^{2}*K)

T_0: temperature of bulk fluid (K).

For our system the values are:

$$\Delta H_R = -283 \times 10^3 \, {}^{J}/_{mol}$$

$\mathcal{R} = 0.473$ (mols/sec*m^3)

$$R_p = 125 \times 10^{-6} \, m$$

$$E_a = 37 \times 10^3 \, {}^{J}/_{mol}$$

$$R_g = 8.314 \, {}^{J}/_{mol\ K}$$

$$T_0 = 170℃ = 443K$$

The heat transfer coefficient can be calculated from:

$$\boldsymbol{h = \frac{2\,\lambda_g}{d_p}} \qquad \textbf{Equation 5.16}$$

where:

λ_g: thermal conductivity of the gas

$$\boldsymbol{\lambda_g = y_{CO}\lambda_{CO} + y_{O_2}\lambda_{O_2} + y_{He}\lambda_{He}}$$ **Equation 5.17**

$$\lambda_g = 0.009(.035) + 0.010(.037) + 0.98(.205) = 0.20\ {}^{W}/_{m\ K}$$

$$h = \frac{2\ \times 0.20}{250\ \times\ 10^{-6}} = 1614\ {}^{W}/_{m^2\ K}$$

Substituting these values into the Mears criterion gives:

$$\frac{283 \times 10^3 * 0.473 * 125 \times 10^{-6} * 37 \times 10^3}{8.314 * 1614 * 443^2} = 2.4x10^{-4} \ll 0.15$$

Since the number is calculated to be well below the Mears criterion of 0.15, we conclude there is no heat transfer limitation for our system under these conditions. The numbers are equivalently low at lower temperatures with the mass transfer limitation number being 0.03 and $4x10^{-4}$ for heat transfer limitations, both below the 0.15 criterion value.

A.3 EXAFS fits

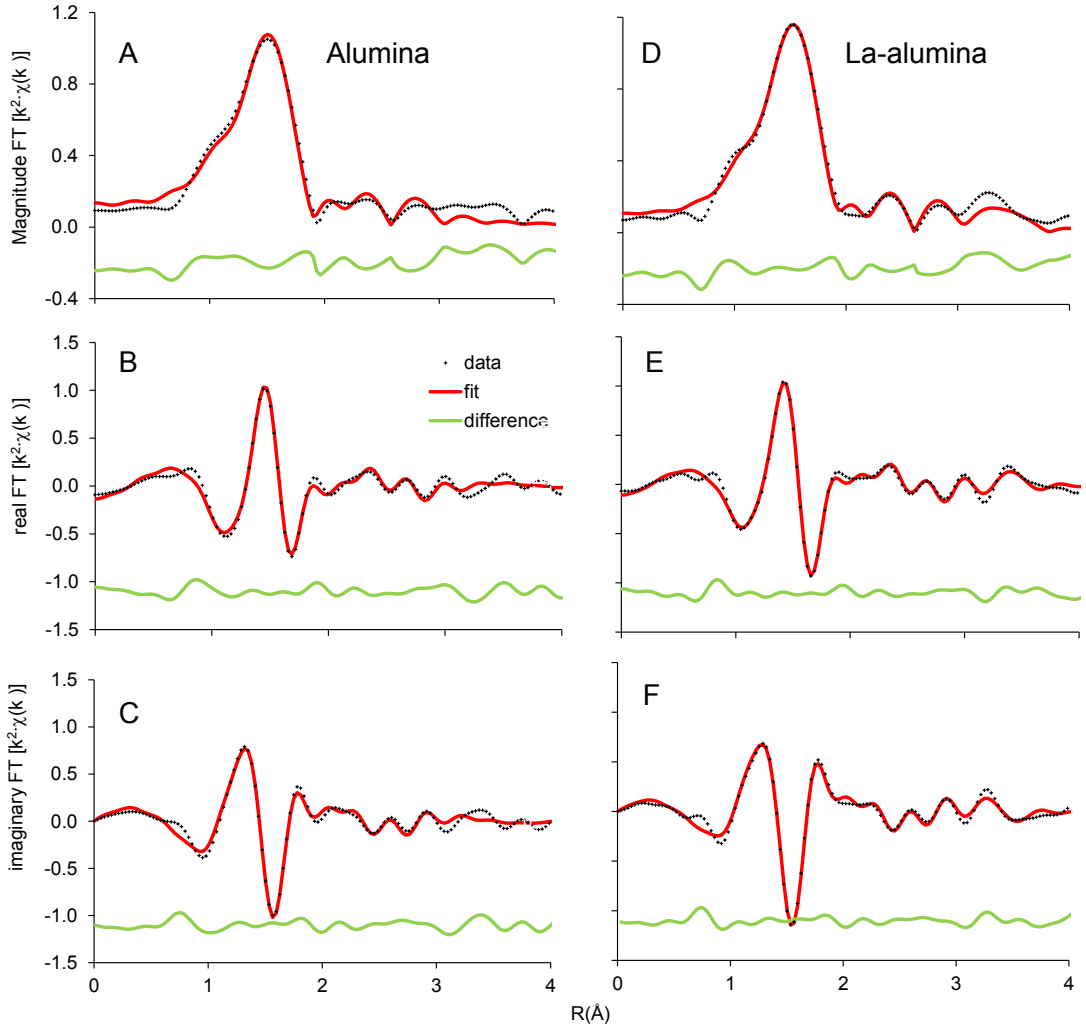

Figure Error! No text of specified style in document.**.9** Fourier transformed EXAFS data collected from 0.5 wt.% Pd/alumina (**A-C**) and 0.5 wt.% Pd/La-alumina (**D-F**). Samples had been calcined at 700 °C for 30 m, and cooled *in situ* to room temperature.

A.4 Density functional theory

All periodic density functional theory (DFT) calculations were performed using the Vienna *ab initio* simulation package (VASP) [4, 5] with the gradient-corrected PW91 exchange-correction functional [6]. For valence electrons, a plane-wave basis set was employed with an energy cut-off of 400 eV, while the ionic cores were described with the projector augmented-wave (PAW) method [7, 8]. A 2×1 unit cell (11.17×8.41 Å) of the γ-Al_2O_3(100) surface [9] with penta-coordinated Al^{3+} sites exposed was simulated using a slab supercell approach with periodic boundary conditions. A 2×2×1 Monkhorst-Pack *k*-point grid [10] was adopted to sample the Brillouin zone, which was found to be converged. This model consists of eight atomic layers with the top four atomic layers relaxed in all calculations. A vacuum spacing of 15 Å was employed to avoid interactions between adsorbates and slab images in the *z* direction. Geometries were optimized until the maximum force on any ion is less than 0.05 eV/Å. Bader analysis was performed using the grid based algorithm of Henkelman[11].

The adsorption energy was calculated as follows:

$$E_{ads} = E_{(adsorbate + surface)} - E_{(free\ molecule)} - E_{(free\ surface)} \qquad \textbf{Equation 5.18}$$

For each elementary step, the initial state (IS) and final state (FS) are first optimized by minimizing the total energy. The climbing image-nudged elastic band (CI-NEB) method [12] was used to determine transition states (TS) between IS and FS, with the

conventional energy (10^{-4} eV) and force (0.05 eV/Å) convergence criteria. Vibrational analysis was then performed to confirm the stationary points. The highest image along the minimum energy path was denoted as TS. The energy barrier E_a of each elementary reaction was calculated by the energy difference between TS and IS. The reaction energy E_r of each elementary reaction was calculated by the energy difference between FS and IS.

A.4.1 *Optimization of Pd doped Al_2O_3*

As shown below, there are four different Al atoms on the (100) surface of γ-alumina [9], and the energy needed to create a vacant site has been calculated. Site A has the smallest energy cost, thus chosen to be substituted by a Pd atom.

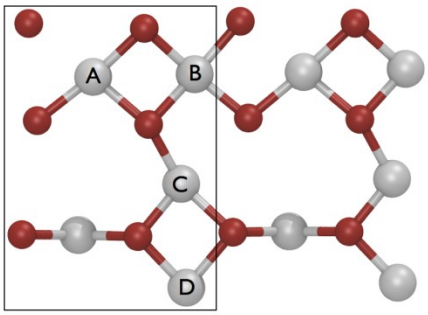

Figure Error! No text of specified style in document..**10** The geometry of the Al2O3 (100) surface showing possible sites for location of the Pd atom.

The optimized geometry of the Pd@Al_2O_3 system features the Pd atom coordinating with four nearby oxygen atoms, forming a planar geometry. The distances of Pd-O are

computed to be 2.11, 2.11, 2.13 and 2.13 Å, which are consistent with the experimental value 2.04 Å. There is a fifth, apical oxygen beneath Pd, with a Pd-O distance of 2.23 Å, which indicates a much weaker interaction. The Bader charge [13] of the Pd atom is (+1.04*e*), indicating significant electron transfer from the Pd atom to the surrounding oxygen atoms. This oxidation state is also consistent with the experimental measurement. The positively charged Pd atom, which differs from the metallic Pd in nanoclusters, might be responsible for the observed catalytic activity of the $Pd@Al_2O_3$ catalyst.

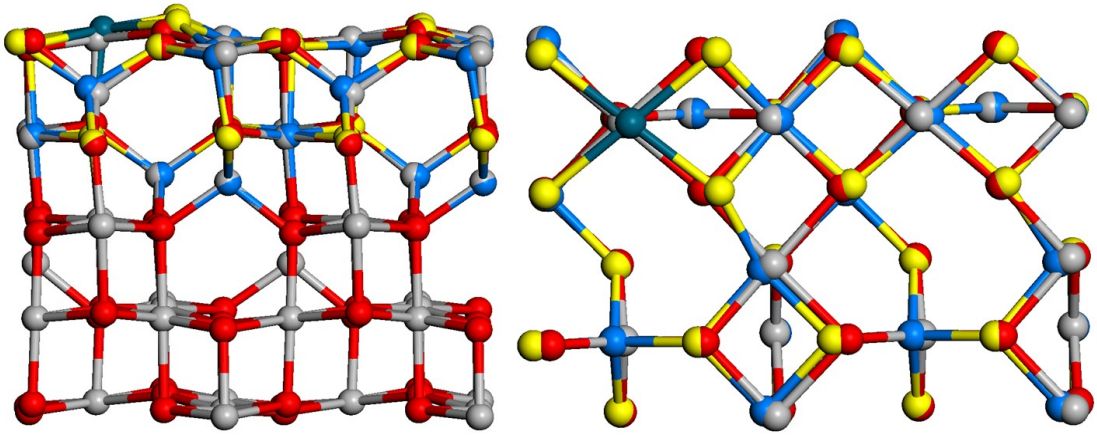

Figure Error! No text of specified style in document..**11** The figure shows the overlap of a relaxed and unrelaxed (100) surfaces of γ-alumina with a Pd atom in an Al site. Atom color: O-relaxed (yellow), O-unrelaxed (red), Al-relaxed (light blue), Al-un-relaxed (grey), Pd (dark blue)

Due to differences in size and electronic structure, the Pd perturbs the surface somewhat, particularly in its vicinity. For example, the shifts for the four oxygen atoms coordinated to Pd are found to be +0.23, +0.23, -0.06, -0.06 Å in the z-direction.

A.4.2 *Adsorption of gas phase species*

CO: The carbon monoxide is found to bind atop on the tetra-coordinated Pd atom with an adsorption energy of -0.72 eV, which is much smaller than that (-1.97 eV) on Pd(111). The C-O bond length and the Pd-C distance are found to be 1.15 and 1.90 Å, respectively. The angle of O-C-Pd is 174.7º. It should be noted that, after adsorption, the distances between Pd and its surrounding oxygen atoms changed to 2.34, 2.09, 2.37 and 2.11 Å, consistent with experimental results that, during the reaction, the coordination is found to drop to 3 or less. We have also considered the adsorption of CO on Pd in the case of O_2 filling the oxygen vacancy, and the adsorption energy becomes -0.33 eV. The adsorbed CO has a slightly elongated bond length, indicating weakening of the bond. The C-Pd distance is 1.93 Å and the O-C-Pd angle is 170.4º. The distance between C and the upper O (denoted as O_{air}) atom of the adsorbed O_2 is 2.64 Å, well positioned for reaction. The Pd-O distances are 2.36, 2.25, 2.06 and 2.47 Å when CO is adsorbed.

When CO adsorbs on the top of a Pd atom, the frequency of CO is calculated to be 2105 cm^{-1}, which agrees very well with the experimental observation (2110 cm^{-1}) [14]. This frequency changes to 2078 cm^{-1} after an oxygen molecule fills the vacancy. These frequencies are consistent with the elongation of the CO bond length from pi-back

bonding from the metal *d*-orbitals to the π* CO orbital. On the 100 surface, we did not find a stable configuration for carbonate.

CO_2: The adsorption energy for CO_2 on Pd is very small (-0.03 ~ -0.05 eV), indicating it is readily desorbed from the catalyst. The distance between C and Pd is typically larger than 3.00 Å.

O_2: The adsorption energy of the O_2 molecule in the oxygen vacancy, created after CO reacts with surface O, is -2.25 eV. The distances between Pd and its surrounding three lattice oxygen atoms are 2.15, 2.10 and 2.36 Å. The distances of O_{air}-O_{air} and O_{air}-Pd are found to be 1.45 and 1.93 Å, respectively, which indicates that molecular oxygen, although not disassociated, is activated upon binding to this site. The angle of Pd-O-O is calculated to be 110.8º.

A.4.3 *Bader charge analysis*

Bader charge analysis [13] was performed on the PdO_4 and PdO_3 active site to determine where the charge is distributed upon formation of the O vacancy. In a formal charge picture, the initial 10 electron O^{2-} species is lost as a neutral 8 e^- oxygen atom in CO_2, leaving 2*e* behind to be accounted for. According to the Bader charges, the oxygen atoms in the PdO_4 active site are not formally O^{2-} but closer to $O^{1.5-}$ (-1.5, -1.4, -1.4 and -1.4 specifically), as might be expected in the coordinately-unsaturated surface, a notable departure from an O^{2-} formal charge. Taking the total charge on the Pd and adjacent O

atoms before and after the defect formation, the Bader values indicate a 0.2*e* difference rather than the 2*e* predicted from formal charges. This is a result of a reorganization of partial charges among the remaining atoms in the active site. Pd is reduced by 0.6*e*, and the remaining oxygen atoms bound to Pd are collectively reduced by 0.8*e*. The remaining 0.2*e* is then distributed though the 9 nearest Al neighbors coordinated to the oxygen atoms in the active site. Although the Al in Al_2O_3 is typically not considered to be a reducible moiety, we find that one Al bound to two Pd coordinating oxygen atoms is reduced by 0.17*e*. The remaining 0.03*e* is distributed across the remaining adjacent Al atoms. In short, the charge balance for formation of the defect state is achieved as partial charges are distributed throughout the remaining structure. As this analysis shows, it may not be appropriate to assign formal charges in this system, as it is for homogeneous analogs. The extended nature of the support allows far more flexibility in distributing partial charges than in the case of relatively small and isolated homogenous catalysts, which we believe is a key feature of this unique catalyst.

Figure A.12 shows the d-band of the LDOS for atomic Pd compared to Pd metal. For the atomically dispersed Pd we see the portion of the d band, atomically discrete as expected, shifted to the right above the Fermi level, indicating that these orbitals are becoming unoccupied, compared to the fully occupied d-band in Pd metal. This is also consistent with our Bader charge analysis.

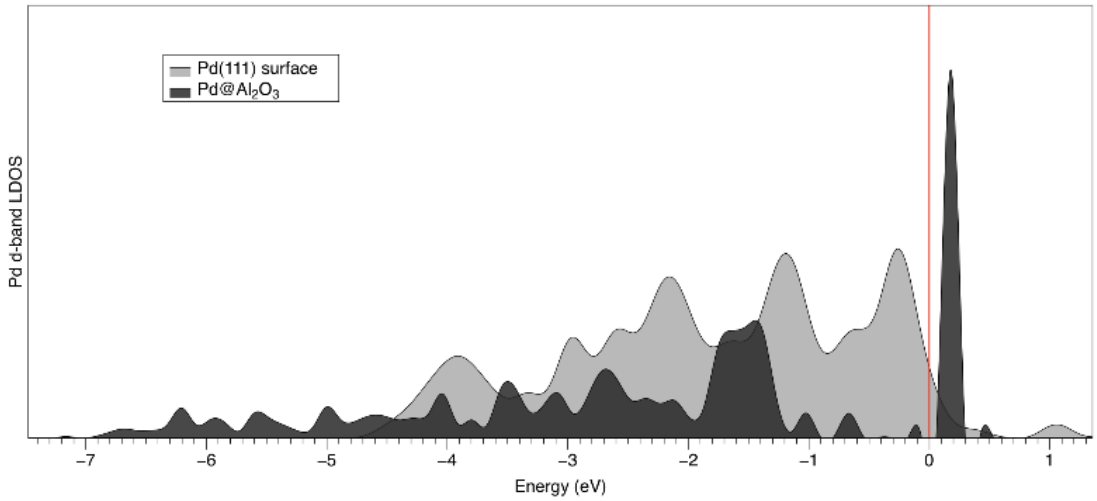

Figure Error! No text of specified style in document.**.12** The d-band LDOS of the Pd(111) (gray) surface and the Pd@Al2O3 atom (black).

Supplementary References

1. Beguin, B., E. Garbowski, and M. Primet, *Stabilization of Alumina by Addition of Lanthanum.* Applied Catalysis, 1991. **75**(1): p. 119-132.
2. Johnson, R.S., et al., *The CO oxidation mechanism and reactivity on PdZn alloys.* Physical Chemistry Chemical Physics, 2013. **15**(20): p. 7768-7776.
3. Mears, D., *Tests for Transport Limitations in Experimental Catalytic Reactors.* Industrial & Engineering Chemistry Process Design and Development, 1972. **11**(2): p. 320-320.
4. Kresse, G. and J. Hafner, *Ab initio molecular dynamics for liquid metals.* Phys. Rev. B, 1993. **47**: p. 558-561.
5. Kresse, G. and J. Furthmuller, *Efficient iterative schemes for ab initio total-energy calculations using plane wave basis set.* Phys. Rev. B, 1996. **54**: p. 11169-11186.
6. Perdew, J.P., et al., *Atoms, molecules, solids, and surfaces: Applications of the generalized gradient approximation for exchange and correlation.* Phys. Rev. B, 1992. **46**: p. 6671-6687.
7. Blöchl, P.E., *Project augmented-wave method.* Phys. Rev. B, 1994. **50**: p. 17953-17979.
8. Kresse, G. and D. Joubert, *From ultrasoft pseudopotentials to the projector augmented-wave method.* Phys. Rev. B, 1999. **59**: p. 1758-1775.
9. Wischert, R., et al., *γ-alumina: The essential and unexpected role of water for the structure, stability, and reactivity of "defect" sites.* J. Am. Chem. Soc., 2012. **134**(35): p. 14430-14449.
10. Monkhorst, H.J. and J.D. Pack, *Special points for Brillouin-zone integrations.* Phys. Rev. B, 1976. **13**: p. 5188-5192.
11. Tang, W., E. Sanville, and G. Henkelman, *A grid-based Bader analysis algorithm without lattice bias.* Journal of Physics-Condensed Matter, 2009. **21**(8).
12. Henkelman, G. and H. Jónsson, *Improved tangent estimate in the nudged elastic band method for finding minimum energy paths and saddle points.* J. Chem. Phys., 2000. **113**: p. 9978.
13. Bader, R.F.W., *Atoms in molecules: A quantum theory*. 1990, Oxford: Oxford University Press.
14. Xu, X.P. and D.W. Goodman, *An Infrared and kinetic-study of CO oxidation on model silica-supported palladium catalysts from 10-9 to 15-torr.* Journal of Physical Chemistry, 1993. **97**(29): p. 7711-7718.